Modelling the coastal ambient noise field in time, frequency, and space

By

Calder Robinson

Submitted in partial fulfilment of the requirements
for the degree of Master of Science

At

Dalhousie University
Halifax, Nova Scotia
December 2020

The ocean is a big place.
It is easy to get lost in its boundless depths and beguiling mysteries.

For my family and those who continued to support me as my own drive for realization faltered.
Without them, this thesis would remain incomplete.

TABLE OF CONTENTS

List of Tables

List of Figures

Abstract

Natural ambient noise levels in time, frequency, and space, in coastal regions are modeled based on local environmental forcing and propagation conditions. Continuous audio recordings were taken between April 18th and May 12th, 2018 off Sooke Inlet, BC, a shallow water region with complex bathymetry and persistent vessel traffic, for model parameterization. The received noise levels were decimated to their hourly minimums, and spectral component filtering was used for source classification. An ambient noise model in the form of a linear combination of wind speed and rain rate source terms, modulated by a tidally driven amplitude term, was developed. Model-data comparisons of monthly sound levels from April 2018 to February 2019 show less than 5 dB error above 1 kHz, and less than 3dB error above 20 kHz. A computational sound propagation model is used to compute the source level per unit of area of the natural noise generating mechanisms.

Acknowledgements

I would like to extend thanks to Dr. Svein Vagle and the other members of his team at IOS for their willingness to provide me with acoustic data, opportunities to go to sea, and for hosting me at their institution for a portion of this thesis; To Bruce Martin for many fruitful conversation on ambient noise processing and calibration information; To the crew of the CCGS Vector who forgave my sea going ignorance and aided in smooth deployments, and lastly to Dr. David Barclay and the rest of my committee for making this entire project possible.

1. Introduction

Physical properties of water such as its density and relative incompressibility allow sound to travel at high speed over great distances underwater, permitting trans-basin target detection with the SOFAR channel (Abileah and Lewis 1996 Sep 26), long distance marine mammal communication (Dudzinski et al. 2009) and the acoustic detection of the ocean weather footprint (Wenz 1962; Vagle et al. 1990; Nystuen et al. 2010). The cylinder[1] of influence of a sound source is therefore not restricted to its immediate location but contributes to the global oceanic susurrus comprised of locally or distantly generated sounds, generally known as the ambient noise field. This makes underwater sound and noise useful for many aquatic organisms, as it provides a means to "shed light[2]" on their surroundings in an environment where light and other electromagnetic waves are restricted. Humans have progressively exploited sound in the marine environment with the advent of active and passive acoustic methods with the introduction of SONAR in WW1 (McCarthy 2004).

The objectives of this project are threefold: filter acoustic recordings from a heavily trafficked area to isolate for the ambient environmental signal consisting of wind driven waves, rain and currents, parameterize an empirically fit effective source term model for near shore regions using the filtered recordings, and combine the model with the local effective listening area calculated from the numerically modeled transmission loss, yielding the sound source level (SSL) per unit area. With a well parameterized source level in terms of wind and surface current vectors, rainfall rate, and an accurate transmission loss model, the near shore ambient noise level

[1] While sound radiates in the shape of a sphere from a point source, the surface and bottom of the ocean truncate it such that at long ranges it is better represented as a cylinder.

[2] Given that light itself does not penetrate to great depths in the ocean (Lee et al. 2005), marine organisms have adapted to other methods of sensing their environment (Dudzinski et al. 2009).

may generally be used to determine the absolute contributions of natural mechanisms and anthropogenic activities in the sound field. This project takes place in coastal British Columbia, with five stations deployed throughout the strait of Juan de Fuca, Salish Sea, and Gulf Islands (Figure 1). Continuous acoustic recordings are on-going, having begun in January of 2018. Preliminary model development was performed on a subset of the recordings collected at station S in the open straight off Sooke inlet between April 18 and May 12, 2018 and was tested against recordings from April 18, 2018 to February 27, 2019.

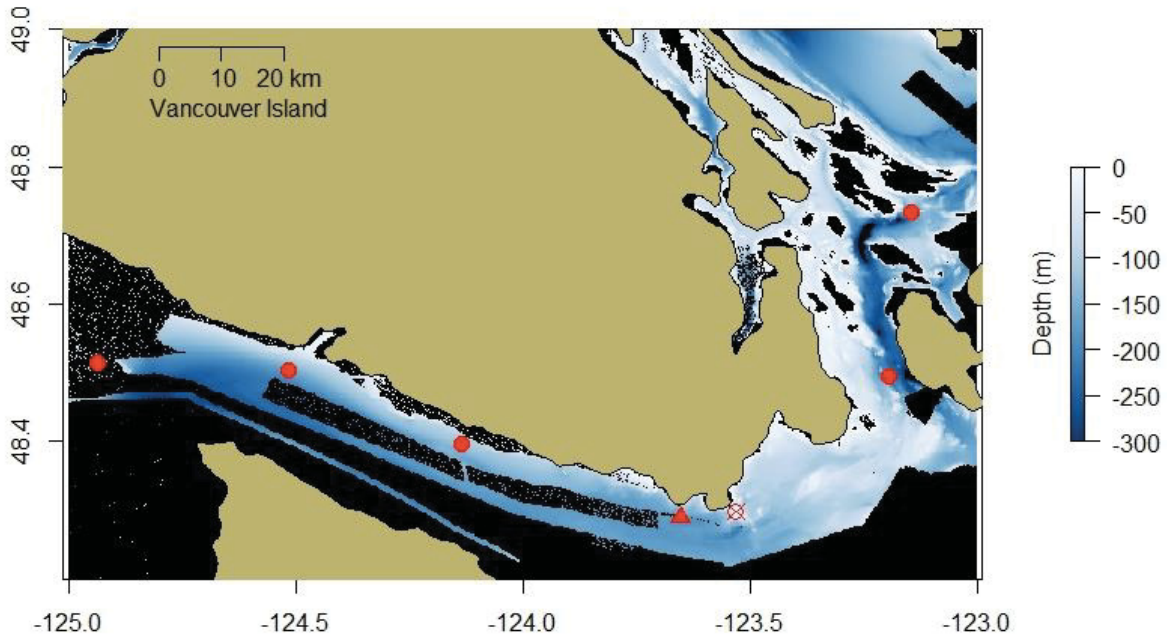

Figure 1: Recording locations (red) overlaid on the bathymetry (CHS NONNA-100) of the sampling region (blue, scale included) in coastal British Columbia. Sooke station (Station S), the site of primary investigation is marked by a triangle. Race Rocks light station is marked by the crossed circle. Black represents regions of no high-resolution bathymetric data, including small islands and other regions above water.

1.1 Motivation

Noise levels in the deep ocean have been increasing over the last century (McDonald et al. 2006; Chapman and Price 2011), although recent decreases at low frequencies have been observed (Miksis-Olds and Nichols 2016). This trend is driven by increasing human use of the ocean for transport of the growing international trade of goods (Frisk 2012) and balanced to some extent by improved noise management systems. This increase in international commercial shipping must be accompanied by an growing use of coastal oceans, along with an expansion of recreational and commercial activities (e.g. ferries, fishing), particularly in regions near key export and import hubs such as the Port of Vancouver (Thomson and Barclay 2020).

Given the technical complexity of monitoring underwater noise, human generated acoustic pollution in the natural ocean environment has not been considered until relatively recently (McCarthy 2004). Modeling a natural coastal ambient noise field baseline is important because there are few pristine soundscapes remaining (Marques and Araújo 2015), resulting in no absolute standard for pre-anthropogenic noise levels, and thus no basis for comparison or context for current levels of emission. While developing baselines is a less than glamorous pursuit, they are nonetheless a fundamental part of acoustic monitoring (Ainslie et al. 2018).

To establish the degree to which ocean noise is a concern for the marine environment, it is essential that normal noise levels and variability be established with geographic location, through seasonal variations, and changes due to anthropogenic activity. This effort is complicated by the efficiency with which sound propagates underwater. Due to depth-gradients in pressure, temperature, salinity, the sound-speed profile can cause favourable propagation conditions where distantly generated noise mixes with locally generated noise (Urick and Kuperman 1989). The physical dynamics of the ocean (waves, currents, tides) and atmosphere

(persistent winds, storms) determine the mixing of water masses and structure of the sound-speed profile. These conditions are dynamically variable in Canadian waters and the effect of noise from a single ship may vary significantly from one day to the next. Additionally, meteorological conditions drive sound production mechanisms at the ocean's surface, such as breaking waves and rainfall, causing short-term variability in the natural underwater soundscape.

Baseline natural environmental noise can be used to generate quantitative estimates of the anthropogenic contribution to the soundscape, conceptually as:

$$A_c = T - E \qquad Eq.1$$

where the measurements are expressed as T the 'total' sound field, natural noise sources are summarized as E, the 'environmental' and anthropogenic contributions, A_c, may be from a wide range of industrial or human activity. The contributions of relatively transient acoustic signals of biological and geophysical origin to the underwater soundscape are ignored.

Quantitative estimates of the anthropogenic contribution to the underwater sound field are needed by bodies such as Transport Canada (TC 2020), the Department of Fisheries and Oceans (DFO 2020), indigenous groups (TC 2020), and the Port of Vancouver (Olszewski and Ren 2015) to inform policy and legislation on acoustic noise levels in Canadian coastal regions. The issue of anthropogenic underwater noise is of societal concern because of the potential impact on marine mammals and other valued marine species; there are reports of whale strandings following explosive noises and high intensity sonar trials (Ketten et al. 1993). Sub-lethal consequences can also result in marine mammals due to chronic noise that interferes with normal animal activities, including changes in stress hormones in whales (Rolland et al. 2012). For animals that navigate, communicate, hunt and forage using acoustics, an increase in human generated noise can reduce the range over which these methods are effective or mask the

necessary signals altogether (Putland et al. 2018; Pine et al. 2020). Many marine fish, including commercial species, are known to be acoustically active and use sound to detect prey or evade predation with elevated anthropogenic noise having shown to negatively impact their catch rates (Engås et al. 1996).

In the study region, the impacts of vessel noise on the endangered Southern Resident Killer Whales (SRKW) are of particular interest. It has been observed that ship traffic can disrupt foraging behavior (Lusseau et al. 2009) and that vessel presence has the impact of causing SRKW to raise their calling amplitudes (Holt et al. 2009) along with other behavioural changes (Williams et al. 2014). Though ship noise is most powerful in the 100's of Hz band, it can extend into the frequency range which may mask echolocation signals (Veirs et al. 2016).

Central to traditional active and passive SONAR acoustics is the concept of signal to noise ratio (SNR), the difference between the amplitude of a signal relative to the amplitude of the background variation where the signal is detected. The noise portion of this relationship is typically comprised of the ambient sound field of the ocean and electronic and mechanical noise generated by the recording system and associated hardware. Accurate modeling of the ambient background allows signal processing algorithms and acoustic antenna designs (absolute and relative sensor positioning) to be implemented to optimize the SNR and model detection performance.

Natural ambient sound can be inverted to passively monitor a variety of noise-generating natural processes, including wind speed (Vagle et al. 1990), rainfall rates and drop size (Medwin et al. 1992; Ma and Nystuen 2005), snowfall rates (Alsarayreh and Zedel 2011), breaking waves (Bass and Hay 1997; Deane and Stokes 2010), and currents. Wind-driven noise can also be used to infer the physical properties of the ocean through which the sound is propagating, such as

temperature (Woolfe et al. 2015), local sound speed (Barclay and Buckingham 2013), seawater pH (Barclay 2011), seabed geoacoustic properties (Barclay et al. 2019) and structure (Siderius et al. 2006), and water column structure (Katsnelson et al. 2019; Shajahan and Barclay 2020).

The WOTAN (Weather Observation Through Ambient Noise) project (Vagle et al. 1990) demonstrated the applicability and performance of a sustained passive acoustic wind and rain monitoring system in the open ocean. In the deep water (> 100 m) case, the relationship between the wind speed and noise level depends almost uniquely on the action of the wind stress on ocean's surface. A frequency dependent source level per unit area (or source level density) as a function of wind speed was estimated by assuming simple geometric spreading sound propagation.

Shallow water ambient noise levels are site dependent (Ingenito and Wolf 1989), making the development of a generalized relationship between wind forcing and noise levels difficult to establish (Wille and Geyer 1984). Previous work in shallow water met with relative success and required significant tuning to the local environment through in situ transmission loss experiments (Kuperman and Ferla 1985). Sound propagation in littoral waters depends heavily on the bathymetry and seabed properties, while the local coastal topography varies fetch as a function of wind direction. Combining these passive and active observations allowed the source level density for wind noise to be estimated.

In this work, a computational approach is taken to estimate the surface receive sensitivity, or effective listening area of the receiver as a function of frequency, from which empirical relationships between power spectral levels and meteorological and oceanographic forcing can be determined. Combining these relationships with the receiver's effective listening area allow the source level per unit area to be estimated.

1.2 Goal and Objectives

The goal of this research is to model the soundscape baseline in coastal waters as it varies in frequency, time, and space. The model will be empirically driven by acoustic data collected in the Salish Sea along with available forcing data such as wind speed and direction, surface current speed and direction, and spatial rainfall intensity. This will be accomplished by achieving the following three objectives:

1. Develop a sufficiently robust filtering system to isolate noise that is natural and abiogenic in origin.
2. Parameterize an empirical ambient noise model as a function of wind speed and perform model data comparison to evaluate suitability. In doing so, other environmental sources and forcing terms, including precipitation and tidal current speed and direction, and wind direction, may be linearly included to improve fit.
3. Transform the empirical model into a generalized relationship between the forcing variables and the source level per unit area by computing the local effective listening area.

2 Theory

Human perception of sound is the sensory representation of a summation of pressure waves[3], where loudness is the perceived pressure amplitude of these waves and pitch the perceived frequency. Underwater noise is identical, save that the medium of propagation is water, rather than air. While minor in scope, this subtle difference has numerous effects on the behavior of sound – chief among them its fast sound speed and high transmission efficiency, leading to its wide use as a means to explore and sense the underwater environment.

The speed of a pressure wave is a function of the density of its medium of transference, and thus also a function of anything that changes this parameter. Kundu et al (Kundu et al. 2008) have an excellent treatment of pressure wave speed relationship with bulk material properties, presented here in summary. Consider a minute pressure disturbance travelling right to left at some speed c into still water. Ahead of the wavefront, the fluid has pressure P, density ρ, temperature T, and particle speed $u = 0$. Behind the wavefront, it has pressure $P + \partial P$, density $\rho + \partial\rho$, temperature $T + \partial T$, and particle speed ∂u, in the direction of propagation. To simplify analysis, we enter the waves frame of reference, and consider a finite area A on the wavefront, with fluid entering the front at speed c, and leaving at speed $c - du$. Taking the mass balance yields

$$A\rho c = A(\rho + \partial\rho)(c - \partial u) \qquad Eq.2$$

Ignoring second order terms due to low assumed disturbance amplitude, this simplifies to

$$\partial u = c\left(\frac{\partial\rho}{\rho}\right) \qquad Eq.3$$

[3] Hence the representation of noise as sound pressure in μPa, or in dB referenced to 1 μPa

Applying the momentum equation to our system, namely that net force (left side) is equal to the change in momentum in the system (right side) without viscous stresses, yields:

$$PA - (P + \partial P)A = (A\rho c)(c - \partial u) - (A\rho c)c \qquad Eq.4$$

and simplifies to

$$\partial P = \rho c\, \partial u. \qquad Eq.5$$

Substituting du from Eq. 3 yields

$$c^2 = \frac{\partial P}{\partial \rho}. \qquad Eq.6$$

In seawater these parameters are generally temperature, pressure, and density. The true equation of state is formulated in terms of the Gibbs free energy of the system as described in the TEOS-10 standard (McDougall and Barker 2011). As the system is highly complex, specific interaction between temperature, pressure, and salinity on density in seawater are empirical relationships derived from large amounts of experimental data.

In the following sub sections, the theoretical basis for a linear combination of acoustic source terms is presented. Section 2.1 details the process of moving a time domain acoustic pressure series into a frequency domain acoustic power series. Section 2.2 describes the complex effects that the propagation environment has on the received acoustic signal, the methods used to quantify these effects, and the use of the principle of reciprocity in modelling a distributed noise source. From a conceptual model of a collection of superimposed source terms in the time domain, Section 2.3 develops the process of source separation through the frequency domain and calculation of the sound source level from received level through acoustic transmission modelling. Section 2.4 demonstrates the use of a common regression model as a way to parameterize the linear combination of the different sources of environmental noise in the received soundscape.

2.1 Signal Processing

It is useful to break noise signals down into their spectral components for further analysis. This is typically achieved by performing a Fourier Transform, moving a signal from the time domain into the frequency domain. As the samples in this study are discrete time series, a discrete transform is used, given by,

$$X_k = \sum_{n=0}^{N-1} x_n \cdot e^{-\frac{i2\pi kn}{N}} , \qquad Eq. 7$$

where X_k represents the spectral energy at frequency k, x_n represents the signal of interest, N represents the number of samples in the signal, and $i = \sqrt{-1}$. The resulting spectra will have a frequency resolution equal to the inverse of $T = N\Delta t$, the signal length in the time domain where Δt is the time resolution determined by the sampling rate, f_s.

A straight, discrete Fourier Transform will also be biased towards the spectral components in the middle of the time domain window. The Welch periodogram (Welch 1967) alleviates this bias by dividing the time domain signal into overlapping subsamples which are Fourier transformed independently and recombined into a mean spectrum in the frequency domain. In doing so, the beginning and end of the signal are better represented in the final spectra. It also reduces the variability in the final spectra, although this comes at the expense of frequency resolution due to the shortened signal length.

The complex output of a Fourier transform can be squared by multiplication by its complex conjugate to compute the signal's power present in a time series as a function of frequency,

$$\bar{X}_k = \frac{\langle X_k X_k^* \rangle}{T} \qquad Eq. 8$$

where $\bar{X}_k$ is the power at frequency k, * denotes the complex conjugate, and the $\langle\ \rangle$ indicate that the ensemble average has been taken. By Plancherel's theorem, the integral of the squared modulus of a function in the time domain is equal to the integral of the squared modulus of its spectrum, where both quantities represent the signal's energy.

For the discretely sampled time series, the spectrum will range from the negative to positive Nyquist frequency ($f_s/2$) and, for all real-world signals, be mirrored about 0 Hz, making spectral values at negative frequencies redundant. The spectrum from 0 to $f_s/2$ can be multiplied by a factor of 2 to account for the loss in energy in the discarded negative frequencies and be made independent of sample length (frequency resolution), resulting in a power spectrum in the units of $\mu Pa^2 Hz^{-1}$. Measured noise power as a function of frequency is the acoustic metric used in this study.

2.2 Sound Propagation

The sources of interest in this study, bubbles generated by breaking waves and rain drop impacts, are all near-surface processes occurring uniformly over the area of sea surface that ensonifies the receiver. For each hydrophone, the range dependent listening area is called the surface receive sensitivity, which depends on the depth of the sensor and details of the propagation environment. It is practical to model ensembles of these bubbles as monopole sources with a prescribed strength per unit area, placed uniformly in an infinite horizontal plane at fixed depth, z', below the surface (Cron and Sherman 1962; Barclay and Buckingham 2013).

The depth-dependent sound speed profile and range-dependent bathymetry in the surrounding ocean requires the use of computational method to determine the transmission loss. Sound will refract as it passes through mediums of changing sound speed, where continuously varying sound speed by depth and range will result in rays bending (wave fronts refracting)

continuously in response. Given the bandwidth of the wind driven noise (0.100 – 100 kHz), the most practical and appropriate computational model of sound propagation is ray tracing. Bellhop is a collection of algorithms that solve the Eikonal equation to compute ray trajectories, and the transport equations to estimate the density of rays at all points, itself an estimate of the acoustic pressure field as a function of range and depth in an arbitrarily complex environment. The transmission loss is then calculated as the proportional difference between source and received level.

The range dependent contribution of each patch of surface noise to a receiver placed at the location of the model source can be calculated by a running a single instance of the computational model and invoking the principal of reciprocity (Carey and Evans 2011). In the simulation, the source can be placed at the receiver, and the field can be computed at the depth z' at all ranges. Since the wave equation obeys reciprocity, the resulting computation can be used to determine the field at the actual receiver (simulated source) due to a source placed arbitrarily in range at depth z'.

The ray tracing software Bellhop will be used to compute the surface receive sensitivity at the study location as a function of frequency (Porter 2011).

2.3 A shallow water ambient noise model

In terms of spatial and temporal extent, the oscillation and collapse of bubbles are a dominant acoustic source in the ocean (Wenz 1962; Deane and Stokes 2002), created by bubble entrainment of breaking waves (Farmer and Vagle 1988), falling raindrops (Ma and Nystuen 2005), or cavitation on the blades of a ship's screw (Arveson and Vendittis 2000). Thus, to a certain degree, it is possible to correlate the natural underwater noise field to sea-state, offering a method of predicting underwater noise levels (Wenz 1962; Kuperman and Ferla 1985), or if

inverted, sea-state from noise levels (Vagle et al. 1990; Nystuen et al. 2010). This is made more complex as the sound, once generated and moving towards the receiver, can be further influenced by the environment through which it is propagating (Figure 2). In the open ocean, off the continental shelf, propagation effects are typically restricted to changes in sound speed profiles, however in shallower water, the sound interacts with the ocean floor making the propagation environment more complex due to multiple reflections and bottom attenuation (Jensen et al. 2011).

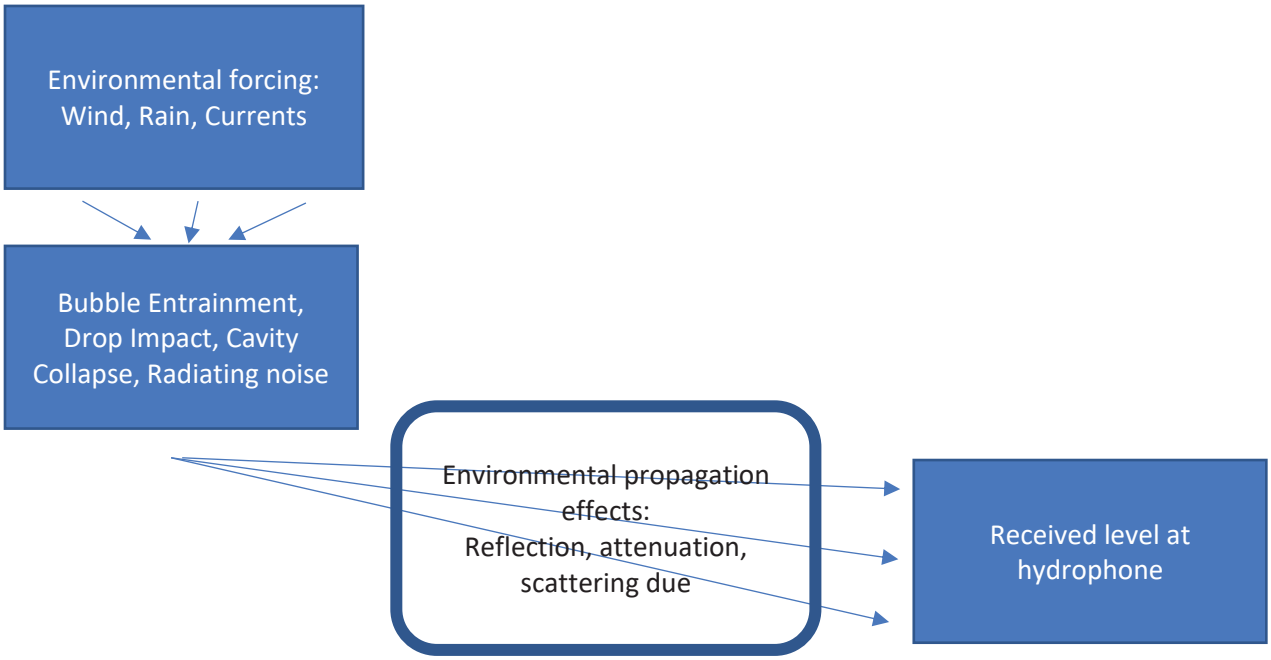

Figure 2: Schematic of sound in the marine environment, describing the path from noise generation as a result of environmental sources including wind and rain, through noise modification by transmission effects like reflection, attenuation, and scattering, to receiving the sound on an acoustic recorder.

The principle of wave superposition in the acoustic pressure field allow the received acoustic pressure time series, $x(t)$, to be represented as the sum of source time series,

$$x(t) = \tau(t_l)\{w(t) + r(t)\} + s(t) + \chi(t) \qquad Eq. 9$$

where $w(t)$, $r(t)$, $s(t)$, and $\chi(t)$ represent the signals attributed to sources generated by wind, rain, shipping, and unknown mechanisms respectively. $\tau(t_l)$ is a tidal scale amplitude modulation on tidal timescales, t_l, due to the effect of surface currents on surface noise source generation as well as the varying water depth that modulates the characteristics of transmission loss between the noise sources and receiver. The longer tidal timescale, t_l, is differentiated from t due to its implication in shifting a multiplication of time series into the frequency domain.

In practice, continuous acoustic pressure signals in the time domain are inseparable. An acoustic pressure series represents the instantaneous deviation in pressure from the hydrostatic background at the hydrophone and do not individually encode any information on their origin. An instantaneous 10 μPa difference from the rupture of a wave entrained bubble is the same as a 10 μPa difference from the impact of a raindrop, the grinding of tidally transported bed load, nearby shipping, or even a biological call like that of a whale.

Moving the acoustic pressure series into the frequency domain through a discrete Fourier Transform (DFT) allows sources to become separable through frequency content. Eq. 9 becomes

$$X(\omega) = T(\omega)\{W(\omega) + R(\omega)\} + S(\omega) + \Xi(\omega), \qquad Eq. 10$$

where *W, R, T, S* and Ξ are the Fourier transformed received, wind, rain, tidal effects, shipping, and unknown components of the signal. Over the time scale of the transform window, $\tau(t_l)$ is functionally constant and represents a simple scaling factor, rather than a convolution of two time series. The power becomes

$$\overline{\mathrm{X}} = \langle X(\omega)X(\omega)^* \rangle \; = \; T^2\{\langle W^2 \rangle + \langle R^2 \rangle\} + \langle S^2 \rangle + \langle \Xi^2 \rangle, \qquad Eq. 11$$

where the frequency dependence of all terms is implied, and uncorrelated cross-terms go to zero when the ensemble average is taken. Note that over the time scale of the ensemble averaging process, the tidal amplitude modulation is effectively constant and thus remains unbracketed. Fourier Transforms performed and ordered at multiple timesteps generates a spectrogram of the received signal, with dimensions of frequency, time, and intensity. With the added frequency information, it is now possible to correlate time series of received power by frequency to time series of environmental forcing.

In this study we are primarily concerned with measuring and predicting the sound field for natural, abiotic, background sources for two reasons. They are more conducive to being modeled across longer[4] timescales, and in nearly all cases are solely responsible for the baseline noise level in the absence of human activity. Lastly, there already exists a large body of research surrounding ocean bioacoustics, and a treatment in this thesis would be insufficient to do the field justice. Thus, ignoring shipping, Eq. 11 becomes

$$\overline{\mathrm{X}} = T^2\{\langle W^2\rangle + \langle R^2\rangle\} + \langle \Xi^2\rangle \qquad Eq.12$$

where wind $\langle W^2\rangle$ and rain $\langle R^2\rangle$ are all distributed sources (Farmer and Vagle 1988; Ma and Nystuen 2005), meaning that rather than originating from a point source, they originate from a random distribution of sources on a plane within the surface receive area of the hydrophone.

With wind driven breaking waves as an example, let dW, the complex pressure received from a single patch of ocean surface with area $dA = rdrd\theta$ at point $r = (r, \theta, z')$ and at frequency ω, be given by

$$dW(\omega) = Q_w P_w(r, \omega), \qquad Eq.13$$

[4] Weeks +

where Q_w is the source strength with units 1/length due to breaking waves and P_w is the complex pressure at the bottom mounted receiver located at the origin for a unit source. The total contribution of wind generated sources to the noise power impinging on the hydrophone is therefore the continuous sum of all such patches in the listening area of the hydrophone, given by

$$\langle W^2 \rangle = \int_0^{2\pi} \int_0^{\infty} {Q_w}^2 \; P_w {P^*}_w \, r \, dr d\theta \, , \qquad Eq. 14$$

where * indicates the complex conjugate. Note that the source density, ${Q_w}^2$, now has units 1/area ensuring that $\langle W^2 \rangle$ has units of $\mu Pa^2 Hz^{-1}$. Assuming a computationally discrete domain, Eq. 14 becomes the double sum

$$\langle W^2 \rangle = {Q_w}^2 \sum_m \sum_n P_w(m,n) {P^*}_w(m,n) \, r(m,n) \Delta r_{m,n} \Delta \theta_{m,n} \, , \qquad Eq. 15$$

where m, n are iterators for range and bearing, respectively. The values within the double summation may computed using a transmission loss model and are not related to the wind stress on the ocean's surface, the forcing considered in this example. For a fixed hydrophone, the computational result obtained using a known discrete transmission loss model can be summed and substituted into Eq. 15 to further to reduce it to

$$\langle W^2 \rangle = {Q_w}^2 NTL_w(\omega), \qquad Eq. 16$$

where the noise transmission loss $NTL(\omega)$, is now a simple scaling factor representing the listening area of the hydrophone and the propagation environment, including bathymetric and oceanographic effects. An identical expression to Eq. 16 can be written to describe the received rain noise power, $\langle R^2 \rangle$.

Eq. 16 demonstrates that a predictive noise model of received acoustic level parameterized by the forcing related directly to the acoustic source strength will rapidly lose its predictive ability as the distance from the recording location increases, or even when the

oceanographic environment is altered. To improve model portability to other regions, it is therefore useful to determine the relationship between an effective source level and the meteorological (wind speed and direction, rainfall rate) and oceanographic (surface current speed and direction) variables that drive natural underwater ambient sound, rather than a direct correlation between those variables and the measured noise.

Substituting the wind and rain variants of Eq. 16 into Eq. 12, gives a relationship between the received power and the source strengths for both wind-wave and rain generated noise

$$\overline{\mathrm{X}(\omega)} = T^2\left\{{Q_w}^2 NTL_w(\omega) + {Q_R}^2 NTL_r(\omega)\right\} \qquad Eq.17$$

where, for simplicity, the presence of additional unknown noise sources is assumed to be zero. If we assume the distribution of wind and rain sources is uniform over the entire listening area of the receiver, then $NTL_w = NTL_R = NTL$, noting that T is a small oscillation about unity and thus T^2 can be approximated as unity itself, then Eq. 17 can be expressed as

$$\left\{{Q_w}^2 + {Q_R}^2\right\} = \frac{\overline{\mathrm{X}(\omega)}}{NTL(\omega)} \qquad Eq.18$$

Eq. 18 shows that the relationship between the observed noise power and the source strength per unit area is a linear scaling defined by the transmission loss between all contributions of the distributed source and the receiver.

2.4 The common regression model

The linear combination of source terms in the received acoustic power shown in Eq. 12 lends itself well to regression against the respective environmental forcing terms. In general, a received signal can be represented as its central tendency, and associated process noise, namely:

$$y_i = \widehat{y_i} + \epsilon_i(0, \sigma^2) \qquad Eq.19$$

where y_i is the *i*th element of series y, $\widehat{y_i}$ is the central tendency, and the process noise $\epsilon_i(0, \sigma^2)$ having a zero mean, and some standard deviation, and where $\widehat{y_i}$ can be modelled through time as function of some predictor variable. Generalizing to the acoustic power series yields

$$\bar{X} = \widehat{T^2}\left\{ \widehat{W^2} + \widehat{R^2} \right\} + e_{WRT}(0, \sigma^2) + \Xi^2 \qquad Eq. 20$$

with $e_{WRT}(0, \sigma^2)$ representing the combined process noise of the wind and rain terms. In this formation, it is apparent that the residual of any single process against the received series is made up of the other processes, and their noise terms. Thus, by systematic fitting of different processes, in effect their linear combination in the modelled series, it is possible to remove predictable variation from the received series until all that remains is the sum of process noise which is due to natural variation in the processes themselves and the unknown noise Ξ^2, which may be physically attributed to mechanical noise generation on the receiver mooring or electrical noise in the data acquisition system. For poorly chosen form of the regression model, $e_{WRT}(0, \sigma^2)$ will appear unreasonably large, while for an inadequately defined ambient noise model, Ξ^2 will be large.

A non-zero process noise for wind generated ocean sound is expected, since the best source level estimates for individual breaking waves has a non-zero variance, and the size of the ensemble used to estimate $\langle W^2 \rangle$, which depends on receiver depth and channel geometry, is typically large. A probabilistic model of wind generated noise could be used to model process noise (Barclay and Lin 2019).

3 Methods

From January 2018 to present, continuous acoustic recordings from the Strait of Juan de Fuca, Salish Sea, and Gulf Islands in Coastal British Columbia (Figure 1) were collected with a goal of parameterizing an empirical noise model. Data were collected in conjunction with Department of Fisheries and Oceans (DFO) research scientists from the Institute of Ocean Sciences (IOS) in Sidney, BC, as part of a monitoring project led by Dr. Svein Vagle. A subset of the entire deployment (April 18 – May 12th, 2018) was selected from Station S to regress against, while the model performance was evaluated against the entirety of the acoustic recordings captured at the station until February 27, 2019.

3.1 Acoustic data collection

Acoustic records used in this thesis originates from the Sooke station (Station S, Figure 1) between April 2018 and February 2019 (Table 1) captured across five deployments. The moorings are bottom mounted, consisting of an anchor, buoyant payload attachment, and hydrophone mast (Figure 3), with an overall length just over four meters (Figure 4). The acoustic package deployed on each mooring consisted of the Autonomous Multi-channel Acoustic Recorder (AMAR) G4 acoustic recorder developed by JASCO, utilizing Geospectrum Technologies M36-100 hydrophones, with single and dual channel configurations. The AMARs were configured to record continuous pressure time series with a sampling frequency of 256 kHz with a 24-bit dynamic range, storing the information as 5-minute-long wave files. The hydrophones have a sensitivity of -165 dB re 1V/µPa over the band 5 Hz – 250 kHz, and, with anti-aliasing filters applied, the system has an acoustic bandwidth of 5 Hz – 100 kHz. An observed system noise floor above 20 kHz was centered around 40 $dB\ re\ 1\mu Pa^2Hz^{-1}$. Power

usage and data rates necessitated mooring recovery and redeployment every three to four months (Appendix 1).

Table 1: Schedule of 2018 to 2019 Sooke station (48° 17.365'N, 123°39.127'W) (-165 m) deployments used in this analysis, detailing deployment and recovery times, sensors, and deployment notes.

Deployment	Retrieval	Deployment notes	Environmental Sensors
		Stopped recording Feb 6 to Mar 6	
01-Feb	15-Apr	2018	JFE Advantech AEM USB flow meter
15-Apr	19-Jun		
19-Jun	17-Aug		RBR TR-1050
17-Aug	12-Oct	Participated in Aug 17th cruise	TDR-2050
12-Oct	29-Nov		
29-Nov	05-Mar	Stopped recording Feb 27	XR-420 CT

To maintain maximum sampling coverage through time, mooring maintenance cruises occurred every three to four months, performed on board the CCGS Vector. Procedures for a typical mooring overhaul follow, taking approximately 1 hour. Arriving on station, an acoustic modem is deployed to locate the mooring and trigger the redundant acoustic releases, separating the mooring from the anchor, allowing it to surface in visual range of the ship. Surfacing times are dependent on depth but are typically between 2 – 5 minutes. Once on board, the science payload is removed for data retrieval and replaced by a new deployment ready payload. Zinc anodes are checked for corrosion, along with all fittings and fasteners to avoid premature subsurface disassembly and are replaced if required. Remaining corrosion tolerances for zinc anodes are approximately 30%, while fasteners and fittings are 60%. The acoustic releases are re-programmed and fitted to a new anchor. The mooring is then re-deployed on station, and its seabed position and orientation localized via triangulation with the acoustic modem. When desired, in situ transmission loss characterization was then carried out with the ship at differ

ranges serving as a source, and environmental characterization collected via a ship borne conductivity, temperature and depth (CTD) profile.

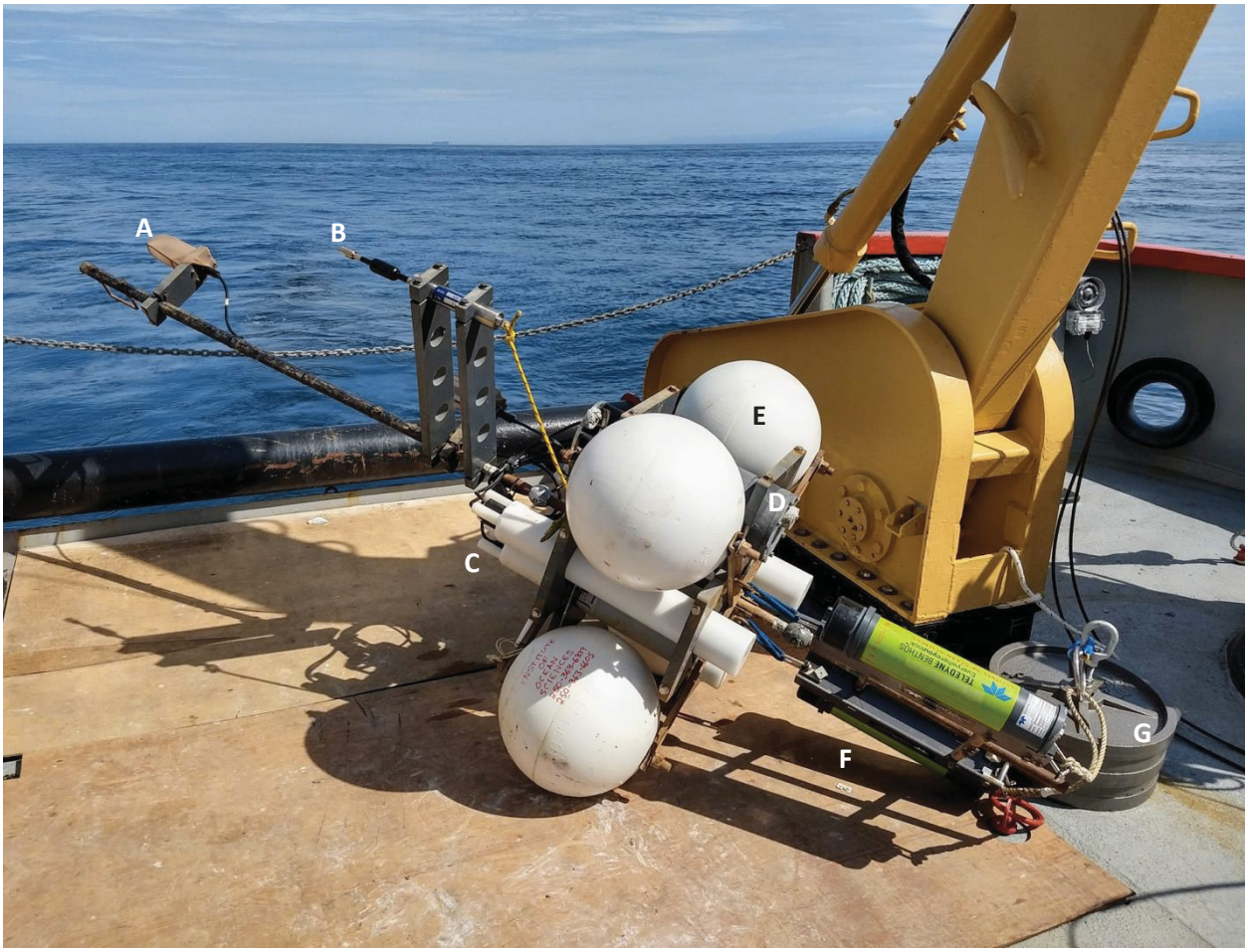

Figure 3:Submerged acoustic mooring system consisting of: (A) hydrophone (Geospectrum M36), (B) current meter, (C) AMAR, (D) auxiliary batteries, (E) buoyancy ring, (F) dual acoustic releases (Teledyne Benthos) for redundant retrieval, (G) 225 lb anchor.

Figure 4: Hands-on, hanging deployment of the mooring from the aft A-Frame of CCGS Vector, demonstrating in-situ mooring orientation. The author is to the left. Aug 17, 2019

3.2 Hydrophone Function and Calibration

A hydrophone is an electromechanical instrument designed to measure pressure fluctuations in a working fluid and is one component of an acoustic recorder, generating a signal passed to a pre-amplifier, analog to digital converter (ADC), and finally to a data logging device (Figure 5). It operates on a similar principle to an air microphone where a vibration induces an electric current, although rather than making use of a diaphragm and magnetic coil, it uses a cylindrical or spherical piezoelectric crystal deformed by pressure oscillations to generate a voltage difference across the inner and outer surfaces of the sensor. Piezoelectric systems are typically preferred for underwater sensing installations due to impedance matching with the medium of transference, a function of pressure wave speed and density of the fluid. Acoustic pressure variations result in small voltage differences which drive small current or voltage variations (depending on preamplifier design). This signal must be amplified to take advantage of the full dynamic range of the ADC before recording to storage, and the distance between the preamplifier and the piezo crystal is minimized. The ADC receives analog signals[5] and quantizes it as digital count value in comparison to some nominal reference voltage range. An acoustic pressure series can be represented and saved digitally by sampling the output of the ADC through time

[5] Continuous both in current and time.

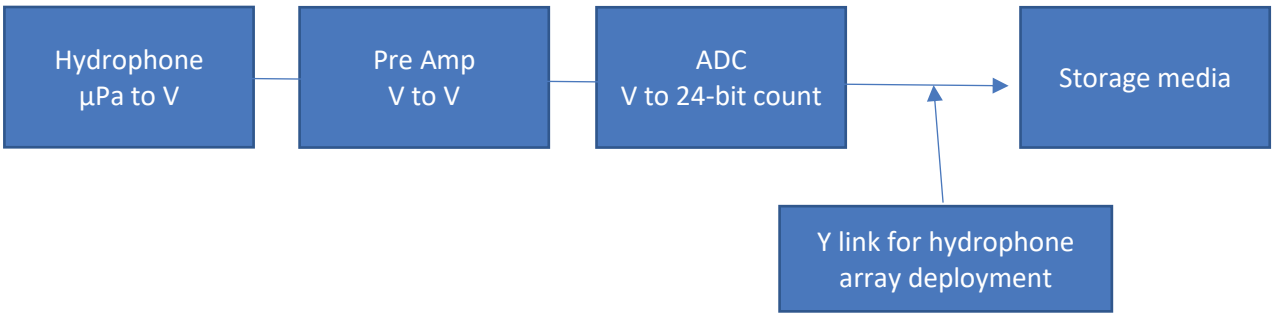

Figure 5: Schematic detailing the theoretical arrangement of systems in an acoustic recorder; including hydrophone, pre-amplifier, Analog to Digital converter, and Recording device.

Each piezoelectric transducer is an analog device with subtly different sensitivity and current generation in response to noise and therefore requires calibration, often performed in a controlled environment pre-deployment, and is represented as a free field sensitivity[6] spectrum in units of dB re 1V/µPa . Furthermore, the acoustic series has undergone significant amplification and transformation to be recorded, and thus must be back transformed prior to use. Calibration of the acoustic series used in this project followed the methodology outlined in Appendix A of the ADEON Hardware Specification version 2.3 (Martin et al. 2017). Wave files contain ordered collections of ADC count values, thus by scaling the count value by ADC voltage sensitivity and gain, hydrophone output voltage V_h can be reconstructed from digital records as in Eq. 21

$$C_{val} \times \frac{V_{ADC}}{N_{bit}} \times \frac{1}{G} = V_h, \qquad Eq. 21$$

where C_{val} is the ADC count value in the wave file, V_{ADC} is the voltage range in Volts of the ADC, N_{bit} is the bit depth of the ADC, and G is the amplifier gain in the system in Volts per Volt. The free field sensitivity of the hydrophone is a function of frequency, and thus the final calibration of volts to µPa is most conveniently applied in the frequency domain on a spectrum

[6] The voltage output of the hydrophone at known sound levels and known frequencies

of the hydrophone output voltage. Shifting both the hydrophone voltage spectrum and the free field sensitivity spectrum to dB simplifies this operation to a subtraction of the free field sensitivity spectrum level from the hydrophone voltage spectrum level following the logarithmic identity

$$log_{10}\left(\frac{A}{B}\right) = log_{10}(A) - log_{10}(B), \qquad Eq.22$$

where A and B are the hydrophone voltage level (dB re 1V) and the free field sensitivity level (dB re 1V/µPa) respectively. The result of the applying the calibrations in Eq. 21 and 22 to the digital signal recorded by the ADC, converted into a power spectrum by squaring the normalized output of discrete Fourier Transform, is the signal power in units of dB re 1µPa/Hz.

3.3 Oceanographic and meteorological data

Station S is located near the eastern mouth of the strait of Juan de Fuca, south of Vancouver Island in the Pacific North West (Figure 1). As the focus of this study is the prediction of the ambient noise field from environmental parameters, sources for wind, rain and tidal current velocity and direction are required as inputs for the model. The sections below outline the acquisition and basic processing of the environmental data used in the model.

3.3.1 Wind

Wind represents the single largest driver of underwater ambient noise through the mechanism of breaking waves, bubble entrainment, and bubble excitation. Thus, physically grounded, observational wind speed and direction are preferred. Race Rocks is a light station eight km east of Station S (Figure 1), located on an offshore reef (48° 17.898' N, -123° 31.896' W) and is the nearest weather station providing U_{10}, hourly wind speed (m/s) (Figure 6) and direction (degrees) at 10 m, accessed through the Environment Canada historical weather data

portal (ECCC 2020). The hourly wind speed is reported from the average speed during the one-, two- or ten-minute period ending at the time of observation while the wind direction is reported from the same data with 10-degree angular resolution. The co-location within the strait of Juan de Fuca; bounded by the Olympic mountain range to the south and Vancouver Island Range to the north, suggest that over eight km spatial scales the wind regime would remain relatively consistent between the acoustic and meteorological observations, and Race Rocks would be an adequate predictor of wind driven noise levels.

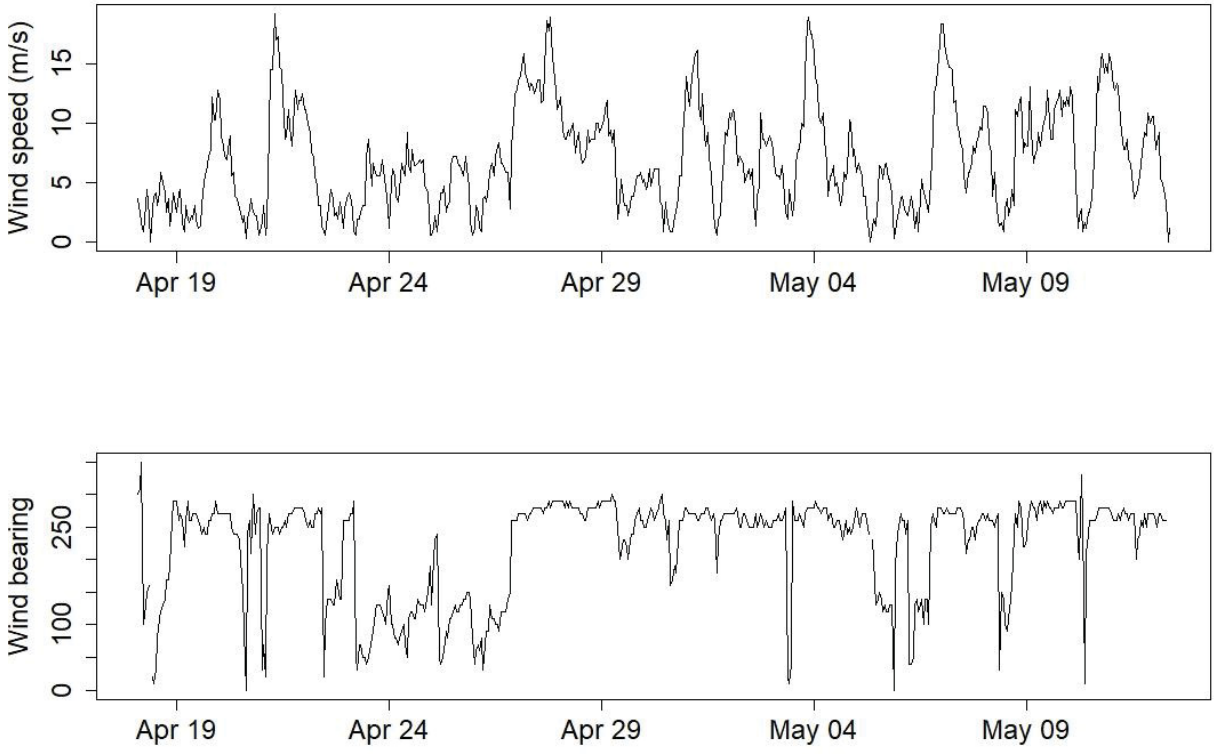

Figure 6: Example wind velocity and direction series generated for acoustic model formation. Data from Race Rocks light station between (April 18th and May 12th), Environment Canada.

3.3.2 Rain

In the Pacific North West, a region synonymous with heavy precipitation, rain is prominent contributor to the underwater soundscape due to drop impacts and cavity collapse leading to bubble entrainment (Nystuen et al. 1992). Spatially averaged hourly rain rate (mm/hr) at the deployment location was derived from Environment Canada PRECIP-ET Radar images (Figure 7). To automatically extract rain rate from a radar image, the deployment location of the acoustic recorder was localized in the image using the known locations of the cities and their on-image pixel location. While errors due a linear approximation on a spherical projection were a concern, it was mitigated by preferentially selecting known city coordinates near and fully surrounding the deployment location. Pixel colors on and surrounding the deployment location were then compared to the precipitation scale and subsequently averaged to provide a spatial composite estimate of rain rate and account for errors in color matching. Hourly radar images from 2018 – 2019 allowed for the formation for a time series of rain rate (Figure 8).

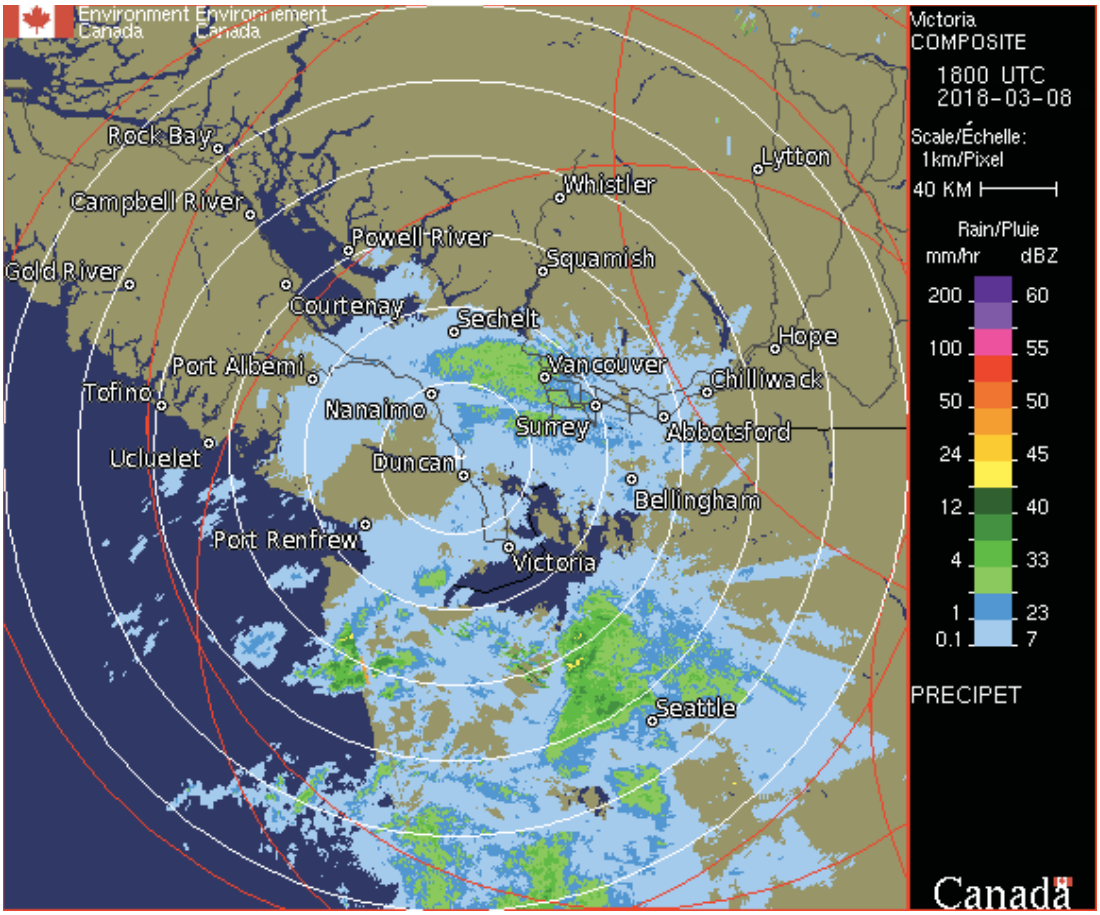

Figure 7: Example Composite PRECIP-ET radar image from March 8th, 2018 used to create local time series of precipitation at the deployment site. Environment Canada.

The time series of rain rate required further processing to separate true rain events from other radar anomalies including false returns from surface waves or heavy mist (ECCC). This was accomplished using a hysteretic peak detection algorithm with critical values of 0.02 mm/hr and 0.36 mm/hr, based on a 1-dimensional implementation of the Canny edge-detection algorithm (Smith 1998). Rain rates above 0.36 mm/hr were considered true returns, while rain rates below 0.02 mm/hr were immediately flagged as false returns. Values between 0.02 mm/hr and 0.36 mm/hr were considered true if they were adjacent to true returns, and false if they were isolated from returns. Through successive iterations, the true returns propagate out from values above 0.36 mm/hr until they cross the 0.02 mm/hr threshold, maintaining the shape of the lower

value regions of the rain events. Concern due to snow as another form of precipitation in this environment can be neglected due to the rarity of snow falling at sea level in this region (ECCC).

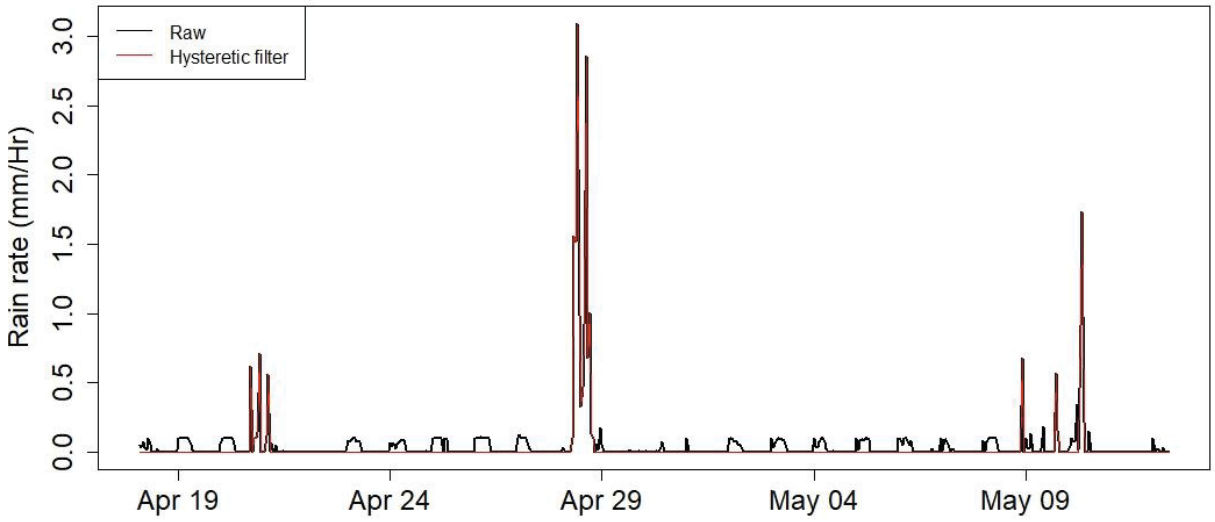

Figure 8: Example of rain rate time series before and after rain events were identified with a hysteretic filter algorithm based on a one-dimensional implementation of a canny edge detection algorithm.

3.3.3 Currents

The strait of Juan de Fuca has measurable tidal currents (Figure 9). As discussed in section 2.2, the environment and medium through which sound propagates can have a profound impact on the received sound pressure level (SPL). As the medium itself is moving, it is reasonable to include some form of periodic information to account for the tidal currents as they play a role in structuring the water masses in this complex coastal region and modifying surface noise generation processes, like current modulated wave steepening when wind direction is nearly constant. Other sources of sound that occur on tidal timescales including flow noise and saltation noise are not considered here since the first is outside of the band of interest and the second is not observed in the data. Current speed and heading information were captured by the

inductive flow sensor deployed on the mooring, however it suffered a battery fault attributed to a high duty cycle part-way through the deployment, resulting in a shortened training dataset of only 18 days between April 15th and May 3rd. To complement the observed tidal record, the Bedford Institute of Oceanography WebTide tidal prediction model (DFO 2009) was used to estimate current speed at the mooring location as it showed good agreement with the in situ measurements (Figure 10).

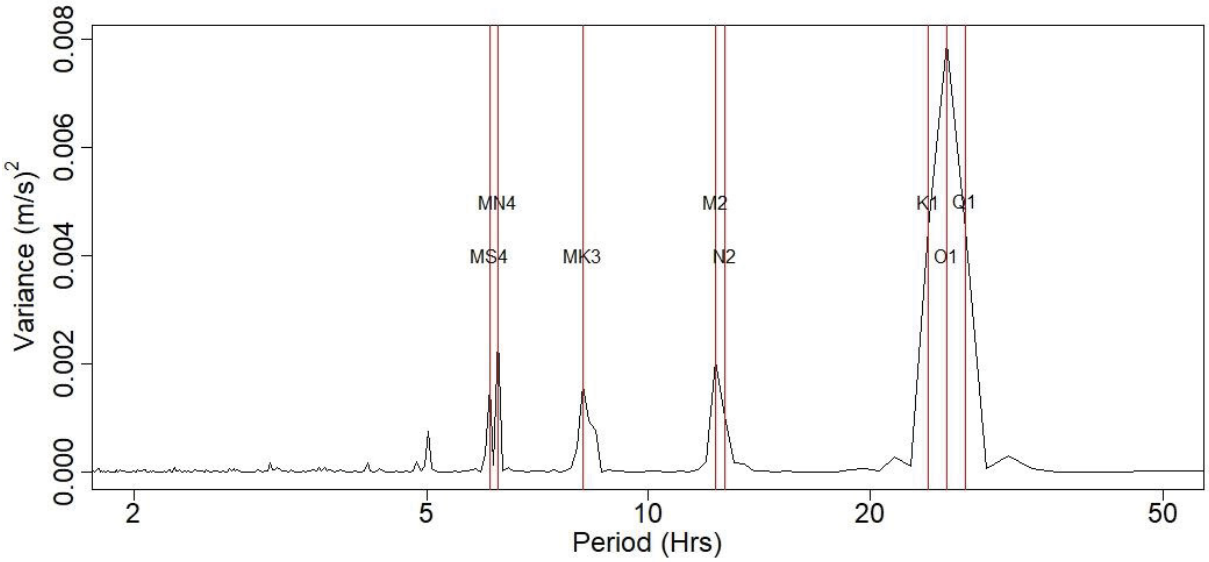

Figure 9: Periodogram of current velocity measured in-situ, overlaid with known tidal frequencies between April 15th and May 3rd, 2018.

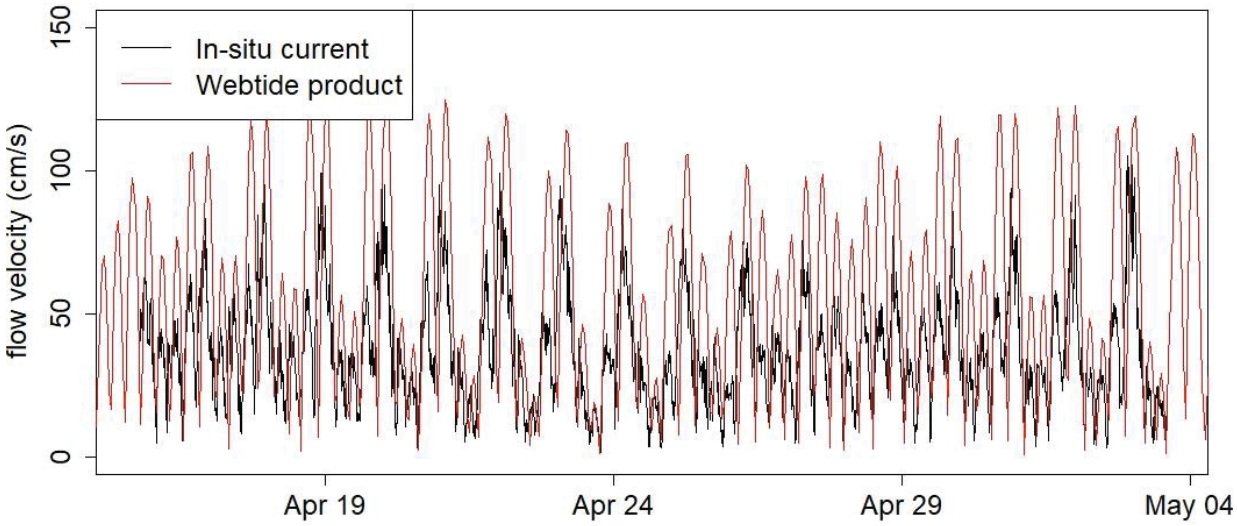

Figure 10: Comparison of current velocity captured in situ and modelled using DFO WebTide model between April 15th and May 3rd.

3.4 Data processing

The data analysis procedure for this project is designed to capture the linear behavior of the combined source terms in the region. The first minute of each five-minute wave file was isolated and used to calculate a representative spectrum with 1 Hz bins, over the band 5 Hz to 100 kHz) using the Welch method (Welch 1967) developing 119 one second spectra with 50 % overlap averaged together. It is assumed that the noise is stationary over the full five-minute file[7]. When spectra are ordered through time a spectrogram is formed, and time series of sound pressure level (SPL) in dB re $1mPa^2$ Hz^{-1} at each frequency is extracted to compare and iteratively corelate against time series of environmental parameters, first against windspeed (m/s) and then against rain rate (mm/hr), in a training data set. Lastly, harmonic regression of the fit

[7] As the recording is continuous, there is no duty cycling, and no startup noise.

residuals was performed at the tidal frequencies present in the observed and WebTide modelled current velocity series. This order of environmental parameters, wind, rain, then tide, was chosen to sequentially remove the largest source of variation, to improve the detection of effects of secondary environmental noise sources like rain and tidal modulation. The combination of the regression models was used to predict sound levels for the remaining acoustic records between April 18th, 2018 and February 27th 2019 and their fit was evaluated.

3.4.1 Filtration of acoustic power series

The Strait of Juan de Fuca is an acoustically diverse region due to the environmental noise sources described above, the biological sources like cetaceans supported by the rich ecosystem, and anthropogenic sources due to heavy surface traffic and marine development (Eng\aas et al. 1996; Lusseau et al. 2009; Olszewski and Ren 2015). Acoustic records therefore required filtering to isolate the ambient background signal prior to comparison and regression against environmental sources could begin.

Two filtering methods were used sequentially to isolate the environmental signal; hourly decimation to the mean, minimum, and maximum, and spectral component filtering to quantify spectral slope and identify sound source. Environmental data were collected at hourly intervals, in comparison to the five-minute intervals of the acoustic records, providing an opportunity to remove a portion of the non-environmental variability and short duration transients in the soundscape while aligning the sampling rates of the acoustic and environmental series.

Spectral component filtering is a method, proposed by Vagle et al 1990 and subsequently used by Nystuen et al 2010, of attributing acoustic records to specific sources through comparing the spectral shapes of different sources. Spectral shapes can be sorted and identified by plotting spectral levels of two or more frequencies against each other in a scatter-gram, where sources

will self-organize into groups (Vagle et al. 1990; Nystuen et al. 2010). In this configuration, records of broadband sources will self-organize about a line with a slope of unity and an intercept related to the consistent relative difference in spectral levels at the target frequencies. Sources that deviate from a slope of one indicate more narrowband source characteristics as they do not affect the spectrum equally. Wind, as a broadband source, closely follows the slope of one. Rain with its acoustic presence more pronounced at higher frequencies, is found above the wind line, while ship noise, with power concentrated in the lower frequencies, is found below the wind signal (Figure 11) (Nystuen et al. 2010). Spectral component cutoffs are found in Table 2. Following the example set by Nystuen et al, 8 kHz and 20 kHz were selected as the frequencies in this application. In doing so, wind, rain, and ship spectra are identified and flagged for later use in regression against their relative source.

Table 2: Cutoff functions for spectral component filtering. Values contained within these bounds are attributed to their respective sources.

Parameter	Domain
Rain	(SPL 20kHz) > (SPL 8kHz) - 6.6 dB, (SPL 20kHz) > 54 dB
Wind	(SPL 20kHz) < (SPL 8kHz) - 6.6 dB, (SPL 20kHz) > (SPL 8kHz) - 9.8 dB
Shipping	(SPL 20kHz) < (SPL 8kHz) - 9.8

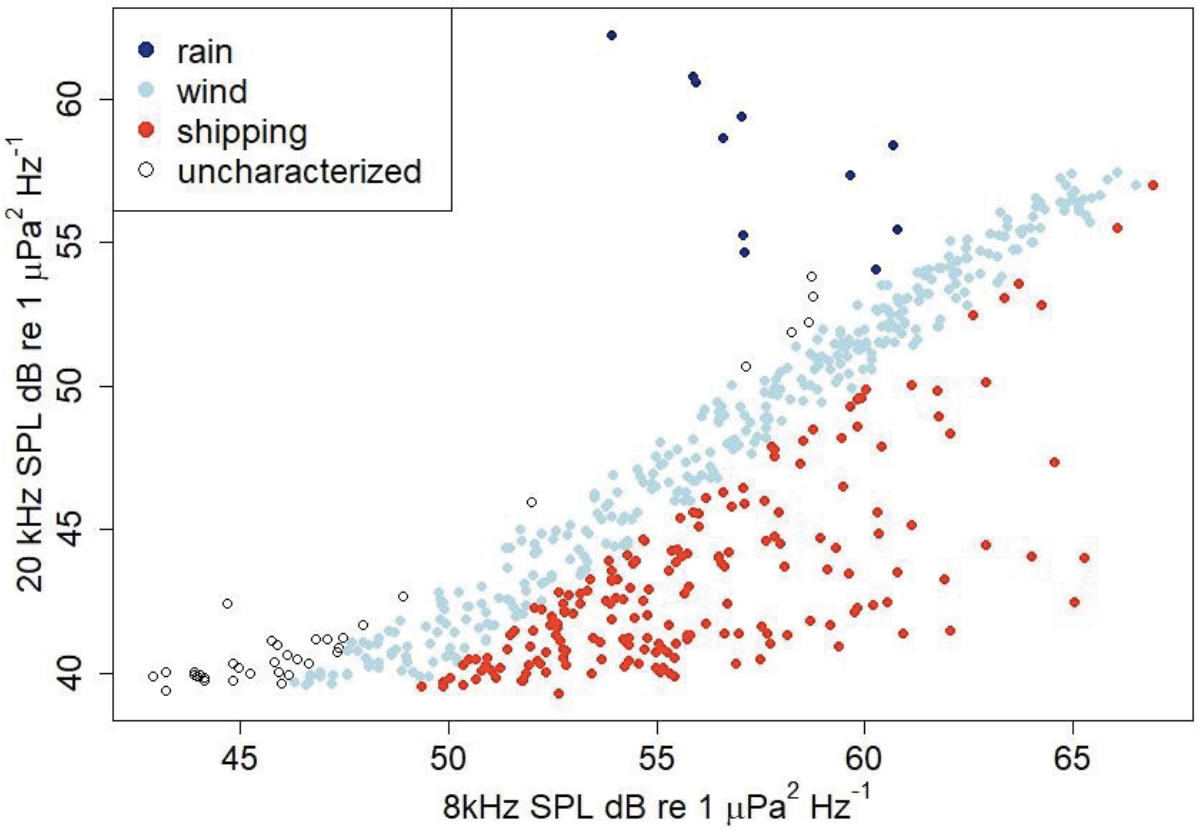

Figure 11: Spectral component scatter-gram whereby different acoustic sources self-organize into distinct regions. Rain noise (dark blue) is categorized by relatively higher noise levels at high frequencies, while shipping noise (red) is categorized by relatively higher noise levels at lower frequencies. Wind noise (light blue) follows quasi-linear relation in the center of the plane, uncharacterized points are unfilled. Method adapted from Nystuen et al. 2010.

3.4.2 Fitting wind

Wind flagged SPL in $dB\ re\ 1\mu Pa^2 Hz^{-1}$ records were regressed against concurrent observations of wind speed as the predictor for each frequency, using first, second, and third order polynomials and a piecewise continuous function. Testing SPL records for normality showed a bi-modal distribution (Figure 12), suggesting a wind regime change and motivating the use of a piecewise continuous function comprised of two segments above and below a windspeed

breakpoint. A second order polynomial regression was used above the breakpoint while below, a linear fit was forced through the 1st percentile SPL at 0 m/s and the extrapolated 10th percentile of the regression above the breakpoint. This ensures continuity at the potential expense of improved R^2 values. Wind speed was not log transformed as in earlier studies (Vagle et al. 1990) as it shifted the distribution of wind further away from normality (Figure 12).

Though the regression model of wind was computed in logarithmic space inherent to the units of dB re 1μPa^{2}Hz^{-1}, the residual resulting from the wind fitting procedure, $\overline{X_{-w}} = \bar{X} - \widehat{W^2}$, was calculated in linear space in units of $\mu Pa^2 Hz^{-1}$. Since T^2 is assumed to be oscillatory with an unknown frequency w_0 taking the form $T^2 \propto e^{i\omega_0 t}$ and to have a small amplitude relative to variations in $\langle W^2 \rangle$ and $\langle R^2 \rangle$, we can express it as a Taylor's series and keep only the leading term. Subtracting the model produced from Eq. 12 gives

$$\overline{X_{-w}} = T^2\langle R^2 \rangle + \langle \Xi^2 \rangle + \varepsilon_W, \qquad Eq. 23$$

The residual $\overline{X_{-w}}$ is then converted back to dB for meaningful use in fitting a model for the next environmental parameter, rain fall noise.

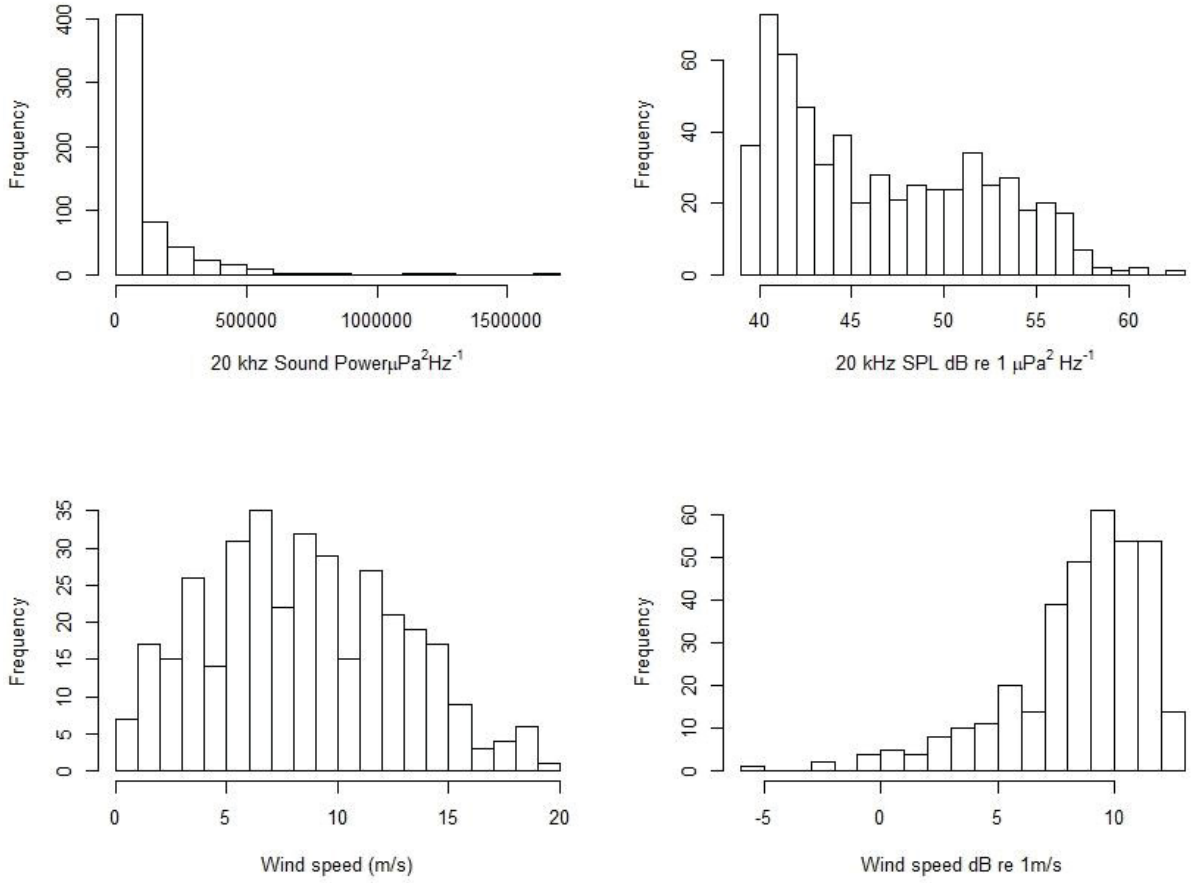

Figure 12: Histograms of untransformed linear (left) and dB (right) transformed logarithm time series of sound pressure (μPa^2 Hz^(-1)) (top) and wind speed (m/s) (bottom).

3.4.3 Fitting rain

Rain represents a complex acoustic source, as it generates noise from drop impact and impact cavity collapse. This is further confounded by the increase in drop size seen with rain rate, and the effects of rain impact grazing angle (Ma and Nystuen 2005). Following their recommendation, the residual SPL, given by $10log_{10}(\overline{X_{-w}})$ were linearly regressed against $10log_{10}\left(\frac{\xi}{U_{10}}\right)$, where $\boldsymbol{\xi}$ is the rain fall rate, the time series of rain events measured in units $\frac{1mm}{Hr} * 1\ s/m$. Noise levels were always underestimated by the preceding wind portion of the

model during rain events, so $\overline{X_{-w}}$ is always positive, allowing for meaningful transformation into logarithmic space[8]. This regression takes the form of a simple power law in linear space which could be predicted by physical models based on drop sizes. Assuming a raindrop has reached terminal velocity towards a relatively flat sea surface, the average impact grazing angle is primarily a function of the drop's lateral velocity, itself is a function of wind speed. As a first order approximation it is fitting to scale the rain rate by the wind speed prior to transforming it into logarithmic space. This is the result of the relationship between the grazing angle $\boldsymbol{\theta}$ and the inverse tangent of the ratio of vertical $\boldsymbol{v_y}$ to horizontal velocities $\boldsymbol{v_x}$

$$\tan\theta = \frac{v_y}{v_x}. \qquad Eq.24$$

The regression between $\overline{X_{-w}}$and the ratio of rain fall rate and windspeed produces a model of rain generated noise, $\widehat{R^2}$. Under the same assumptions that T^2 is both oscillatory with a small amplitude relative to $\langle W^2 \rangle$ and $\langle R^2 \rangle$, the residual can be computed again as

$$\overline{X_{-w-R}} = \langle \Xi^2 \rangle + \varepsilon_{WR}. \qquad Eq.25$$

In this case the residual has lost its dependence on T^2, as that second order variation has been absorbed into the process noise for both the wind and the rain. However, to determine the tidal amplitude modulation component of the model using regression, the residual can be computed in logarithmic space.

[8] An important distinction should be made between residuals in µPa which are transformed into dB, and residuals calculated in dB, given that residuals in µPa represent a Euclidean distance, while those calculated directly in dB represent a scaling factor. Furthermore, it is not possible to calculate the logarithmic units of a negative value.

3.4.4 Fitting tidal components via harmonic regression

Harmonic regression is a linear regression schema where the predictor variables are a trigonometric function of a single variable (Hamilton 2020) – typically time. Due to the repeating nature of harmonic regression, it performs poorly on timeseries with a large and temporally inconsistent variance. Post-rain, untransformed residuals have a large variety of positive and negative amplitudes[9], which without pre-processing is a sub-optimal application of harmonic regression. Scaling raw residuals into level space to account for the dynamic range proves difficult as negative values are undefined when transformed in dB space. The residuals feeding the harmonic regression were calculated as the difference in dB between the modeled series and the observed series,

$$dB_r(\omega,t) = 10log_{10}(|\bar{X}|) - 10log_{10}\left(\widehat{W^2} + \widehat{R^2}\right) = 10log_{10}\left(\frac{|\bar{X}|}{\widehat{W^2} + \widehat{R^2}}\right), \qquad Eq.26$$

with the distinction that rather than informing further linear combination, it would represent a harmonic scaling function. In the ambient noise model presented in Eq. 12 this corresponds to T^2, the amplitude modulation of surface noise processes by tidally driven currents

The full mechanics of the tidal modulation are potentially quite complex, as it impacts both sound transmission through changing water depth, water mass structure, and generation through wind-wave-current interaction. As such, rather than directly fitting time series of observed or modelled current speed to the dB residuals, harmonic regressions were carried out at critical frequencies identified in the observed tidal series (Table 3). To capture phase information, both sine and cosine series were fit at the critical frequencies in the form

[9] Due primarily to the large dynamic range of associated with untransformed acoustic pressure measurements

$$\widehat{T^2} = \sum_{i=1}^{6} A_i sin(\omega_i t) + B_i \cos(\omega_i t), \qquad Eq. 27$$

where A_i and B_i are the frequency dependent coefficients of the i[th] critical frequency identified in the tidal series, and ω_i is the i[th] critical frequency. Each sine cosine pair in this series can subsequently be recombined with the identity

$$\mathrm{C}_i \sin(\omega + \varphi) = \mathrm{C}_i \sin(\omega)\cos(\varphi) + \mathrm{C}_i \cos(\omega)\sin(\varphi). \qquad Eq. 28$$

Given constant phase yields constant $\sin(\varphi)$ and $\cos(\varphi)$, and by the Pythagorean theorem (Eq. 28),

$$A_i{}^2 + B_i{}^2 = \mathrm{C}_i{}^2, \qquad Eq. 29$$

$$A_i = \mathrm{C}_i cos(\varphi), \qquad Eq. 30$$

$$B_i = \mathrm{C}_i sin(\varphi), \qquad Eq. 31$$

such that Eq. 27 can be written equivalently as

$$\widehat{T^2} = \sum_{i=1}^{6} C_i sin(\omega_i t + \varphi_i), \qquad Eq. 32$$

where C_i is a new frequency dependent coefficient of the i[th] critical frequency, and φ_i is the phase of harmonic regression.

Table 3: Critical frequencies identified in the observed tidal frequencies, subsequently targeted in harmonic regression.

Nearest Darwin Symbol	Period (hrs)	NOAA order
MS4	6.08	37
MN4	6.26	10
MK3	8.15	8
M2	12.34	1
N2	12.71	3
K1	24.00	4
O1	25.41	6
Q1	27.00	26

3.4.5 Modelling through time and evaluation of performance

Frequency dependent coefficients and model structure were extracted for both the wind and rain dependent models generated in the fitting process and used to predict hourly noise levels each month between April 2018 and February 2019. As the harmonic regression used to account for tidal mechanics did not directly make use of any time dependent input, it was applied *a posteriori* to each month at the identified critical frequencies, taking into account month to month differences in phase and superposition of long terms signals not identified in in the analysis of tidal signals. Applying the model by frequency and through time results in the formation of a spectrogram that can then be compared to the spectrogram of the acoustic recording.

The goodness of fit was modelled through time via the creation of a dB difference spectrogram, representing the scale difference between the observed and modelled spectrograms by computing

$$\Delta(\omega, t) = 10log_{10}\left(\frac{|\bar{X}|}{\widehat{T^2}\{\widehat{W^2} + \widehat{R^2}\}}\right) \qquad Eq. 33$$

While two-dimensional plots of Δ are useful to identify temporal errors in the model, for a quantifiable estimate of model performance by frequency, the root mean squared (RMS) of Δ was computed by

$$\Delta_{RMS}(\omega) = \sqrt{\frac{1}{N}\sum_{n=1}^{N}\Delta^2} \qquad Eq. 34$$

where N is the number of samples considered in the model data comparison. Monthly $\Delta_{RMS}(\omega)$ values by frequency can then be combined into a representation of model performance across the

full deployment, highlighting seasonal effects that are beyond the ability of the training dataset to resolve. An RMS under 3 dB is desired as it constrains the model performance to predict untransformed sound power ($\mu Pa^2 Hz^{-1}$) to within a factor of two.

3.5 Transmission loss modelling of distributed sources

By invoking the principle of reciprocity, the transmission loss between a large distributed source and a receiver can be efficiently modelled (Barclay and Lin 2019). Wind and rain noise are well described by an infinite plane of uniformly distributed monopole sources placed just below the sea surface. By placing a modeled source and the location of the experiment receiver, the amplitude and phase of the pressure arriving at the receiver from each patch of noise sources can be modelled in a single instance. In this study, a Nx2D ray tracing model is used where seabed geoacoustic properties are assumed to be uniform and a range and azimuth independent iso-sound speed profile with c = 1500 m/s is used. Horizontal refraction and reflection are not permitted in this study though, in general, the chosen model may be arbitrarily complex.

The model bathymetry is the GEBCO 2020 global terrain model for ocean and land (GEBCO Compilation Group 2020) with 15 arc second resolution, shown in Figure 13. The experimental receiver and model source location is shown by red circle, at a depth of 4 m above the seabed.

The compressional sound speed of the seabed was chosen as c_p=1640 m/s with a compressional attenuation of α_p = 0.5 dB/m and a density of 1700 kg/m^3 based on data from the dBseabed global seabed database (Jenkins 2010). The seabed is modelled as a fluid infinite half-space, since for the majority of the frequency band considered here (1 kHz – 20 kHz), sub-bottom properties and layering do not have a large impact on the propagation. In the water

column, Thorpe's analytical expression for frequency dependent absorption is applied (Thorp 1967).

Bellhop, the raytracing model employed, is configured to compute the 2D pressure field calculations along 10 km radials, with 1 m range resolution emanating from the source location with an azimuthal resolution of 6 degrees. The pressure field is computed by summing (coherently) for each range-depth grid cell over the amplitude of rays, accounting for the relative phase of each ray. Ray paths are given an effective width using a Gaussian cross-sectional area. For each radial, 2000 rays were launched between the angles -89.9 to 89.9 degrees relative to vertical. An example of the computation in terms of the transmission loss as a function of range and depth along a bearing of 45 degrees (north-west) is shown in Figure 14.

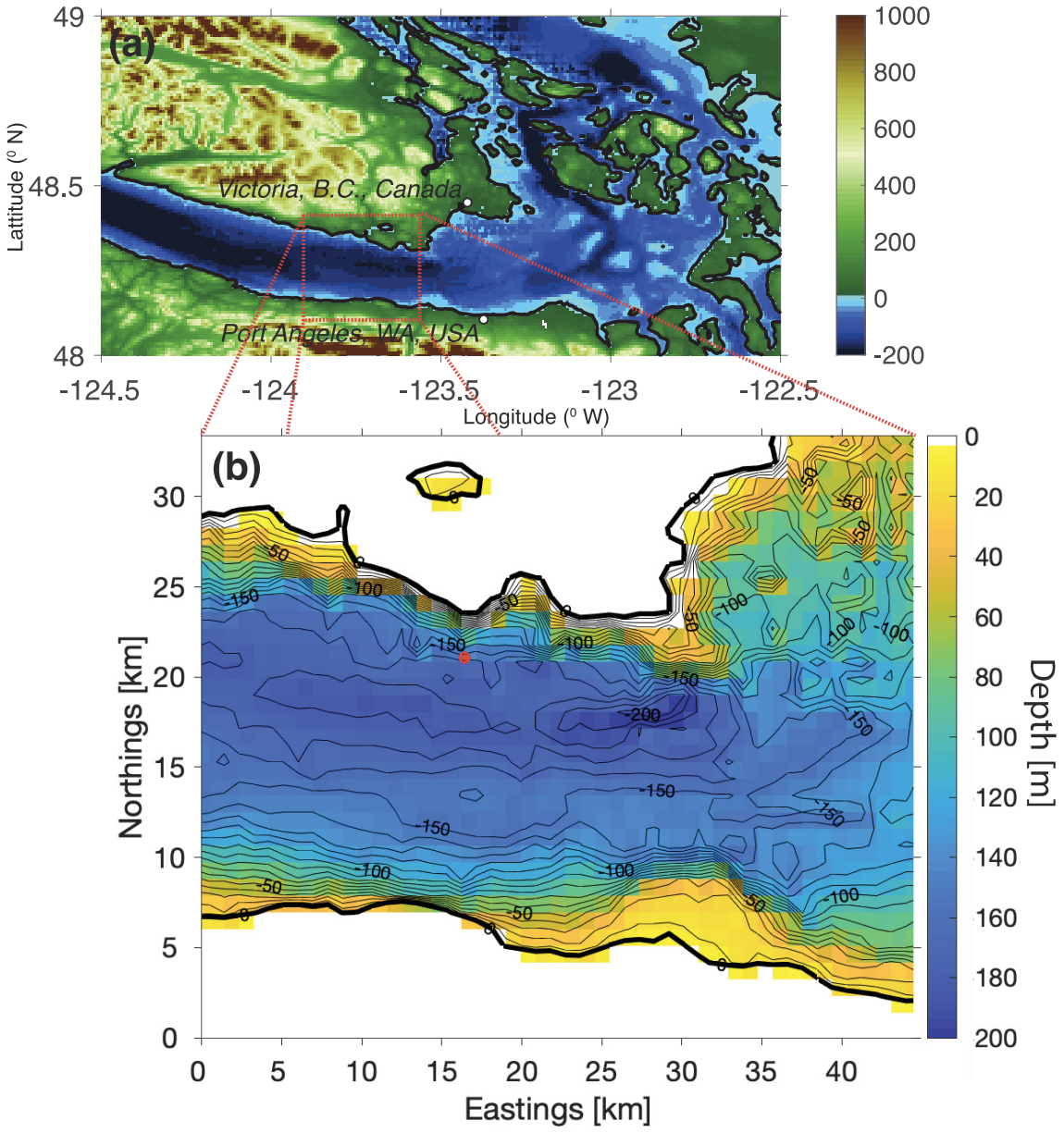

Figure 13: a) The Salish Sea with b) the model domain bathymetry from the GEBCO ocean data with 10 m contours shown by the black lines and the receiver location shown by the red circle.

The computed pressure field at a depth of 0.5 m is then mosaiced to produce a 2D plan view of the surface receive sensitivity, or the sensitivity of the receiver to each discrete area of the ocean's surface, shown in terms of transmission loss in Figure 15 at 1, 5, 10 and 20 kHz. The pressure field is summed over, accounting for the area represented by each pixel, following Eq. 15 and producing a value for *NTL* at that frequency.

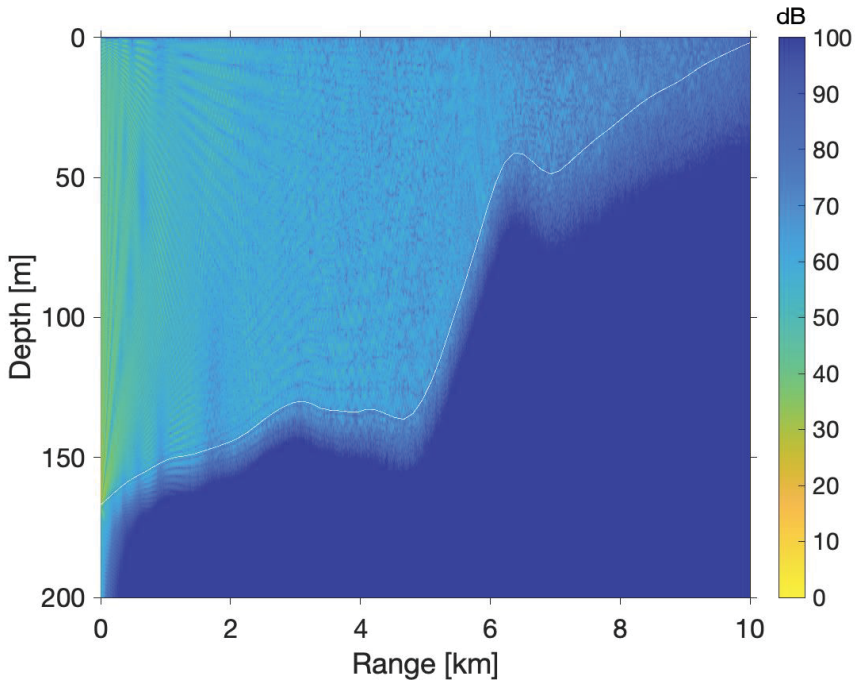

Figure 14: The modelled transmission loss along the radial in the 45 degrees (North-West) bearing direction, with the source placed 4 m from the bottom, computed at 1 kHz.

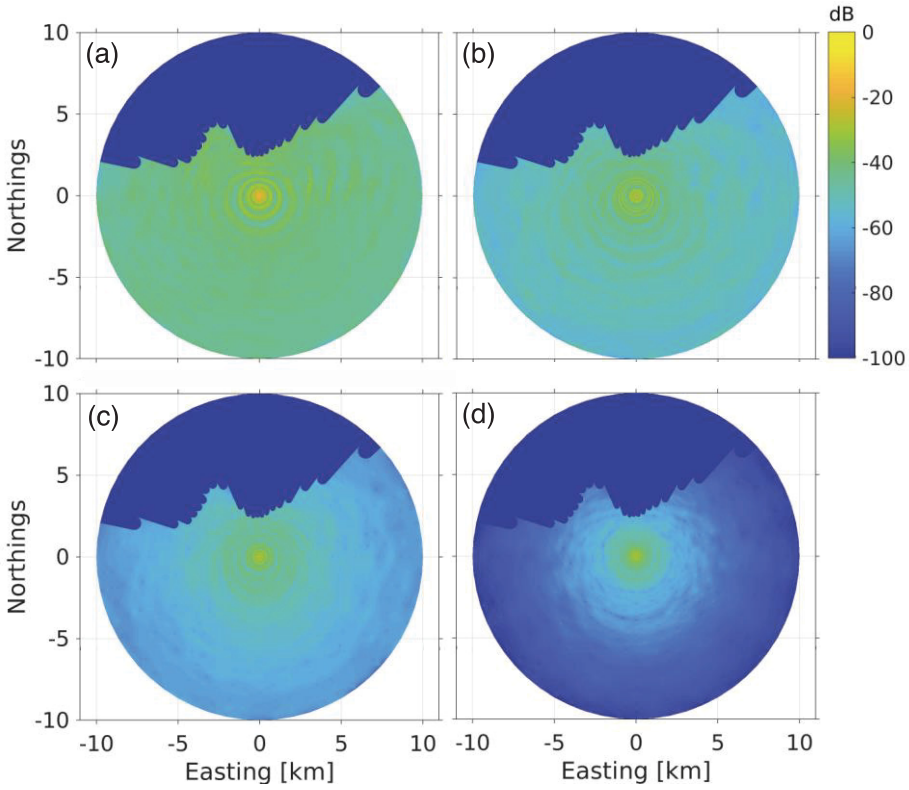

Figure 15: The modelled surface receive sensitivity, or transmission loss at a depth of 0.5 m, for the receiver placed at the origin, computed at a) 1 kHz, b) 5 kHz, c) 10 kHz, and d) 20 kHz.

4 Results

4.1 Wind

Comparing the time series of SPL to time series of absolute wind speed, the dominant natural source of ambient noise through the breaking wave mechanism, it is readily apparent that the minimum hourly sound level correlates well with absolute wind speed (Figure 16). Maximum sound level does not correlate well and mean sound level falls in between. Correlation is not consistent through frequency, with frequencies below 2.5 kHz having a small relation to wind, while above 2.5 kHz, it is the dominant forcing term, as seen in Figure 17. The maximum coefficient of determination achieved was 0.58 at 20 kHz. Down sampling to hourly minimum sound levels reduces the number of data records used in the model fitting from 6993 to 584.

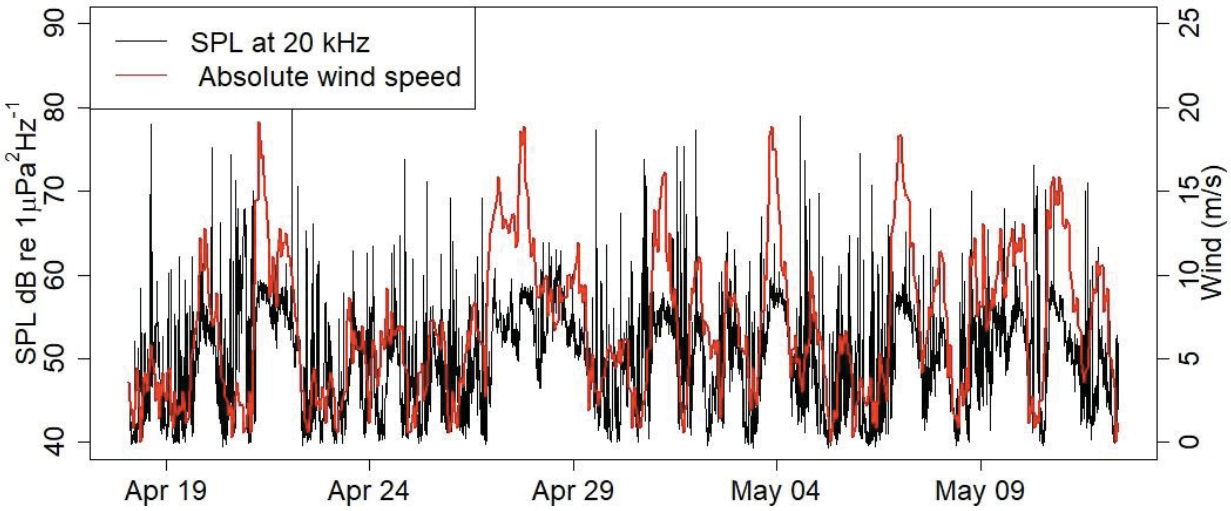

Figure 16: Time series of noise level (SPL dB re 1µPa^{2}Hz^{-1}) at 20 kHz superimposed over local absolute wind speed (m/s) collected at Race Rocks Light station.

Improved correlation was possible by taking advantage of the different spectral shapes of different sources, and further isolating SPL samples that are uncontaminated by sources other than wind generated noise. Regressing wind speed against wind-flagged spectra increased

correlation markedly, with a maximum coefficient of determination of 0.66 at 39.4 kHz (Figure 17). Correlation remains inconsistent across frequencies; however, the frequency at which divides the weakly correlated from the highly correlated sections of the spectrum is consistent at 2.5 kHz. Spectral component filtering further reduced the number of useable records to 350 over the training interval.

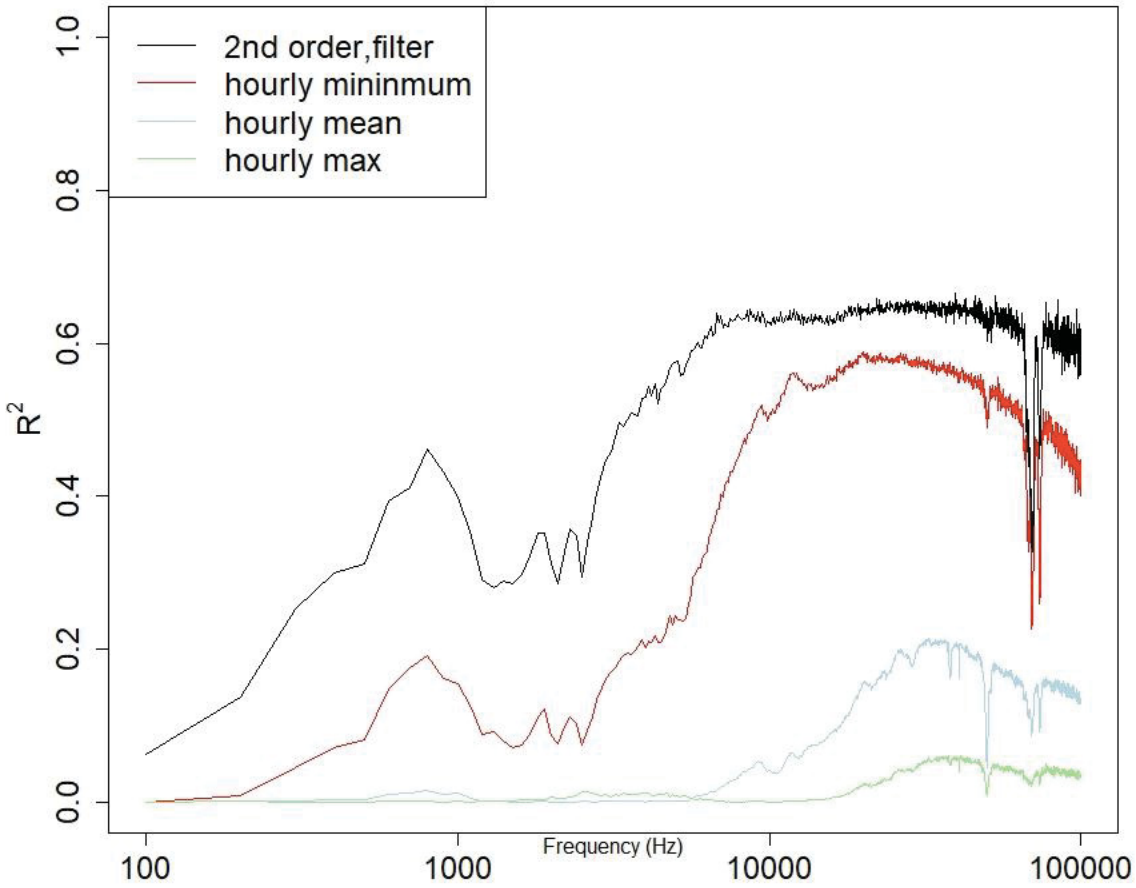

Figure 17: R^2 as a function of frequency for linear relationship between hourly minimum, mean, and maximum noise power level and wind speed (m/s), and model after spectral component filtering.

The best regression function found for wind was in the form of a piecewise polynomial due to the clear presence of different wind regimes above and below 5 m/s, shown in Figure 18. The general form for the fit is

$$10log_{10}(W^2(\omega)) = \begin{cases} Au^2 + Bu + K, & u > 5\frac{m}{s} \\ Mu + D, & u \leq 5\frac{m}{s} \end{cases}, \qquad Eq. 35$$

with the coefficients A, B, K, M, D all being frequency dependent and u being U_{10} wind speed in m/s. Local model data comparison achieves an error RMS of 3.5 dB at 20 kHz (Figure 19 A). The residuals of the model contain three large anomalous errors and minor periodicity (Figure 19 B).

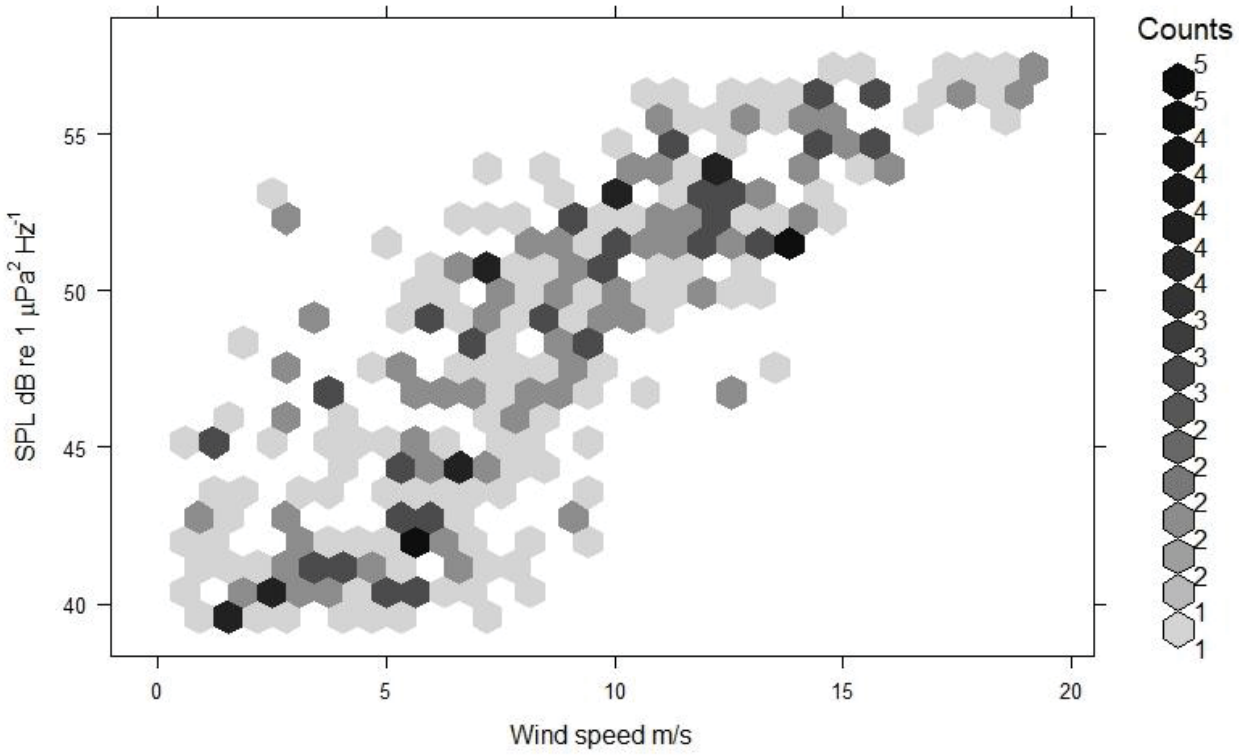

Figure 18: Two-dimensional histogram demonstrating the high and low wind regimes present, with a breakpoint at 5 m/s.

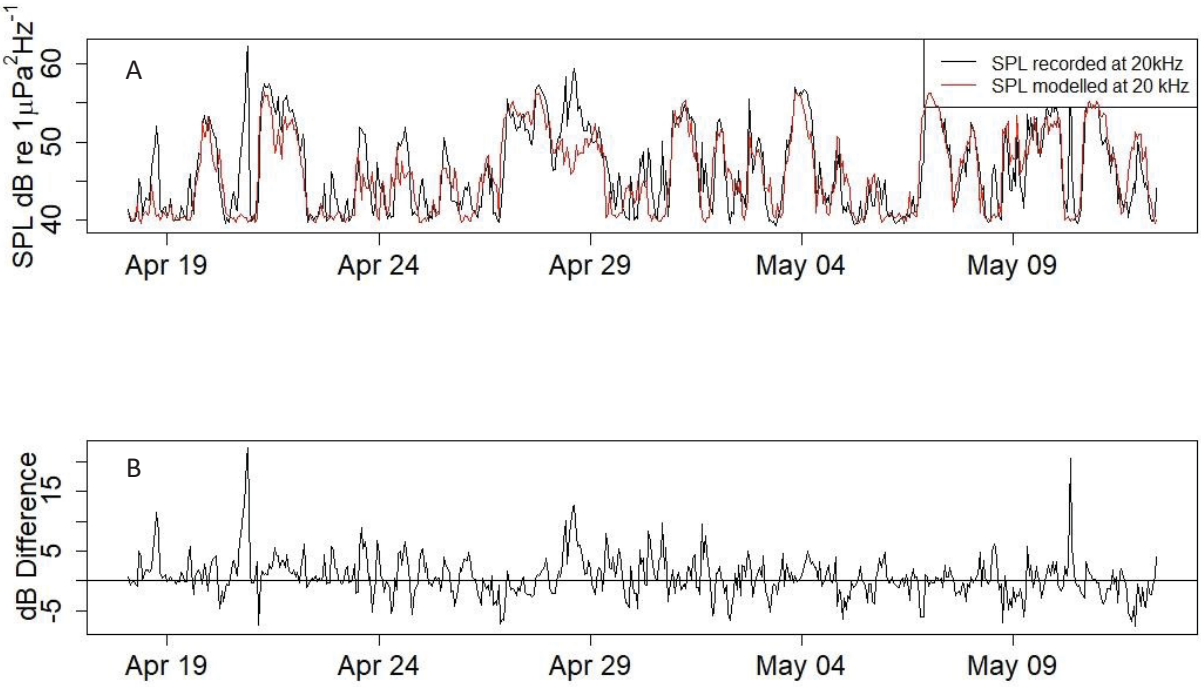

Figure 19: A) Local 20 kHz wind noise model-data comparison through time. B) Data-model differences calculated as the difference between predicted noise level and recorded noise level. Large deviations represent rain events, and cyclic variations appear tidal in timescale.

4.2 Rain

In comparing the residual acoustic power time series to that of rain rate, it is apparent that the large anomalies present are attributable to rain events due to their alignment in time (Figure 20). Linear correlation between the absolute rain level (dB re 1 mm/Hr) and residual noise level (dB re 1 μPa^2Hz^{-1}) again shows variation through frequency, with a maximum R^2 of 0.46 at 67.9 kHz (Figure 21 A), and a critical frequency of (11 kHz). Correlation between residual acoustic power and rain rate scaled by wind speed (dB re 1mm/Hr * 1s/m) shows a reduced R^2 across most frequencies (Figure 21 A) and an improved RMS error values across the training dataset by frequency when combined with the wind source model as described in Section 4.1 (Figure 21 B).

In this case, improved RMS is preferred over improved R^2 as it represents better cumulative model performance, rather than its ability to fit a single facet of the environment.

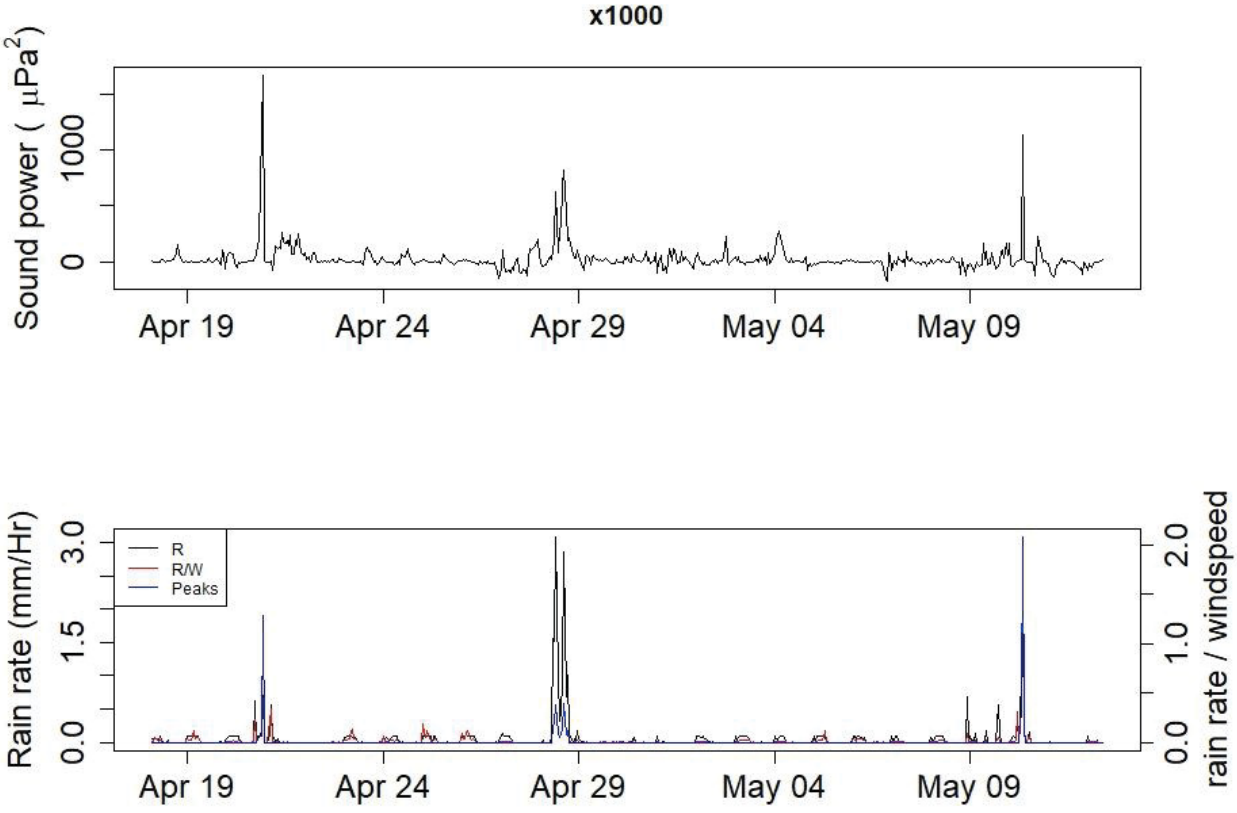

Figure 20: Top) Example time series of wind residuals at 20 kHz. Bottom) Raw, wind scaled, and wind-scaled filtered rain rate.

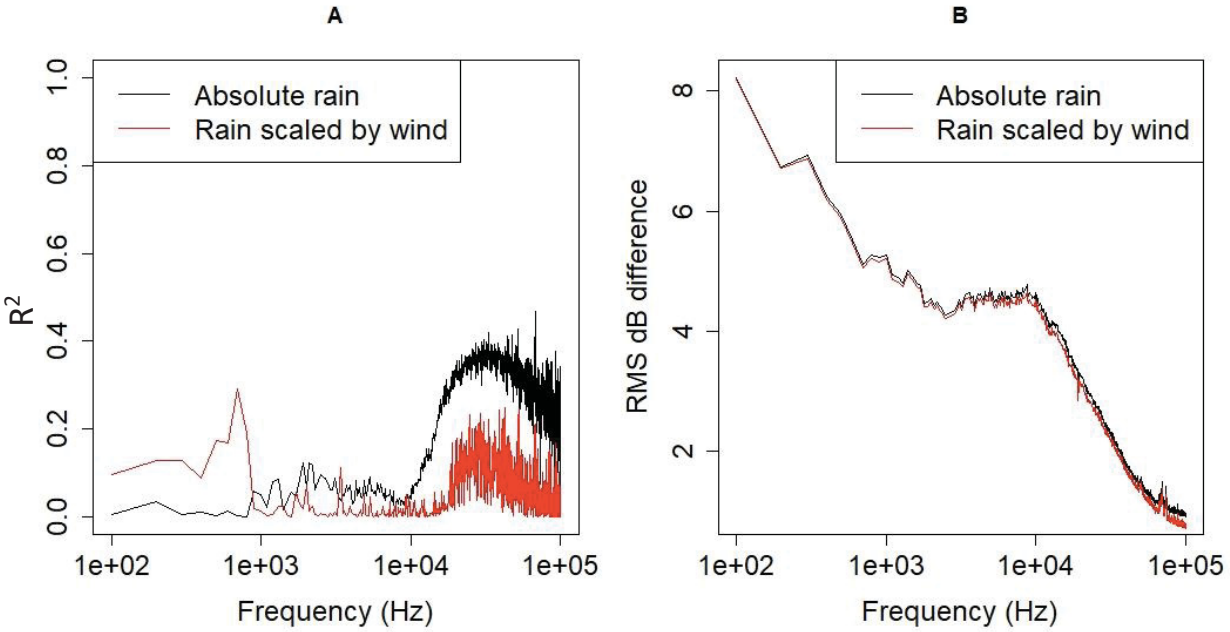

Figure 21: A) Spectra of coefficient of determination (R^2) of raw and wind scaled rain model. B) Spectra of total model dB difference after applying raw and wind scaled rain model

The best rain driven regression model is therefore the linear regression

$$10log_{10}(\overline{X_{-w}}) = G * 10log_{10}\left(\frac{\xi}{U_{10}}\right) + H\,, \qquad Eq.36$$

where G and H are fitted coefficients, where $\boldsymbol{\xi}$ is the rain fall rate, and the time series of rain events is measured in units $\frac{1mm}{Hr} * 1\ s/m$. Representing Eq. 36 in natural units reduces it to a power law,

$$(\overline{X_{-w}}) = \alpha\left(\frac{\xi}{U_{10}}\right)^{G}, \qquad Eq.37$$

where

$$\alpha = 10^{\frac{H}{10}}. \qquad Eq.38$$

Model performance is adequate, removing the large transient anomalies in the residual acoustic power series shown in Figure 22, reducing the RMS of the dB difference in the training data set from 3.53 to 2.99 at 20 kHz.

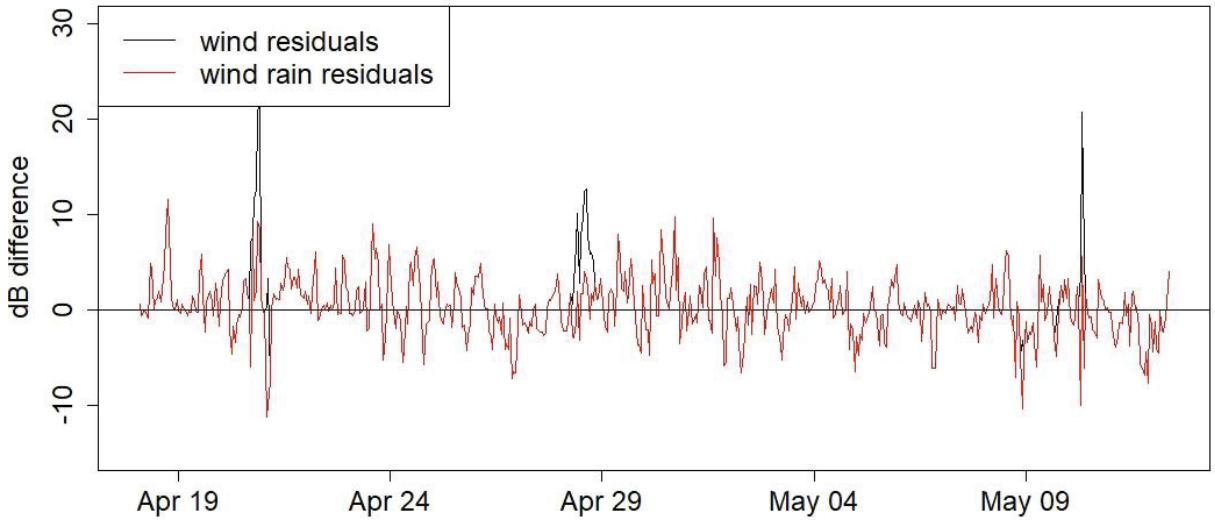

Figure 22: Example of data-model dB residual time series of the training dataset before and after the addition of rain driven acoustic events at 20 kHz. Note the presence of cyclic variations in amplitude occurring on approximately tidal timescales.

4.3 Amplitude modulation at tidal timescales

The Strait of Juan de Fuca can be considered a large tidal channel over which wind blows with a relatively consistent westerly direction. This motivates the need to include some capacity to capture the modulation in the wind and rain noise signals on tidal time scales in the model. Additive noise sources maybe present on these time scales as well, at lower frequencies (< 1 kHz) where flow noise or mooring noise may be present, and at high frequencies (> 10 kHz) where tidally driven sediment transport may generate noise. Residual dB, $dB_r(\omega, t)$ in Eq. 26, show periodic variations on tidal timescales persisting across a broad spectrum of acoustic frequencies, persisting in some cases up to 20 kHz, (Figure 23), and through most of the training data set (Figure 22). Harmonic regression at the critical frequencies identified in table 3 has two R^2 maxima of 0.21 and 0.19 at 100 Hz and 4.9 kHz respectively (Figure 24A). RMS dB residuals showed a similar trend with frequency where the largest deceases were seen at frequencies below

15 kHz (Figure 24B). Periodic variations in model residual are removed across the full frequency spectrum when the harmonic regression is used as a scaling factor (Figure 25).

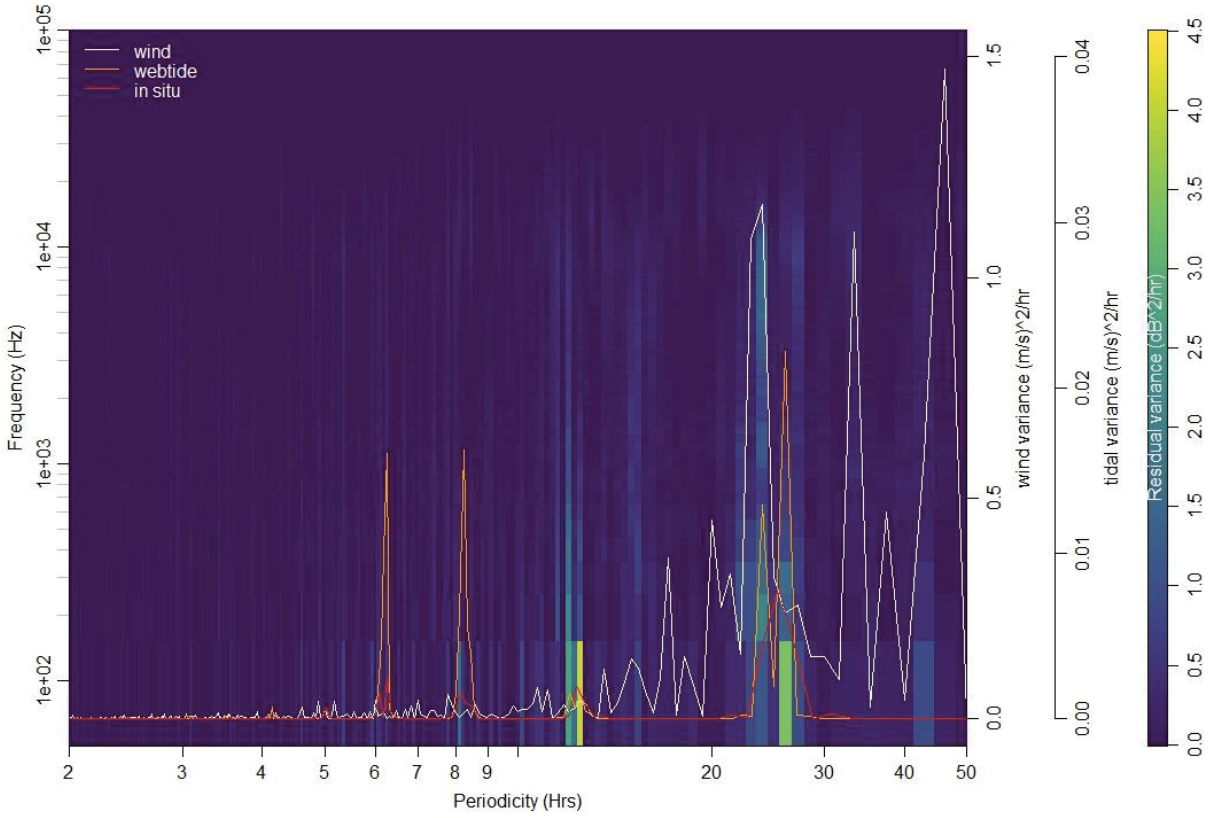

Figure 23: Periodospectrogram demonstrating the strength of wind, rain residual periodicity by frequency, prior to performing harmonic regression. Overlay is the periodicity present in the wind, in-situ current, and WebTide modelled velocity series.

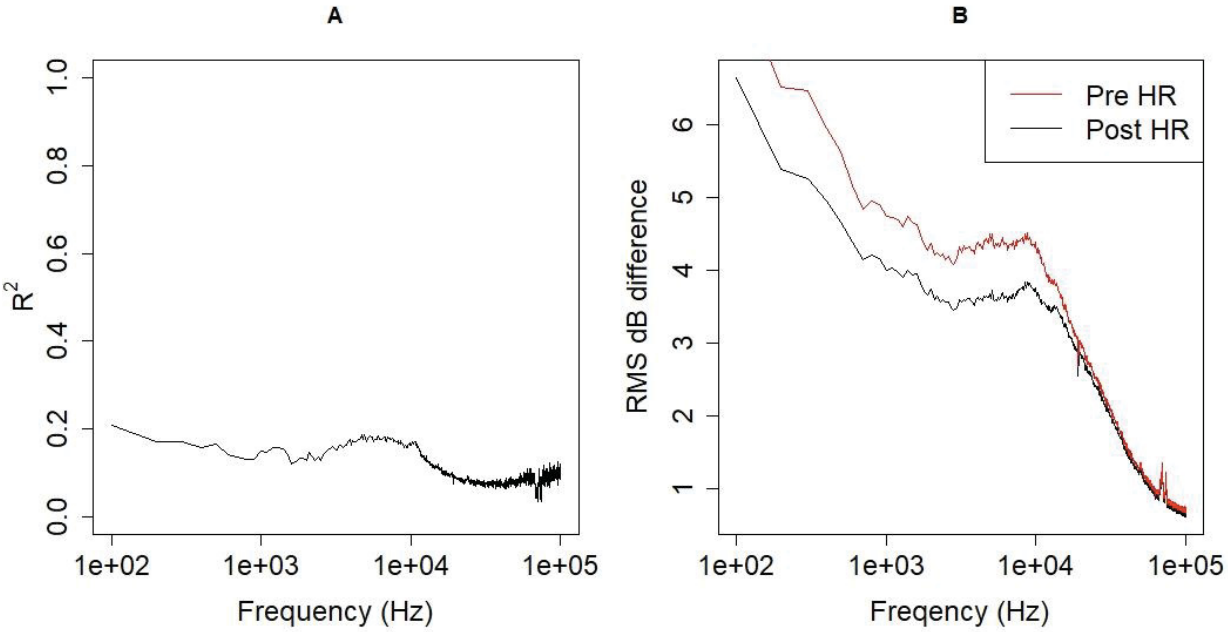

Figure 24: A) Spectra of coefficient of determination (R2) of harmonic regression at tidal frequencies identified in table 3. B) Spectra of total model dB difference after before and after applying the scaling factor generated by the harmonic regression.

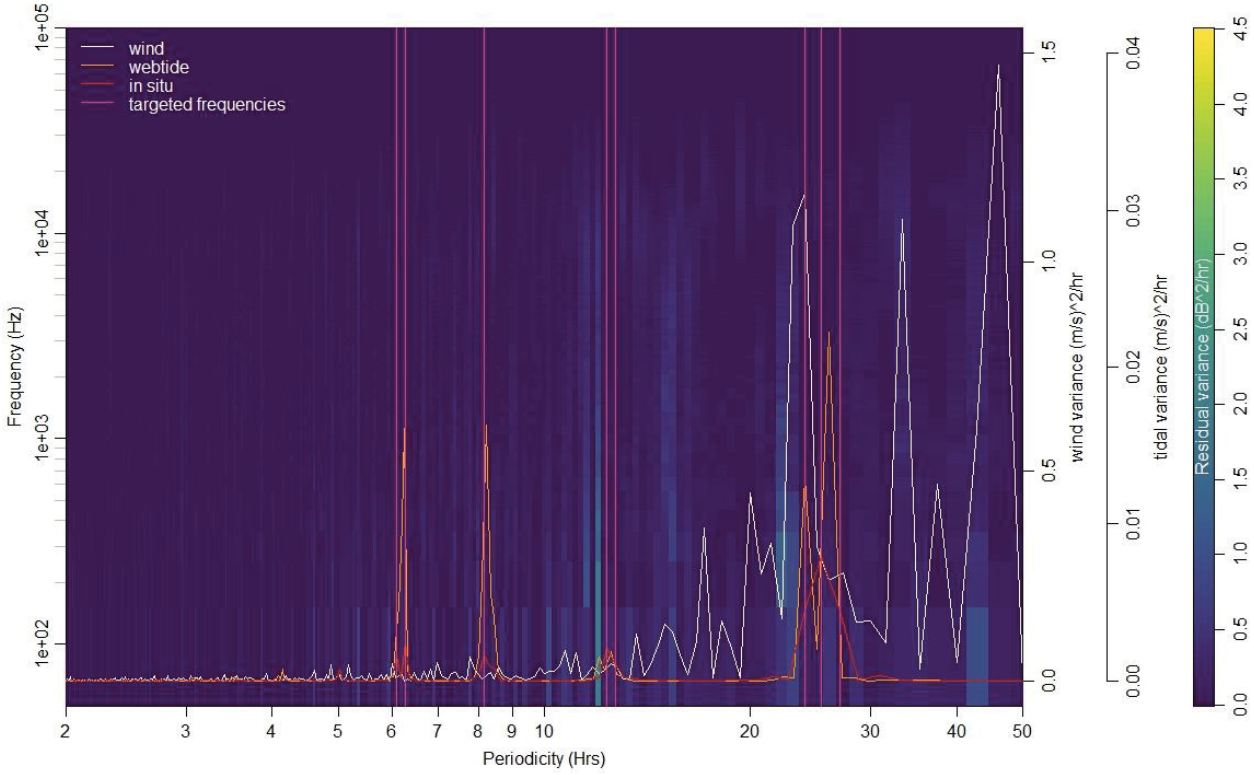

Figure 25: Periodospectrogram demonstrating the removal of wind and rain residual periodicity by frequency, after scaling by harmonic regression. Overlay is the periodicity present in the wind, in-situ current, and WebTide modelled velocity series, and critical frequencies used in the harmonic regression.

As the harmonic portion of the model takes the form of Eq. 32 and was fit on $dB_r(\omega, t)$, it must be transformed into linear space prior to inclusion in the full ambient noise field model. Consider that the residuals feeding the harmonic regression are calculated by Eq. 26. When combined with Eq. 26 and transformed to acoustic power ($\mu Pa^2 Hz^{-1}$), Eq. 30 becomes

$$\sum_{i=1}^{6} C_i sin(\omega_i t + \varphi_i) = 10log_{10}\left(\frac{\overline{\mathrm{X}}}{\widehat{W^2} + \widehat{R^2}}\right), \qquad Eq. 39$$

$$\overline{\mathrm{X}} = 10^{\frac{\sum_{i=1}^{6} C_i sin(\omega_i t + \varphi_i)}{10}} \times \left(\widehat{W^2} + \widehat{R^2}\right). \qquad Eq. 40$$

4.4 The cumulative model

Following the common regression model described in section 2.4 it is now possible to combine each of the environmental models together to predict the ambient noise field. Eq. 12 can be expanded to include the wind, rain, and tidal models in raw acoustic power ($\mu Pa^2 Hz^{-1}$) yielding:

$$\overline{\mathrm{X}}(\omega) = \beta \times \left(\begin{cases} 10^{\frac{Au^2+Bu+K}{10}} + \alpha \left(\frac{\xi}{u}\right)^G, & u > 5 \\ 10^{\frac{Mu+D}{10}} + \alpha \left(\frac{\xi}{u}\right)^G, & u \leq 5 \end{cases} \right), \qquad Eq. 41$$

$$\beta = 10^{\frac{\sum_{i=1}^{6} C_i sin(\omega_i t + \varphi_i)}{10}},$$

$$\alpha = 10^{\frac{H}{10}},$$

where $\overline{\mathrm{X}}$ is in $\mu Pa^2 Hz^{-1}$, $A,\ B,\ K,\ M,\ D,\ G,\ C,\ \varphi,\ H$ are all frequency dependent coefficients, u is U_{10} wind speed (m/s), and ω_i are the critical tidal frequencies for harmonic regression. Example coefficients for pre fit terms for at a variety of frequencies are provided in table 4.

Table 4: Example pre fit coefficients for model, including significance terms. Tides were not included as they were fit a posteriori. Harmonic frequencies are available in table 3.

	Coefficient													
	K		B		A		G		H		M		D	
Freq (kHz)	Fit	P-Val	Fit	P-Val	Fit	P-Val	Fit	P-Val	Fit	P-Val	Fit	P-Val	Fit	P-Val
3	60.06	8.06E-130	0.93	2.60E-04	-0.01	2.10E-01	-0.23	1.40E-01	77.22	4.77E-17	2.07	NA	64.47	NA
8	41.78	1.21E-79	2.23	5.29E-13	-0.05	5.34E-05	-0.24	2.21E-01	70.77	3.03E-14	1.04	NA	64.07	NA
10	37.88	3.41E-67	2.35	5.45E-13	-0.06	4.36E-05	0.02	9.33E-01	75.02	1.41E-13	0.68	NA	66.89	NA
20	33.04	1.91E-61	2.30	8.42E-14	-0.06	2.24E-05	-0.05	8.64E-01	70.25	1.93E-12	1.82	NA	62.54	NA
50	35.77	3.99E-142	0.78	1.30E-08	-0.01	2.56E-02	-0.06	7.75E-01	61.50	5.93E-13	0.79	NA	54.15	NA

The model performs well capturing wind events like those on April 21st or May 6th, 2018 (Figure 26). At frequencies above 10 kHz, rain events are present in both the observed and modelled spectrogram on April 20th, 28th, and between May 9th and 10th. The dynamic range of the model is also well represented with power falling towards the noise floor at higher frequencies. Structure below 10 kHz is less well characterized given the semi random broadband errors observable in the $\Delta(\omega, t)$ spectrogram, both positive and negative in equal measure, with $\Delta_{RMS}(\omega)$ of 2.88 at 20 kHz.

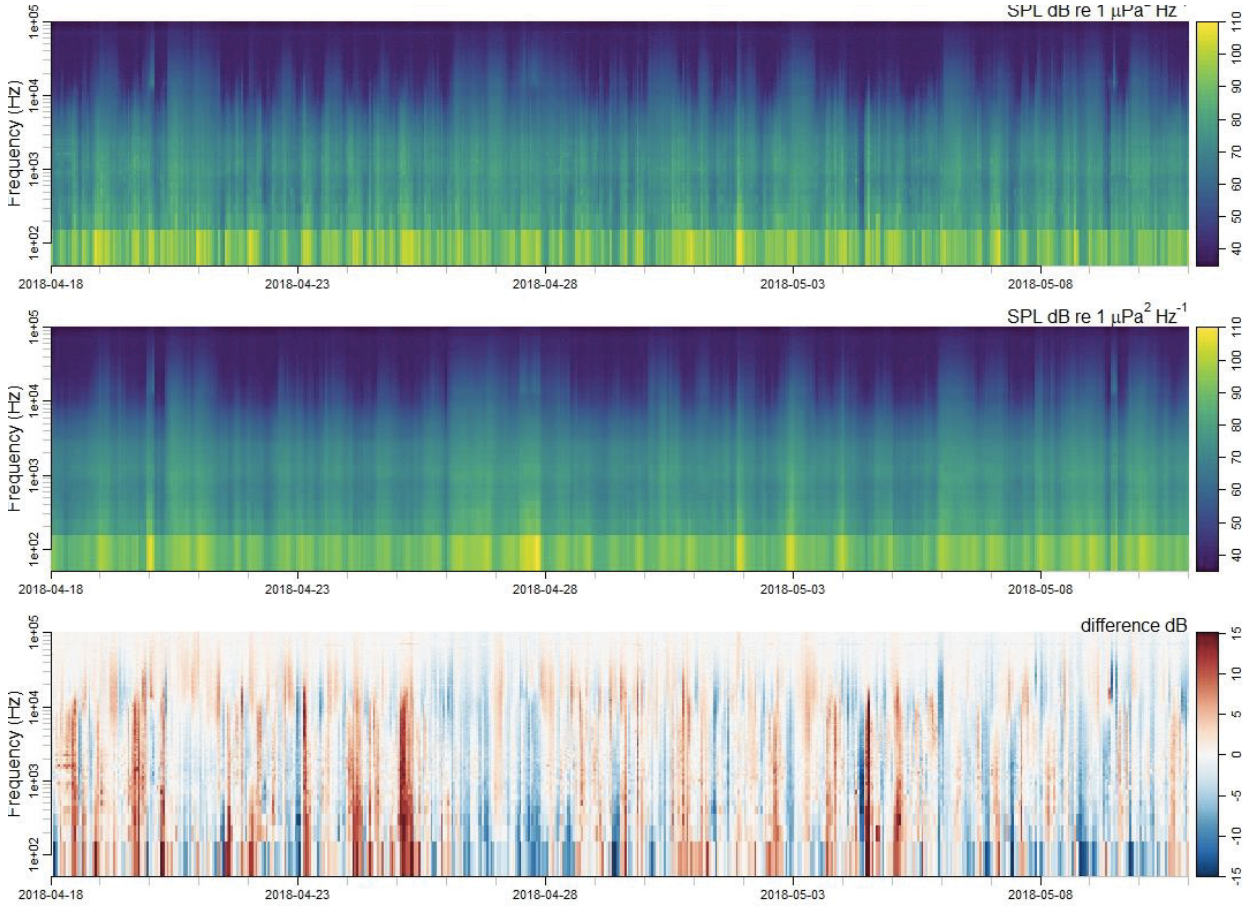

Figure 26: Top) Received level spectrogram used in the training dataset from April 18th to May 11th. Middle) Spectrogram predicted by Eq. 34 over the same time period. Bottom) Spectrogram of the difference in dB between the observed and predicted spectrograms. Red represents positive residuals (model underestimation) while blue represent negative residuals (model overestimation).

4.5 Source level estimation

Source level was calculated from predicted received level at six wind speeds and across 5 example frequencies (Figure 27 A) demonstrating model wind and frequency response. Figure 27 B shows the effect of NTL scaling of received level to source per unit area. The reduction in spectral slope highlights the increased transmission loss at high frequencies.

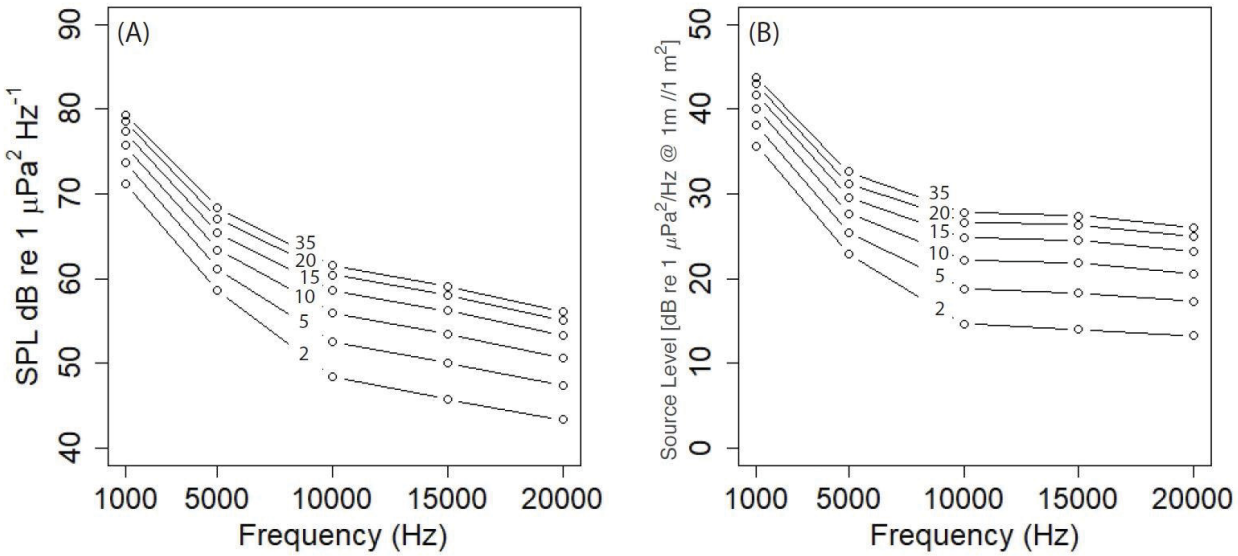

Figure 27 A) Modelled received levels at wind speeds of 2, 5, 10, 15, 20, 35 knots (1, 2.6, 5.1, 7.7 10.3, and 18 m/s) demonstrating wind speed frequency response of the model and B) Source strength per unit area computed from Eq. 18 from the modelled receive values shown in A.

4.6 Quality of fit through time

The cumulative model formation described in Section 4.4 was applied to time series of environmental parameters, with *a posteriori* harmonic regression for tidal periodicity, and compared to acoustic recordings between April 18th 2018 and February 27th 2019. Model-data comparison is quantified with monthly $\Delta_{RMS}(\omega)$ spectrogram (Figure 28), representing the RMS scale difference between the observed and modelled spectrogram. Complete monthly model-data comparisons are from April 2018 to February 2019 are shown in Appendix 2. Separation in time

between the training data set (April 18th to May 12th 2018) and the testing month generally increased Δ_{RMS} at frequencies up to 1 kHz, save February 2019. Δ_{RMS} at mid-frequencies (1 kHz to 10 kHz) are relatively consistent at between 3 and 5 dB save for a temporary increase to 5.2 dB between November 2018 and January 2019. At high frequencies between 50 and 100 kHz, Δ_{RMS} is relatively consistent at 1.3 dB. The narrowband deviation present at 50 kHz in September and October is visible in their respective spectrograms (A2 Figs 4 and 5).

The 3 dB residual contour in the monthly Δ_{RMS} spectrogram (Figure 28) represents the model achieving better than a factor of two fit with the observed spectrogram and is present between 10 and 50 kHz. The contour appears to show seasonality, with the largest band of the spectrum being adequately characterized by the model in May 2018, showing a 3 dB crossing frequency of 15.3 kHz. The month with the smallest band of the spectrum adequately characterized by the model was January 2019, with a 3 dB crossing frequency of 39.3 kHz. February 2019 showed a reversal of trend, with a greater portion of the spectra characterized by the model than January, with a 3 dB crossing frequency of 27.8 kHz. The average 3 dB crossing frequency was 29.2 kHz. A large portion of the model was characterized below the 6 dB threshold, representing a factor of four fit, with an average crossing frequency of 220 Hz, and showed no signs of seasonal effects. Qualitatively, there appears to be a plateau in RMS dB difference values between 10 and 20 kHz, similar to that present in the RMS dB difference observed in the training dataset (Figure 24 B).

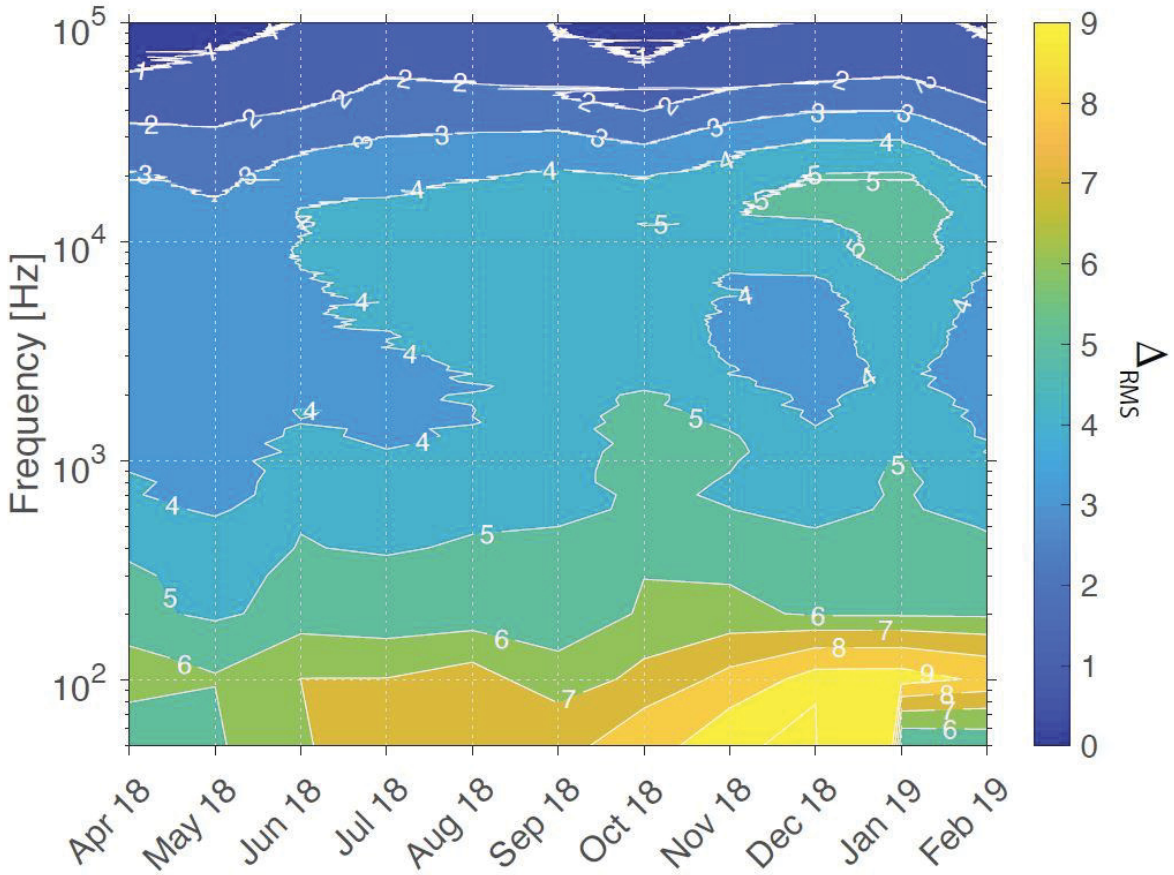

Figure 28: RMS dB difference by frequency for each month between April 2018 and February 2019. March wav files were omitted due to insufficient calibration resources. The white line represents the 3 dB contour, below which the model achieves a fit within a factor of 2. The red line represents the 6 dB contour and a fit within a factor of 4.

April (Figure 29) and May (Figure 30) 2018 show good agreement between the observed and modelled spectrogram. Medium and large-scale wind events are resolved throughout the frequency range, while rain events are well resolved above 10 kHz. April has minor periodicity on tidal timescales, while May shows increased tidal activity. Structure below 10 kHz is present, however the dynamic range of the model at these lower frequencies is less than the recorded spectrogram. The model accurately quantifies the appearance of the noise floor above 10 kHz as indicated by the dB difference trending towards zero.

Spectrograms from June (A2 Figure 1), July (A2 Figure 2), and August (A2 Figure 3) 2018, show substantial periodic variations on tidal timescales, including the strong presence of a spring-neap cycle with signatures extending across the full frequency spectrum. Characterization of the noise floor above 10 kHz is adequate in June, however the presence of strong tidal signals above 10 kHz in July and August reduce the predictive ability of the model. Structure of wind and rain events are again discernable, but to a lesser extent than in the preceding months, a corollary to the increasing RMS dB difference seen in Figure 24. Tidal signals are accounted for; however, the model is underestimating the dynamic range of their effects as demonstrated by the more consistent pattern in dB difference spectrums (A2 Figure 2, 3). All modeled spectrograms continue to deviate from their respective observed monthly spectrograms.

Spectrograms from September (A2 Figure 4), October (A2 Figure 5) and November (A2 Figure 6) continue to show periodic variations on tidal frequencies. In September, there are few resolvable wind events both in the observed and modelled series. Rain events, while present, are poorly characterized in September, with the model over and under estimating sound levels in equal measure. Anomalies present at 52 kHz account for the high frequency structure visible September and October in Figure 24. October shows improved agreement both in structure below 10 kHz, and the characterization of the noise floor above. However, the single rain event on October 6th is poorly represented as demonstrated in the dB difference spectrogram. November again shows the clear presence of a strong spring-neap cycle.

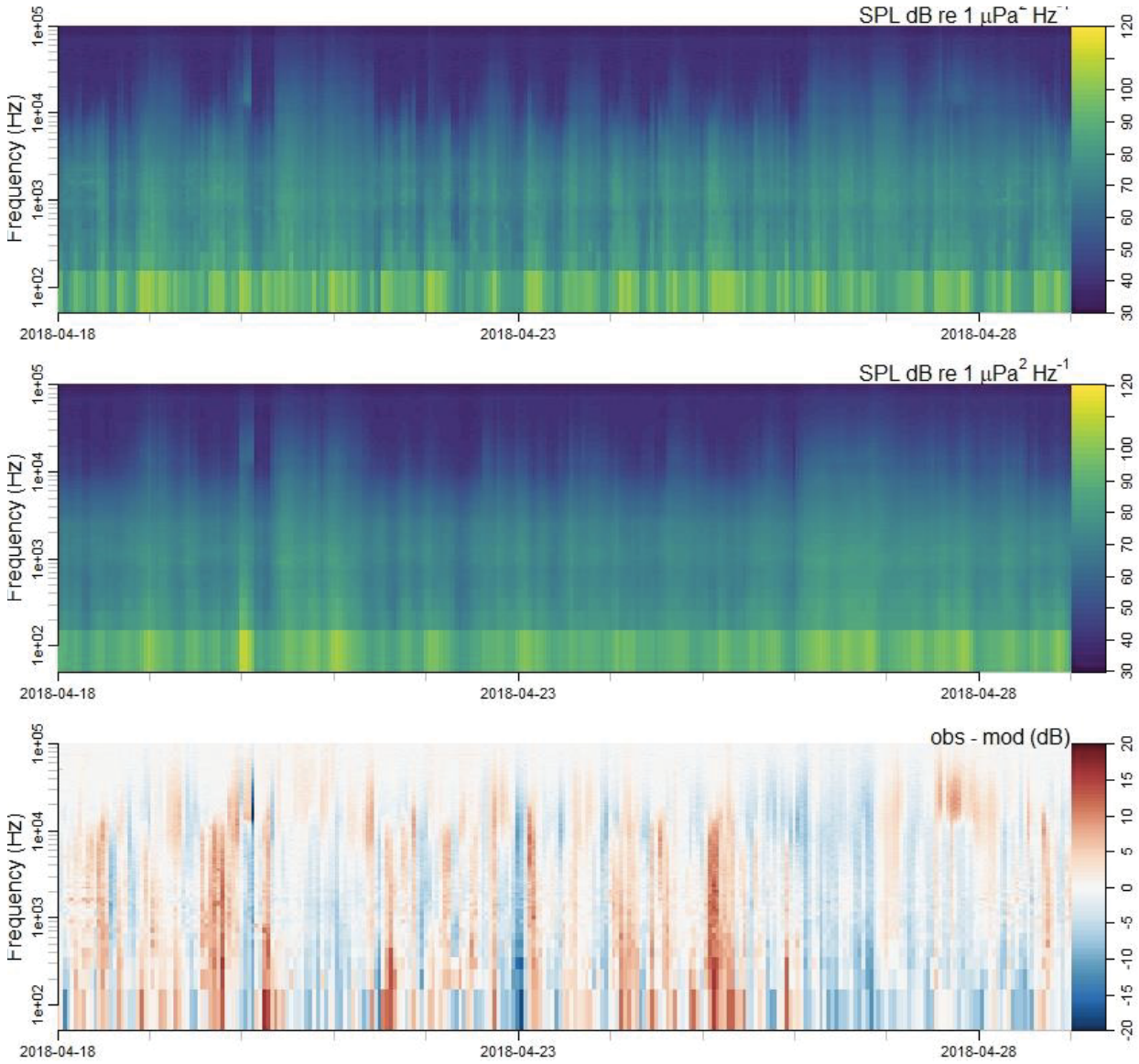

Figure 29: Comparative Spectrograms. Top) Received level spectrogram from April 18th to April 30th, 2018. Middle) Spectrogram predicted by Eq. 36 over the same time period. Bottom) Spectrogram of the difference in dB between the observed and predicted spectrograms. Red represents positive residuals (model underestimation) while blue represent negative residuals (model overestimation).

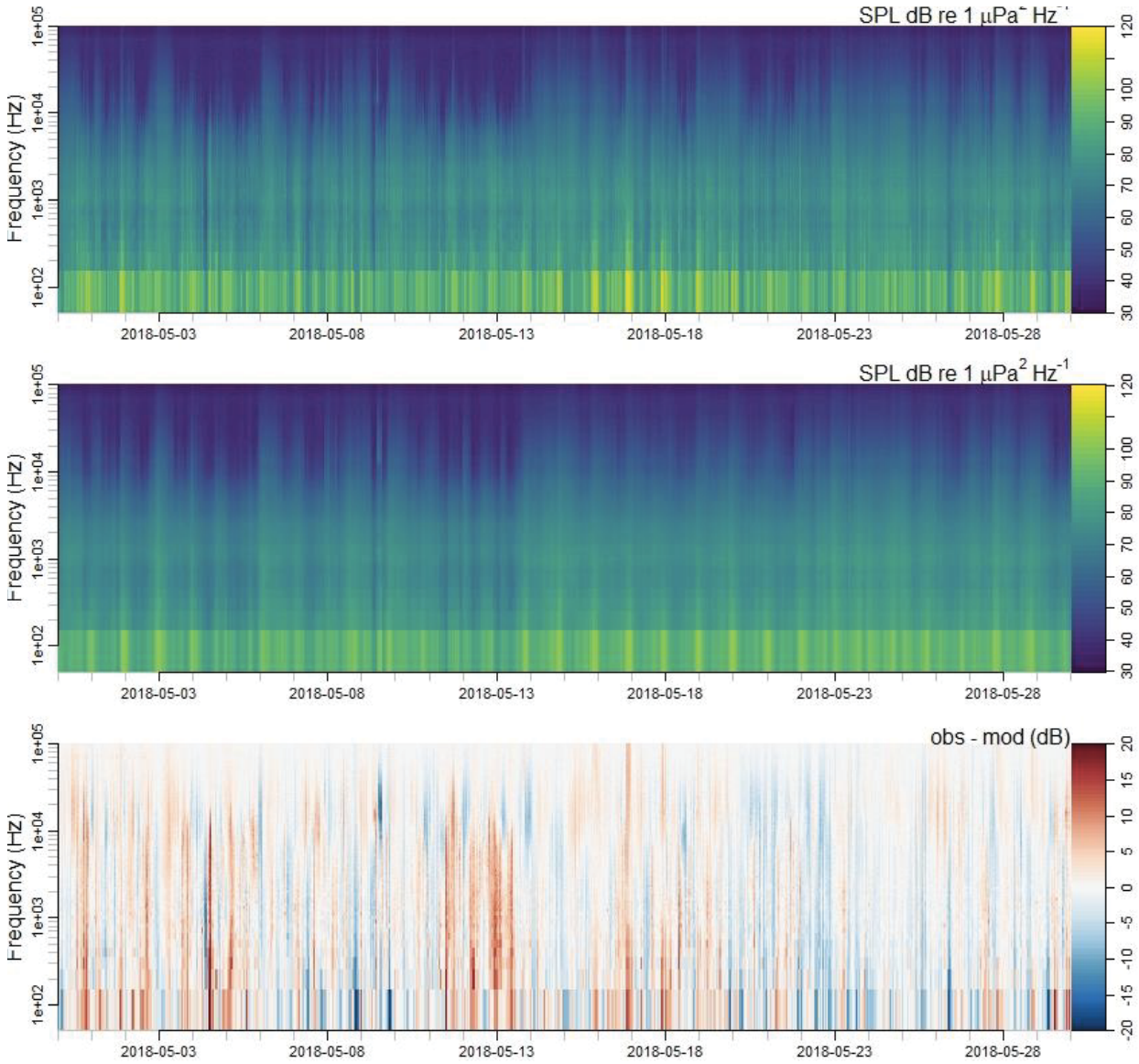

Figure 30: Comparative Spectrograms. Top) Received level spectrogram from May 2018. Middle) Spectrogram predicted by Eq. 36 over the same time period. Bottom) Spectrogram of the difference in dB between the observed and predicted spectrograms. Red represents positive residuals (model underestimation) while blue represent negative residuals (model overestimation).

Spectrograms of December 2018 (A2 Figure 7), January (A2 Figure 8), and February (A2 Figure 9) all show strong signs of a spring neap cycle at lower frequencies. In November, the model accurately targets the presence of wind events in time and frequency but underestimates

their contribution to the noise field by 5 - 7 dB. The model only shows good agreement with January 2019 in on the largest of wind structures above 39 kHz. Rain contribution is over predicted as seen in the precipitation event early in the month, and may be attributable to snowfall. February 2019 shows improved agreement with the model, with adequately resolved wind events and structure below 10 kHz. Rain events, though few, are adequately characterized and visible towards the beginning of the month. Residual dB for February shows a slowly oscillating trend on the order of 3 weeks.

5 Discussion

The Strait of Juan de Fuca, the surrounding Salish Sea, and Gulf Islands represent a highly diverse acoustic environment, with a variety of environmental, biogenic, and anthropogenic sources contained within a complex propagation environment (Eng\aas et al. 1996; Lusseau et al. 2009; Olszewski and Ren 2015). The goal of this project was to model the ambient soundscape baseline via in-situ acoustic recording and empirical regression against time series of environmental forcing agents, such as U_{10} (m/s) and rain rate (mm/hr). The model was parameterized on a subset of the data collected at Station S between April 18th and May 12th 2018, and then evaluated on acoustic recordings from Station S between April 18th 2018 and February 27th 2019. The following sections discuss model performance in both training and testing its predictive ability (5.1), sources of error from both the environment and assumptions in the model (5.2), comparisons with other source level models (5.3), and future recommendations on the next generation of ambient soundscape modelling (5.4).

5.1 Model performance

As the ambient sound scape in the region is created by a diverse array of sources, prefiltering of the data was required to isolate the signal of interest using with two filtering steps sequentially. Hourly minimum decimation outperformed mean and maximum decimation because the ambient background level, when all else is removed, is best characterized by the minimum sound level (Figure 17). Conversely, hourly maximum decimation selected for high intensity transients related to shipping or mooring noise and so does not make up the background ambient noise level; it was ultimately included out of completeness. Standard decimation to the hourly mean was also outperformed by the hourly minimum filter as it included the high intensity transients in its calculation.

While defining the natural ambient soundscape at all frequencies as the hourly minimum received sound level is possible as is demonstrated herein, it is likely that with a more nuanced approach such as frequency-dependent hourly percentiles, hourly decimation could yield better results. Hourly minimum decimation is highly dependent on the noise floor of the system being used, as it will always identify the noise floor if it is present within an hour. Given that spectral levels typically diminish with frequency, the noise floor becomes more prevalent (Figure 26), reduces the dynamic range of the predicted variable, and may account for the presence of two wind regimes in the training set. Furthermore, as the noise floor is present in the training dataset upon which the model is based, comparisons to systems with different noise floors will result in a perceived dynamic range error, as that is a strong feature identified by the model in the training dataset.

Spectral component filtering was used to identify the source characteristics of the hourly minimums and showed when they were attributable to a particular source, providing a cleaner training dataset for their respective environmental source regressions. 8 kHz and 20 kHz were used in this study following the example set by (Nystuen et al. 2010). These frequencies, while capable of resolving the general differences between wind, rain, and shipping sources, are likely not the optimal frequencies for resolving all sources. If the spectral effect of the source is not contained within the bands between 8 kHz and 20 kHz, then it cannot be resolved. As such the identification capability of the spectral component method is highly dependent on the frequencies chosen. Bandwidth of the 8 kHz and 20 kHz bins would also have an effect on resolving capacity.

The environmental fitting process provided an opportunity to evaluate the soundscape and its environmental contributors at Station S and compare it to generally accepted ocean sound

levels like the Wenz Spectrum (Wenz 1962). The Wenz spectrum predicts that the ambient noise field in the deep ocean will become sea state dominant above approximately 1 kHz without heavy surface traffic, with the frequency increasing as traffic increases. The wind driven R^2 spectra begins to show strong wind dependance above 2.5 kHz, with an R^2 increasing to 0.58, which is in relatively close agreement with accepted values considering the heavy commercial traffic present in the Salish Sea. The rain terms show generally lower R^2 for two reasons, they were fit on the remaining portion of the unexplained variation, and fewer number of rain events resulting in a larger spread of data.

While wind and rain may be corelated as environmental forcing agents as apparent in the effect of wind on raindrop grazing angle, their sound signatures are not, as the mechanism for noise generation are different. Wind can generate noise via breaking waves, as accounted for in section 3.42, while rain scaled by wind can only make noise if it is actively precipitating. Thus, scaling the precipitation rate rain by the wind is acceptable because it is still the rain that is wholly making the sound, while the wind is moderating the mechanics of the creation through its impact on grazing angle.

The *a posteriori* application of tidal regression is not truly *predictive* modelling, however the author felt it was justified given that the mechanics of the tidally mediated system are unknown in that it may be a source, modulation, or transmission loss term, or some combination thereof, suggesting that the phase could vary month to month, artificially inducing higher residuals. Thus, to assess predictive performance in light of this variation, its removal was deemed necessary. Further ambient noise modelling efforts should make the tidal component and its effect on the sound an area of primary investigation.

The criterion for success for this environmental ambient noise level model is the achievement of a $\Delta_{RMS}(\omega)$ better than 3 dB, representing a better than factor of two agreement with the observed noise levels. By such criterion, higher frequencies (> 25 kHz) were well characterized by the model, while lower frequencies (< 25 kHz) were less well characterized with a $\Delta_{RMS}(\omega)$ between 3.25 and 6. This is likely due in part to the presence of contamination by distant shipping sources (Kuperman and Ferla 1985; Nystuen et al. 2010) in a constrained environment at lower frequencies. A significant removal of contaminated sources reduced the number of training records from 6993 to 350, producing a model trained, ideally, against only meteorologically driven noise. In the Salish Sea however, it is rare to have ambient sound free of ship generate noise which reduces the performance of a model that has no ship noise component. The addition of such a component driven by Automated Identification System (AIS) data is another avenue for future research.

$\Delta_{RMS}(\omega)$ generally shows a decreasing trend with increased frequency in Figure 28. Practically speaking, this is due to the lower dynamic range found in the spectra at higher frequencies and is driven by the fact that $\Delta_{RMS}(\omega)$ is proportional to the total variation at frequency (ω). Thus, as the dynamic range in spectral levels decrease with frequency, so too does $\Delta_{RMS}(\omega)$. Frequency dependent transmission loss may also play a role in this trend. Higher frequencies are attenuated more readily from distant sources, and thus can be better characterized by local expressions of the environmental forcing terms used in the model. Conversely, lower frequencies resist attenuation and are therefore products of distant expressions not accounted for in the model. A secondary feature visible in most $\Delta_{RMS}(\omega)$ spectra (Figure 21, Figure 24, Figure 28) is the presence of plateau between 10 and 20 kHz, where it remains constant as frequency continues to decrease. This is likely attributable to the initial appearance of the noise floor in the

acoustic power series (Figure 19), and its change through time. This change may be due to the use of different recorders throughout the time period, or by a noise source in the environment that was not directly considered. Seasonality, while apparent in the 3 dB contour, cannot be concluded decisively because March is absent, and the dataset is not long enough to rule out stochastic variations. However, this preliminary indication of seasonality warrants further investigation into the seasonal variations of the ambient noise field in the Strait of Juan de Fuca and the Salish Sea.

5.2 Environmental and Assumptive Error

Taking a linear approach to fitting a combination of source terms to the acoustic model (Eq. 12), while simple, does have some drawbacks including the introduction of artificial residuals in the data due to potential correlation of higher order terms neglected in this analysis. The assumption that these sources are fully mechanically separable is likely not true, given the acoustic differences in rain accounted for by drop grazing angle under storm conditions, or that heavy rain can impact wave breaking characteristics (Ma and Nystuen 2005). Wind direction was not included in the model because the sample area was in a strait and it was assumed that in general there are only two reciprocal wind directions aligning within the straight, yielding consistent, relatively infinite fetch, as observed in a time series of wind direction (Figure 6).

A source of variation in the errors present is likely due to the assumed coupling between the soundscape at Station S and the source of the wind time series, Race Rocks light station. While relatively well co-located in the Strait of Juan de Fuca (Figure 1), the deployment location is located deeper into the strait while the light station is located at junction with the Salish sea, a comparatively more exposed region with greater fetch in multiple directions. It is likely that seasonal changes to the larger regional circulation patterns will change the relative coupling

between the two locations, ultimately accounting for part of the month-to-month differences in $\Delta_{RMS}(\omega)$ (Figure 28)

Furthermore the ability of the model to extrapolate noise levels at windspeed beyond the training set is poor, given the observed reduction in radiated sound during extreme wind events due to bubble mediated attenuation in the upper ocean (Farmer and Lemon 1984). The model was parameterized in early summer, it did not include the full range of wind speeds possible throughout the year, especially the extreme events possible in winter when bubble attenuation is observed. As such, there was no way for the model to predict the intense attenuation of wind generated sound at extreme wind speeds, likely resulting in over estimation of the soundscape. While modelling the minimum sound level does provided some room for error, it is likely not sufficient to fully account for these bubble mediated attenuation effects.

The time series of rain rate is also a potential source of environmental error in the model as it was created from the radar images, which can contain many different false return anomalies (ECCC). While significant effort to account for radar anomalies were made, through both spatial averaging and the hysteretic filtering algorithm, it is still likely that some were present in the time series. It has been presented that under certain conditions, ocean surface waves may generate false returns (ECCC). In this region, it is possible that these would show correlation with other forcing terms like wind speed or tidal induced wave breaking.

Tidal signals represent another source of environmental error, partially accounted for by harmonic regression. The mechanics of the tidally modulated sound level amplitude are difficult to fully disentangle and may range from source modulation through the proposed wind-wave tide mechanic of differential wave breaking under different current regimes, or it may be sediment transport and saltation noise. Tidal currents creating turbulence on bathymetric features and

altering the propagation environment may also be implicated. While performing a simple harmonic regression at know tidal frequencies is a first order approximation, improvements are expected if the mechanics can be better parameterized. Flow noise directly on the hydrophone occurs at lower frequencies (below 300 Hz in a tidal channel with flow speed ~ 2 m/s (Auvinen et al. 2019)) but may cause noise at higher frequencies due to motion of mooring components. However, because the harmonic regression shows best fit as a modulation term rather than a linear source term, it is likely that the tidal currents are modulating an existing noisescape in the Salish rather than adding to it.

Lastly, a source of error in the model-data comparisons is due to the total exclusion of vessel presence in the model. Since the waters near our receiver are so well travelled, persistent background noise due to ships is likely degrading model performance. The model, which seeks to only predict the natural components of the underwater soundscape, would require some additional noise element to capture the variable but relatively persistent ship noise contribution to the sound field in the region.

5.3 Comparison with previous studies

Previously, empirical ambient noise models have been developed and parameterized from acoustic recordings made in shallow and deep-water environments (Kuperman and Ferla 1985; Vagle et al. 1990; Ma and Nystuen 2005). In this study, rather than considering single environmental sources like wind, or rain, an effort is made to account for multiple sources making up the environmental ambient noise field in an acoustically complex environment like the near shore region. The wind parameterization utilized within this model took the form of a second order piecewise continuous relationship, with a wind speed breakpoint of 5 m/s (Eq. 35), with a second order term fit at higher windspeeds.

Kuperman and Ferla 1985 show a similar parametrization using second order polynomials to fit wind to sound level over a lower frequency band (50 Hz – 3.2 kHz) and noted that at wind speeds below 7 knots (3.6 m/s) had little effect on sound levels. It is likely that the higher critical frequency found in this study is a combination of increased surface traffic to major ports in the region, and the increased variability in noise levels at lower wind speeds.

Conversely, in a deep water study carried out by Vagle (Vagle et al. 1990), a linear fit between wind and sound levels was used, noting that higher order polynomials are less likely to be predicted by simple physical models in comparison to power laws, and that a marginal improvement in fit at high wind speeds did not warrant extra complexity. More complex formulations are available for rain formulations exist beyond this model, like that of Ma et al 2005, considering the spectral characteristics of different drop sizes, rain rate, and grazing angle, although they do recommend an exponential relationship for a first approximation (Nystuen et al. 2010). By fitting a model by frequency, and scaling rain rate by the wind speed, our simple model shows some agreement with their findings.

Kewley et al. (Kewley et al. 1990) made an estimate of the source level per unit area from an ensemble of results collected by other authors in deep and shallow water environments from many different regions, including Kuperman and Ferla's study site in the Mediterranean. All studies focused on frequencies below 3 kHz. The characteristic source level per unit area curves they produced are compared against our estimate of $10log_{10}\{Q_w^2\}$ at wind speeds of 10, 20, 30 and 40 knots, shown in Figure 31. For windspeeds above 20 knots, the source spectrum levels estimated in this thesis are underestimated relative to the historical data, suggesting that that $NTL(\omega)$, the modelled surface receive sensitivity integrated over the listening area of our sensor, may have been overestimated in the model domain. Small errors in transmission loss

may result in significant errors in estimating $NTL(\omega)$. Though sources at distant ranges undergo large transmission loss, the area over which they cover increase as r^2. Since $NTL(\omega)$ is the product of the transmission loss and the element of area $r\Delta r\Delta\theta$, distant sources (> 10 km) can still add significant energy to the noise field. The effect of persistent ship noise also plays a role in our results. For wind speeds below 10 knots, our source level is overestimated, likely due to the contamination of ship noise in our noise model training set.

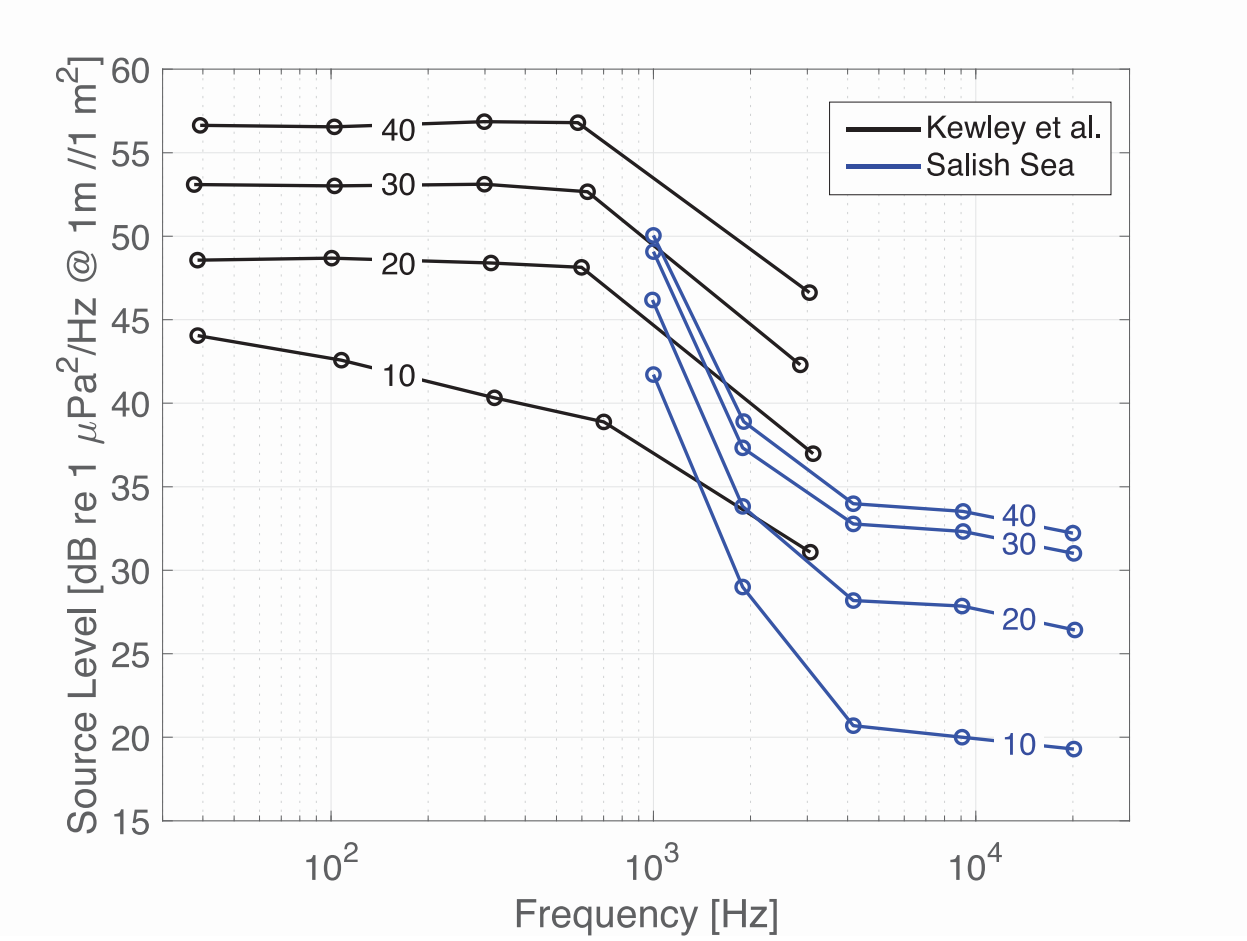

Figure 31: Source level spectrum computed by Kewley (black lines) and in this study (blue lines) for 10, 20, 30, and 40 knot wind speeds.

5.4 Future recommendations

Depending on the scale of the data set, fitting by frequency represents significant computation time and so it is recommended that method to collapse spectra about particular

indicator frequencies be implemented to speed up analysis, after which the spectra can be reconstructed. However, developing a frequency specific model allows for frequency specific sensitivity analysis, and may highlight seasonal effect in the model not previously considered, represented in Figure 27. The acoustic filtration process provided herein to better resolve the ambient soundscape at lower frequencies can likely also be further optimized. Rather than choosing a single metric, like the minimum, to represent the ambient soundscape at all frequencies, a frequency dependent descriptor, likely some form of percentile, may improve detection. Furthermore, rather than using two frequencies to classify sources in a spectral component plot, the use of more frequencies would improve the resolving capability of this system, behaving increasingly like a PCA grouping method. To begin determining the mechanics behind the impact of tides and currents on this system, it is recommended that wind and wave and current direction be included in future version of this model. Calculation of source strength per area of other existing source level models is recommended to improve model intercomparison.

6 Conclusions

This model was a parameterized with the express goal of modelling the baseline environmental soundscape in coastal waters in time, frequency, and space, based on available environmental parameters like wind speed, rain rate, and tidal currents. Acoustic parameterization data was collected in the Strait of Juan de Fuca, BC, between April 18th and May 12th, 2018, and tested against acoustic records from April 18th 2018 to February 27th 2019. In doing so, it was successfully demonstrated that:

1. The received soundscape, heavily contaminated by anthropogenic sources, can be successfully filtered by decimation to hourly minimum levels and spectral component analysis to isolate the for the environmental ambient soundscape.
2. The environmental ambient sound scape can be used to parameterize an environmental noise model, represented as a linear combination of wind, rain, and unknown source terms, modulated by tidal forcing. Model data comparison until February 27th showed good fit, <3dB $\Delta_{RMS}(\omega)$ at frequencies above 20 kHz, and <6dB $\Delta_{RMS}(\omega)$ at frequencies below 20 kHz.
3. The modelled soundscape can be made independent of model training location through calculation of the spectral source level based on calculations of local transmission loss, and that estimated spectral source level compare favorably with other estimates of Ma et al 2005, and Kuperman and Ferla 1980.

References

Abileah R, Lewis D. 1996 Sep 26. Monitoring high-seas fisheries with long-range passive acoustic sensors. IEEE Transactions on Audio and Electroacoustics.:378–382. doi:https://doi.org/10.1109/OCEANS.1996.572776.

Ainslie MA, Miksis-Olds JL, Martin B, Heaney K, de Jong CAF, von Brenda-Beckman AM, Lyonse AP. 2018. Underwater Soundscape and Modelling Metadata Standard Version 1.0. Atlantic Deepwater Ecosystem Observatory Network (ADEON):An Integrated System for Long-Term monitoring of Ecological and Human Factors on the Outer Continental Shelf Report No.: M16PC00003.

Alsarayreh T, Zedel L. 2011. Quantifying snowfall rates using underwater sound. Atmosphere-ocean. 49(2):61–66.

Arveson PT, Vendittis DJ. 2000. Radiated noise characteristics of a modern cargo ship. The Journal of the Acoustical Society of America. 107(1):118–129. doi:10.1121/1.428344.

Auvinen MF, Barclay DR, Coffin ME. 2019. Performance of a Passive Acoustic Linear Array in a Tidal Channel. IEEE Journal of Oceanic Engineering.

Barclay DR. 2011. Depth profiling ambient noise in the deep ocean [PhD Thesis]. UC San Diego.

Barclay DR, Bevans DA, Buckingham MJ. 2019. Estimation of the Geoacoustic Properties of the New England Mud Patch From the Vertical Coherence of the Ambient Noise in the Water Column. IEEE Journal of Oceanic Engineering. 45(1):51–59.

Barclay DR, Buckingham MJ. 2013. Depth dependence of wind-driven, broadband ambient noise in the Philippine Sea. The Journal of the Acoustical Society of America. 133(1):62–71.

Barclay DR, Lin Y-T. 2019. Three-dimensional ambient noise modeling in a submarine canyon. The Journal of the Acoustical Society of America. 146(3):1956–1967.

Bass SJ, Hay AE. 1997. Ambient noise in the natural surf zone: Wave-breaking frequencies. IEEE journal of oceanic engineering. 22(3):411–424.

Carey WM, Evans RB. 2011. Ocean ambient noise: measurement and theory. Springer Science & Business Media.

Chapman NR, Price A. 2011. Low frequency deep ocean ambient noise trend in the Northeast Pacific Ocean. The Journal of the Acoustical Society of America. 129(5):EL161–EL165.

Cron BF, Sherman CH. 1962. Spatial-Correlation Functions for Various Noise Models. The Journal of the Acoustical Society of America. 34(11):1732–1736.

Deane GB, Stokes MD. 2002. Scale dependence of bubble creation mechanisms in breaking waves. Nature. 418(6900):839–844. doi:10.1038/nature00967.

Deane GB, Stokes MD. 2010. Model calculations of the underwater noise of breaking waves and comparison with experiment. The Journal of the Acoustical Society of America. 127(6):3394–3410.

DFO. 2009. Webtide; Tidal Prediction Model. Fisheries and Oceans Canada Dartmouth, NS.

Dudzinski KM, Thomas JA, Gregg JD. 2009. Communication in Marine Mammals. In: Encyclopedia of Marine Mammals. 2nd ed. Academic Press. p. 260–269.

Eng\aas A, Løkkeborg S, Ona E, Soldal AV. 1996. Effects of seismic shooting on local abundance and catch rates of cod ((Gadus morhua) and haddock)(Melanogrammus aeglefinus). Canadian journal of fisheries and aquatic sciences. 53(10):2238–2249.

Farmer DM, Lemon DD. 1984. The influence of bubbles on ambient noise in the ocean at high wind speeds. Journal of Physical Oceanography. 14(11):1762–1778.

Farmer DM, Vagle S. 1988. On the determination of breaking surface wave distributions using ambient sound. J Geophys Res. 93(C4):3591. doi:10.1029/JC093iC04p03591.

Frisk GV. 2012. Noiseonomics: The relationship between ambient noise levels in the sea and global economic trends. Scientific reports. 2:437.

Hamilton JD. 2020. Time series analysis. Princeton university press.

Holt MM, Noren DP, Veirs V, Emmons CK, Veirs S. 2009. Speaking up: Killer whales (Orcinus orca) increase their call amplitude in response to vessel noise. The Journal of the Acoustical Society of America. 125(1):EL27–EL32.

Ingenito F, Wolf SN. 1989. Site dependence of wind-dominated ambient noise in shallow water. The Journal of the Acoustical Society of America. 85(1):141–145.

Jensen FB, Kuperman WA, Porter MB, Schmidt H. 2011. Computational ocean acoustics. Springer Science & Business Media.

Katsnelson B, Godin O, Zhang Q. 2019. Variations of Acoustic Noise Intensity Accompanying Internal Wave Soliton. In: OCEANS 2019-Marseille. IEEE. p. 1–4.

Ketten DR, Lien J, Todd S. 1993. Blast injury in humpback whale ears: evidence and implications. The Journal of the Acoustical Society of America. 94(3):1849–1850.

Kewley DJ, Browning DG, Carey WM. 1990. Low-frequency wind-generated ambient noise source levels. The Journal of the Acoustical Society of America. 88(4):1894–1902.

Kundu PK, Cohen IM, Dowling D. 2008. Fluid Mechanics 4th. Elsevier.

Kuperman WA, Ferla MC. 1985. A shallow water experiment to determine the source spectrum level of wind-generated noise. The Journal of the Acoustical Society of America. 77(6):2067–2073.

Lee Z, Du K, Arnone R, Liew S, Penta B. 2005. Penetration of solar radiation in the upper ocean: A numerical model for oceanic and coastal waters. J Geophys Res. 110(C9):C09019. doi:10.1029/2004JC002780.

Lusseau D, Bain DE, Williams R, Smith JC. 2009. Vessel traffic disrupts the foraging behavior of southern resident killer whales Orcinus orca. Endangered Species Research. 6(3):211–221.

Ma BB, Nystuen JA. 2005. Passive Acoustic Detection and Measurement of Rainfall at Sea. JOURNAL OF ATMOSPHERIC AND OCEANIC TECHNOLOGY. 22:24.

Marques PAM, Araújo CBD. 2015. The Need to Document and Preserve Natural Soundscape Recordings as Acoustic Memories. doi:10.13140/RG.2.1.4396.9123. [accessed 2020 Jan 23]. http://rgdoi.net/10.13140/RG.2.1.4396.9123.

Martin B, Hillis C, Miksis-Olds J, Ainslie M, Warren J, Heaney KD. 2017. ADEON Hardware Specification.

McDonald MA, Hildebrand JA, Wiggins SM. 2006. Increases in deep ocean ambient noise in the Northeast Pacific west of San Nicolas Island, California. The Journal of the Acoustical Society of America. 120(2):711–718.

McDougall TJ, Barker PM. 2011. Getting started with TEOS-10 and the Gibbs Seawater (GSW) oceanographic toolbox. SCOR/IAPSO WG. 127:1–28.

Medwin H, Nystuen JA, Jacobus PW, Ostwald LH, Snyder DE. 1992. The anatomy of underwater rain noise. The Journal of the Acoustical Society of America. 92(3):1613–1623.

Miksis-Olds JL, Nichols SM. 2016. Is low frequency ocean sound increasing globally? The Journal of the Acoustical Society of America. 139(1):501–511.

Nystuen JA, Moore SE, Stabeno PJ. 2010. A sound budget for the southeastern Bering Sea: Measuring wind, rainfall, shipping, and other sources of underwater sound. The Journal of the Acoustical Society of America. 128(1):58–65. doi:10.1121/1.3436547.

Nystuen JA, Ostwald Jr LH, Medwin H. 1992. The hydroacoustics of a raindrop impact. The Journal of the Acoustical Society of America. 92(2):1017–1021.

Olszewski GC, Ren J. 2015. Development and policy analysis of an effective noise management strategy for port metro Vancouver. In: INTER-NOISE and NOISE-CON Congress and Conference Proceedings. Vol. 250. Institute of Noise Control Engineering. p. 938–947.

Pine MK, Nikolich K, Martin B, Morris C, Juanes F. 2020. Assessing auditory masking for management of underwater anthropogenic noise. The Journal of the Acoustical Society of America. 147(5):3408–3417.

Porter MB. 2001. The BELLHOP Manual and User's Guide: :57.

Putland RL, Merchant ND, Farcas A, Radford CA. 2018. Vessel noise cuts down communication space for vocalizing fish and marine mammals. Global change biology. 24(4):1708–1721.

Rolland RM, Parks SE, Hunt KE, Castellote M, Corkeron PJ, Nowacek DP, Wasser SK, Kraus SD. 2012. Evidence that ship noise increases stress in right whales. Proceedings of the Royal Society B: Biological Sciences. 279(1737):2363–2368.

Shajahan N, Barclay D. 2020. Remote sensing mixed layer depth using ocean ambient noise. In: EGU General Assembly Conference Abstracts. p. 9671.

Siderius M, Harrison CH, Porter MB. 2006. A passive fathometer technique for imaging seabed layering using ambient noise. The Journal of the Acoustical Society of America. 120(3):1315–1323.

Smith DA. 1998. A quantitative method for the detection of edges in noisy time–series. Philosophical Transactions of the Royal Society of London Series B: Biological Sciences. 353(1378):1969–1981.

Thomson DJ, Barclay DR. 2020. Real-time observations of the impact of COVID-19 on underwater noise. The Journal of the Acoustical Society of America. 147(5):3390–3396.

Thorp WH. 1967. Analytic description of the low-frequency attenuation coefficient. The Journal of the Acoustical Society of America. 42(1):270–270.

Urick R, Kuperman WA. 1989. Ambient noise in the sea. Acoustical Society of America.

Vagle S, Large WG, Farmer DM. 1990. An Evaluation of the WOTAN Technique of inferring Oceanic Winds from Underwater Ambeint Sound. JOURNAL OF ATMOSPHERIC AND OCEANIC TECHNOLOGY. 7:576–595.

Veirs S, Veirs V, Wood JD. 2016. Ship noise extends to frequencies used for echolocation by endangered killer whales. PeerJ. 4:e1657.

Welch P. 1967. The use of fast Fourier transform for the estimation of power spectra: A method based on time averaging over short, modified periodograms. IEEE Trans Audio Electroacoust. 15(2):70–73. doi:10.1109/TAU.1967.1161901.

Wenz GM. 1962. Acoustic Ambient Noise in the Ocean: Spectra and Sources. The Journal of the Acoustical Society of America. 34(12):1936–1956. doi:10.1121/1.1909155.

Wille PC, Geyer D. 1984. Measurements on the origin of the wind-dependent ambient noise variability in shallow water. The Journal of the Acoustical Society of America. 75(1):173–185.

Williams R, Erbe C, Ashe E, Beerman A, Smith J. 2014. Severity of killer whale behavioral responses to ship noise: a dose–response study. Marine pollution bulletin. 79(1–2):254–260.

Woolfe KF, Lani S, Sabra KG, Kuperman WA. 2015. Monitoring deep-ocean temperatures using acoustic ambient noise. Geophysical Research Letters. 42(8):2878–2884.

Appendix 1: Hydrophone deployment locations, durations, and notes

Location	Location coordinates	Water depth	Deployment Date	Retrieval Date	Comments
Haro Strait	48° 29.750'N 123° 11.567'W	235 m	Jan 31 2018	Apr 14 2018	
			Apr 14 2018	Jun 19 2018	
			Jun 19 2018	Aug 20 2018	
			Aug 20 2018	Oct 14 2018	
			Oct 14 2018	Nov 28 2018	
			Nov 28 2018	Mar 6 2019	Stopped recording Feb 27
			Mar 6 2019	May 31 2019	
			May 31 2019	Aug 18 2019	
			Aug 18 2019	Nov 24 2019	
			Nov 24 2019	July 16 2020	stopped recording Mar 21 2020
			July 16 2020		
Sooke	48° 17.365'N 123° 39.137'W	165 m	Feb 1 2018	Apr 15 2018	Stopped recording Feb 6 to Mar 6 2018
			Apr 15 2018	Jun 19 2018	
			Jun 19 2018	Aug 17 2018	
			Aug 17 2018	Oct 12 2018	
			Oct 12 2018	Nov 29 2018	
			Nov 29 2018	Mar 5 2019	Stopped recording Feb 27
			Mar 5 2019	May 31 2019	Stopped recording May 18
			May 31 2019	Aug 17 2019	Stopped recording Aug 9
			Aug 17 2019	Nov 25 2019	Stopped recording Nov 3
			Nov 25 2019	May 14 2020	stopped recording Feb 11
			May 14 2020	Sep 10 2020	
			Sep 10 2020		
Port Renfrew	48° 30.274'N 124° 31.016'W	170 m	Feb 1 2018	April 15 2018	
			Apr 16 2018	Jun 20 2018	
			Jun 20 2018	Aug 19 2018	stopped recording after 7 seconds
			Aug 19 2018	Oct 11 2018	
			Oct 11 2018	Nov 29 2018	
			Nov 29 2018	Mar 4 2019	Stopped recording Feb 28
			Mar 4 2019	May 30 2019	
			May 30 2019	Aug 16 2019	
			Aug 16 2019	Nov 26 2019	
			Nov 26 2019	June 21 2020	stopped recording March 24 2020
			June 21 2020	Sep 12 2020	
			Sep 12 2020		
Jordan River	48° 23.793'N 124° 07.976'W	120 m	Feb 1 2018	Apr 16 2018	
			Apr 16 2018	Jun 19 2018	

Location	Location coordinates	Water depth	Deployment Date	Retrieval Date	Comments
			Jun 20 2018	Aug 17 2018	
			Aug 17 2018	Oct 12 2018	
			Oct 12 2018	Nov 30 2018	
			Nov 30 2018	Mar 4 2019	
			Mar 4 2019	May 30 2019	
			May 30 2019	Aug 17 2019	
			Aug 17 2019	Nov 25 2019	
			Nov 25 2019	May 14 2020	stopped recording Mar 19
			May 14 2020	Sep 12 2020	
			Sep 12 2020		
Boundary Pass	48° 44.014'N 123° 08.741'W	180 m	Feb 5 2018	Apr 14 2018	
			Apr 14 2018	Jun 21 2018	
			Jun 21 2018	Aug 20 2018	
			Aug 20 2018	Oct 14 2018	
			Oct 14 2018	Nov 27 2018	
			Nov 27 2018	Mar 6 2019	stopped recording Feb 23
			Mar 6 2019	Jun 1 2019	
			Jun 1 2019	Aug 18 2019	stopped recording Jul 2
			Aug 18 2019	Nov 24 2019	stopped recording Nov 3
			Nov 24 2019	May 12 2020	stopped recording Feb 9
			May 12 2020	Sep 14 2020	
			Sep 14 2020		
Swiftsure MEQ	48° 30.924'N 124° 56.156'W	75 m	Jul 13 2017	Apr 15 2018	
			Apr 15 2018	Aug 16 2018	stopped recording Jul 29
			Aug 16 2018	Oct 11 2018	
			Oct 11 2018	Nov 30 2018	
			Nov 30 2018	Mar 3 2019	
			Mar 3 2019	May 30 2019	
			May 30 2019	Aug 15 2019	
			Aug 15 2019	Nov 26 2019	
			Nov 26 2019	Jun 21 2020	stopped recording Mar 18 2020
			Jun 21 2020	Sep 11 2020	
			Sep 11 2020		
Turn Point	48° 42.099'N 123° 16.654'W	195 m	June 1 2019	Aug 18 2019	
Swanson Channel	48° 44.340'N 123° 15.340'W	75 m	Aug 18 2019	Nov 23 2019	
			Nov 24 2019	May 12 2020	stopped recording Mar 20 2020
			May 12 2020	Sep 14 2020	
			Sep 14 2020		
Swiftsure ISZ		40 m	Feb 7 2020	Jun 21 2020	stopped recording Jun 17

Location	Location coordinates	Water depth	Deployment Date	Retrieval Date	Comments
	48° 33.120'N 125° 00.432'W		Jun 21 2020 Sep 11 2020	Sep 11 2020	
East Point	48° 46.566'N 123° 04.156'W	85 m	May 12 2020 Sep 14 2020	Sep 14 2020	
La Perouse Bank	48° 23.085'N 125° 48.326'W	150 m	May 31 2019 June 23 2020	June 23 2020	stopped recording Jun 15 2019
Strait of Georgia South	48° 58.862'N 123° 24.303'W	240 m	Aug 9 2020		
Strait of Georgia North	49° 11.568'N 123° 20.788'W	190 m	Aug 9 2020		

Appendix 2: Comparison between recorded and predicted hourly minimum spectrograms

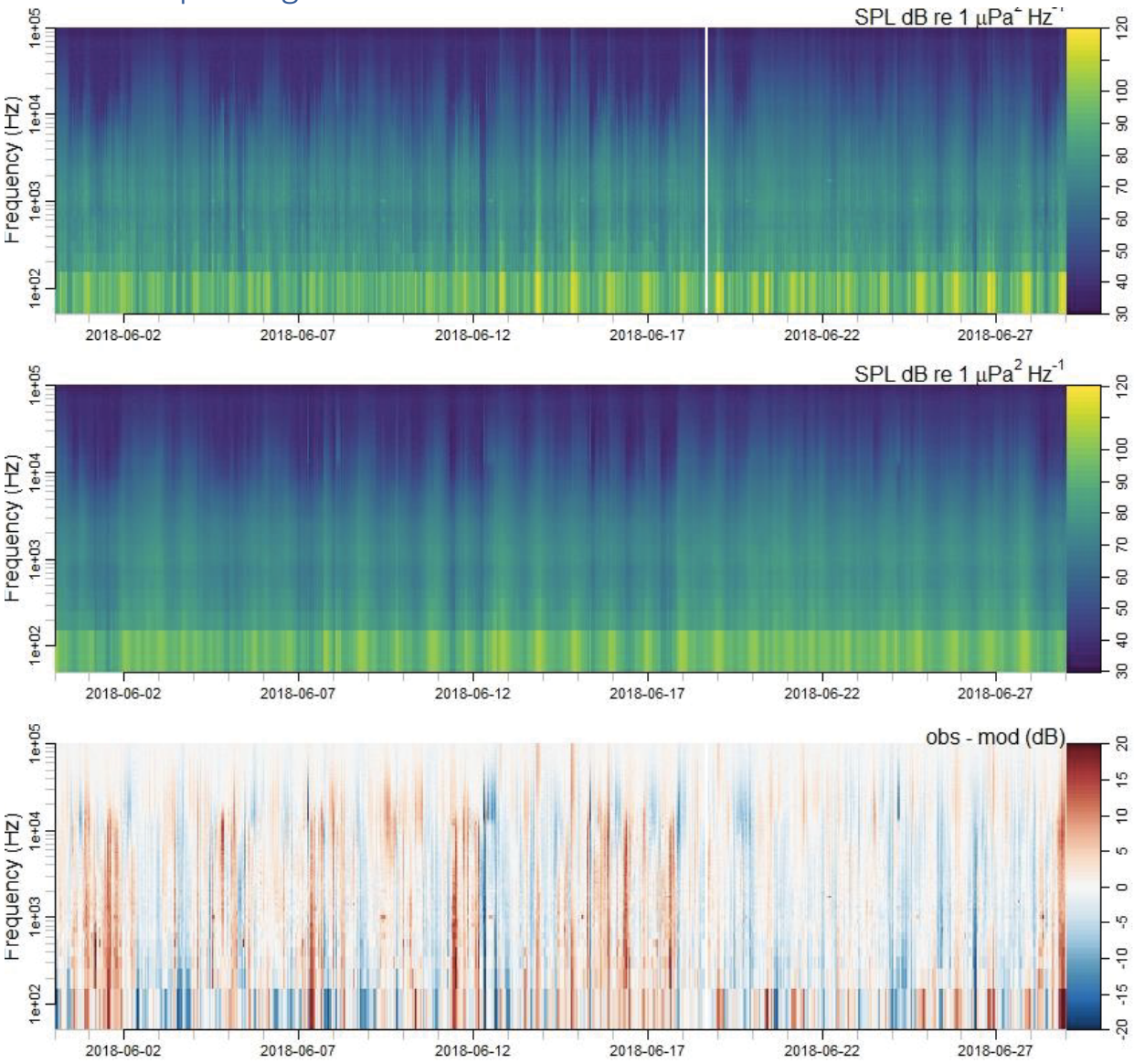

A2 Figure 1: Comparative Spectrograms. Top) Received level spectrogram from June 2018. Missing data on the 18th are due to the mooring being removed for servicing. Middle) Spectrogram predicted by Eq. 34 over the same time period. Bottom) Spectrogram of the difference in dB between the observed and predicted spectrograms. Red represents positive residuals (model underestimation) while blue represent negative residuals (model overestimation).

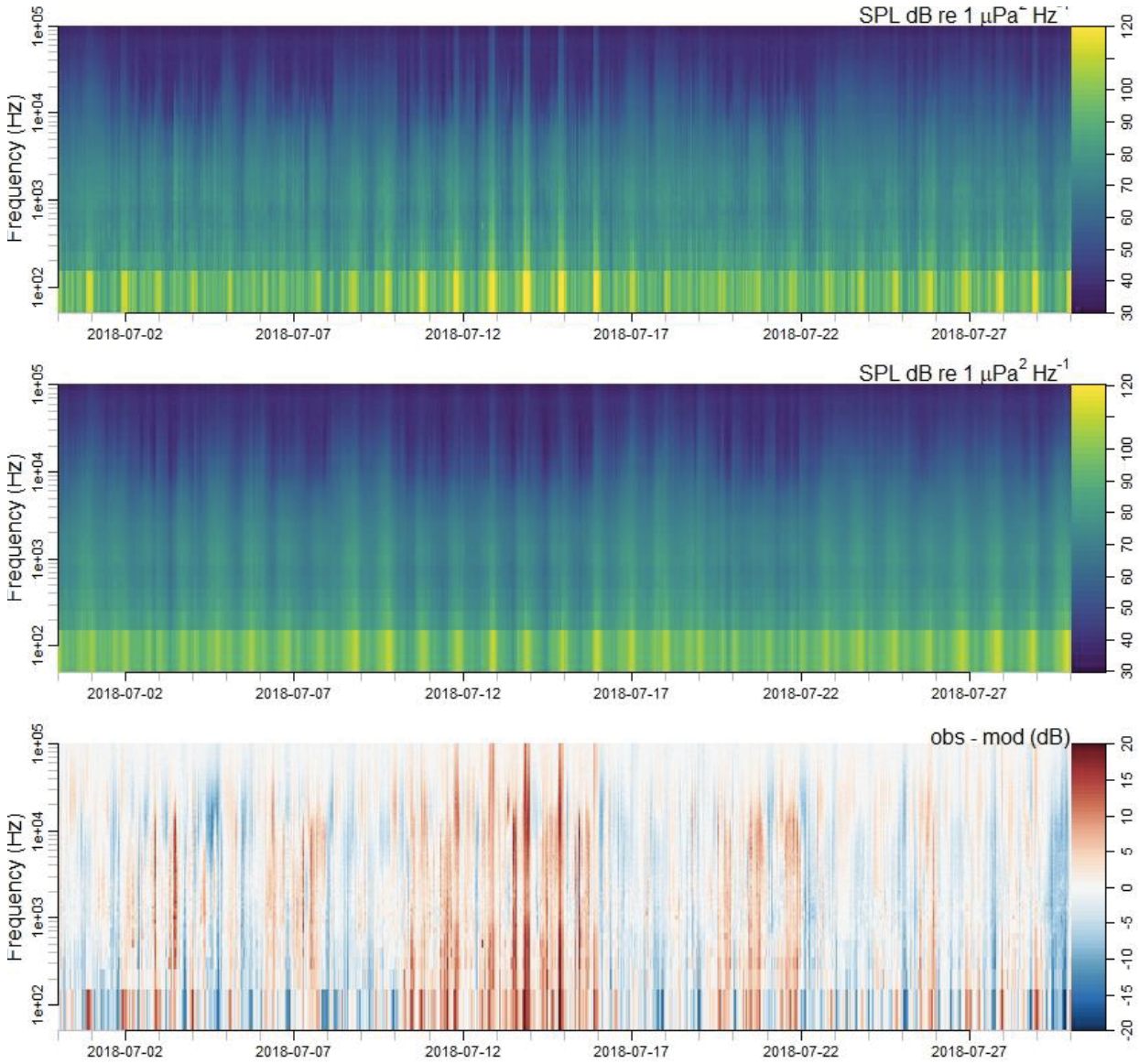

A2 Figure 2: Comparative Spectrograms. Top) Received level spectrogram from July 2018. Middle) Spectrogram predicted by Eq. 34 over the same time period. Bottom) Spectrogram of the difference in dB between the observed and predicted spectrograms. Red represents positive residuals (model underestimation) while blue represent negative residuals (model overestimation).

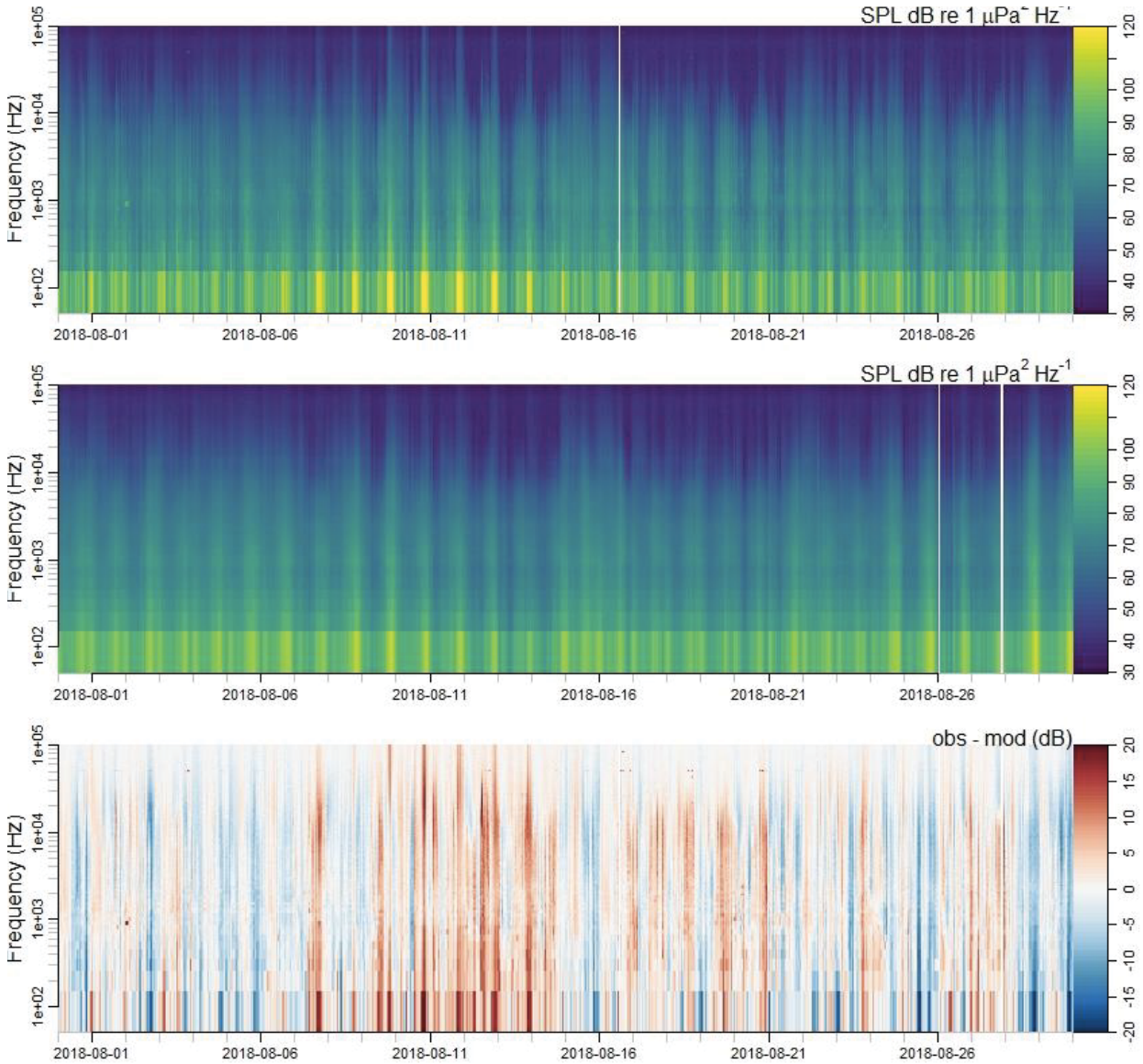

A2 Figure 3: Comparative Spectrograms. Top) Received level spectrogram from August 2018. Missing data on the 16th are due to the mooring being removed for servicing. Middle) Spectrogram predicted by Eq. 34 over the same time period. Missing data in the predicted spectrogram are attributed to incomplete wind and rain information. Bottom) Spectrogram of the difference in dB between the observed and predicted spectrograms. Red represents positive residuals (model underestimation) while blue represent negative residuals (model overestimation).

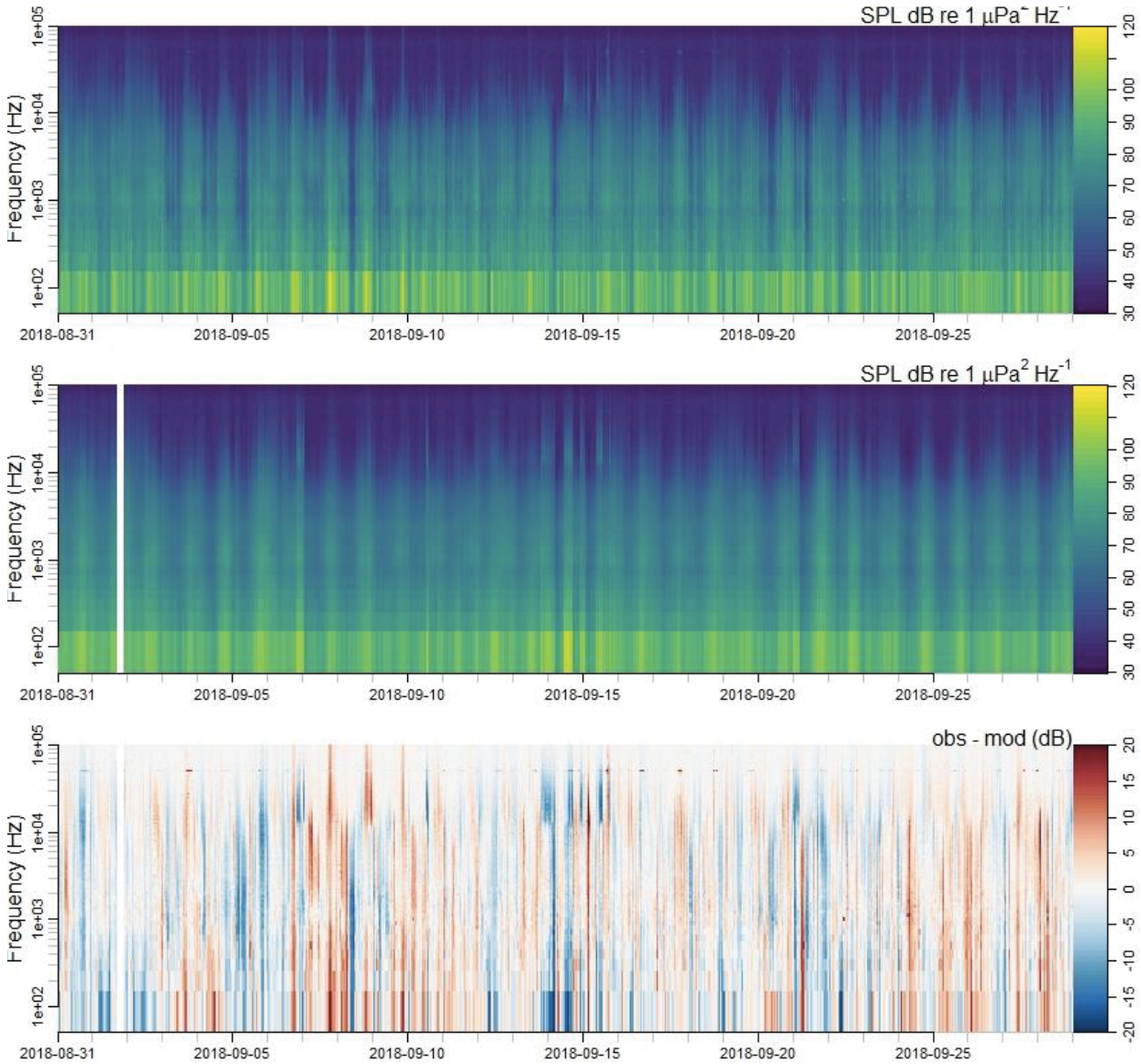

A2 Figure 4: Comparative Spectrograms. Top) Received level spectrogram from September 2018. Middle) Spectrogram predicted by Eq. 34 over the same time period. Missing data in the predicted spectrogram are attributed to incomplete wind and rain information. Bottom) Spectrogram of the difference in dB between the observed and predicted spectrograms. Red represents positive residuals (model underestimation) while blue represent negative residuals (model overestimation).

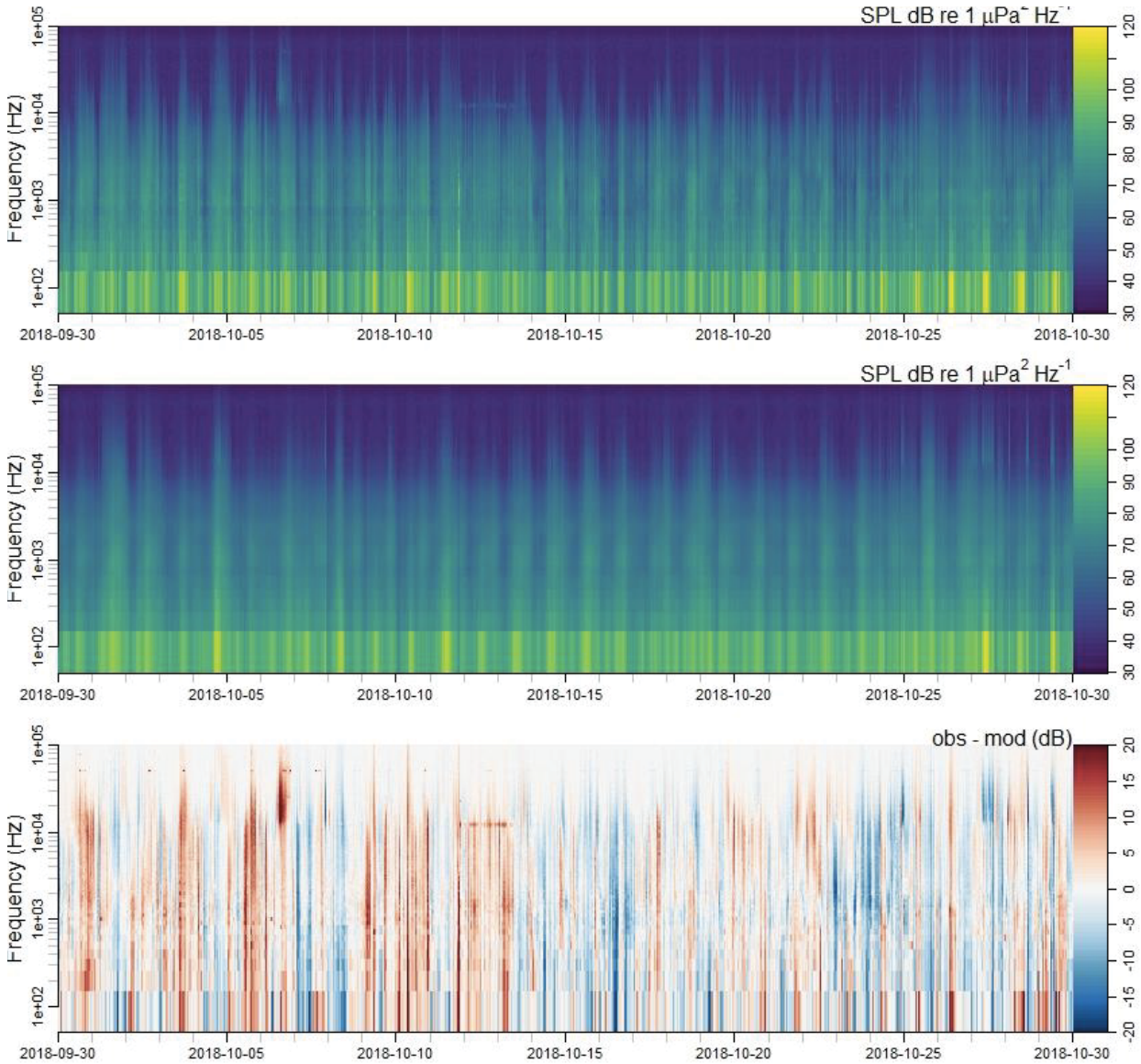

A2 Figure 5: Comparative Spectrograms. Top) Received level spectrogram from October 2018. Middle) Spectrogram predicted by Eq. 34 over the same time period. Bottom) Spectrogram of the difference in dB between the observed and predicted spectrograms. Red represents positive residuals (model underestimation) while blue represent negative residuals (model overestimation).

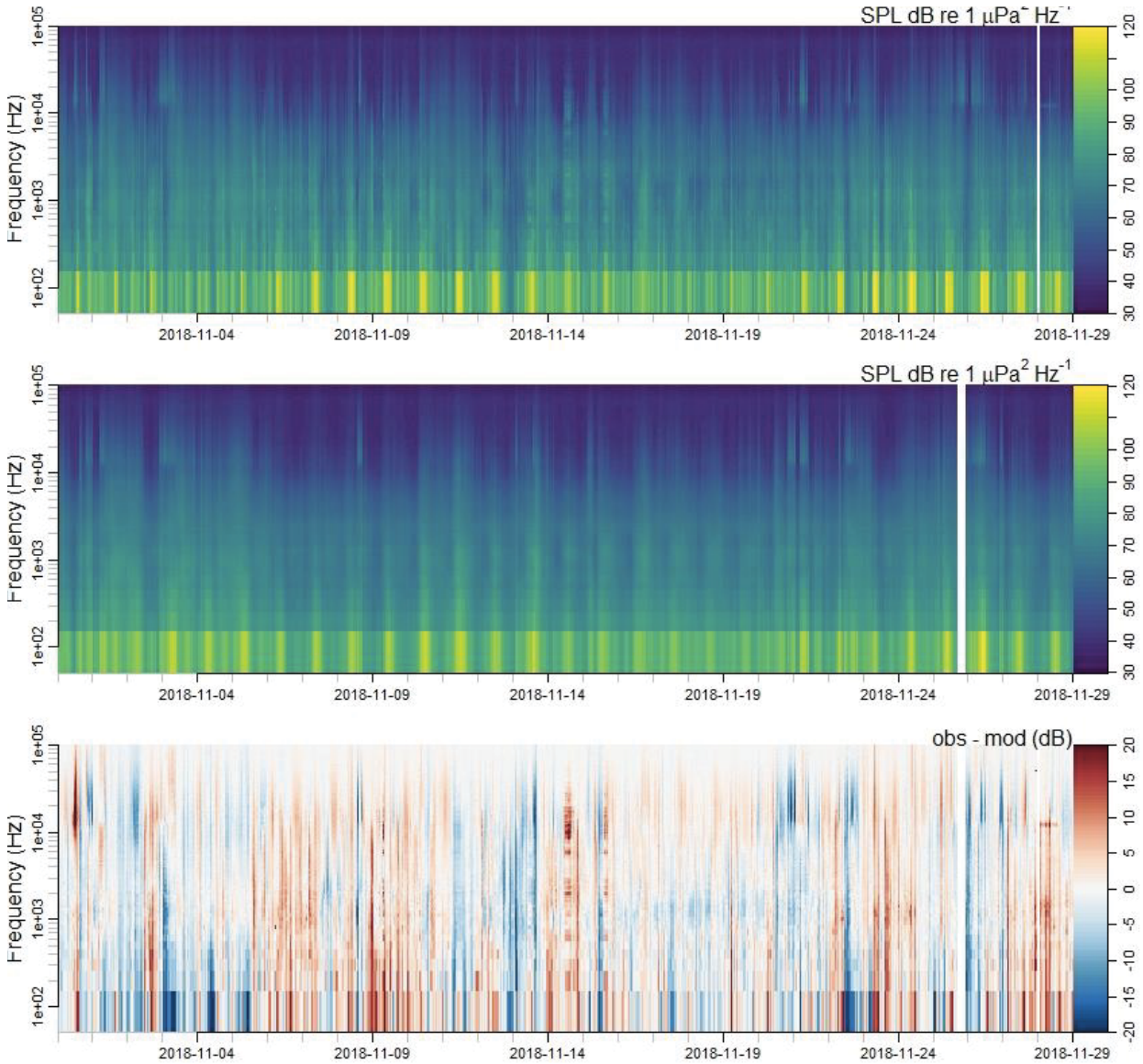

A2 Figure 6: Comparative Spectrograms. Top) Received level spectrogram from November 2018. Missing data on the 16th are due to the mooring being removed for servicing. Middle) Spectrogram predicted by Eq. 34 over the same time period. Missing data in the predicted spectrogram are attributed to incomplete wind and rain information. Bottom) Spectrogram of the difference in dB between the observed and predicted spectrograms. Red represents positive residuals (model underestimation) while blue represent negative residuals (model overestimation).

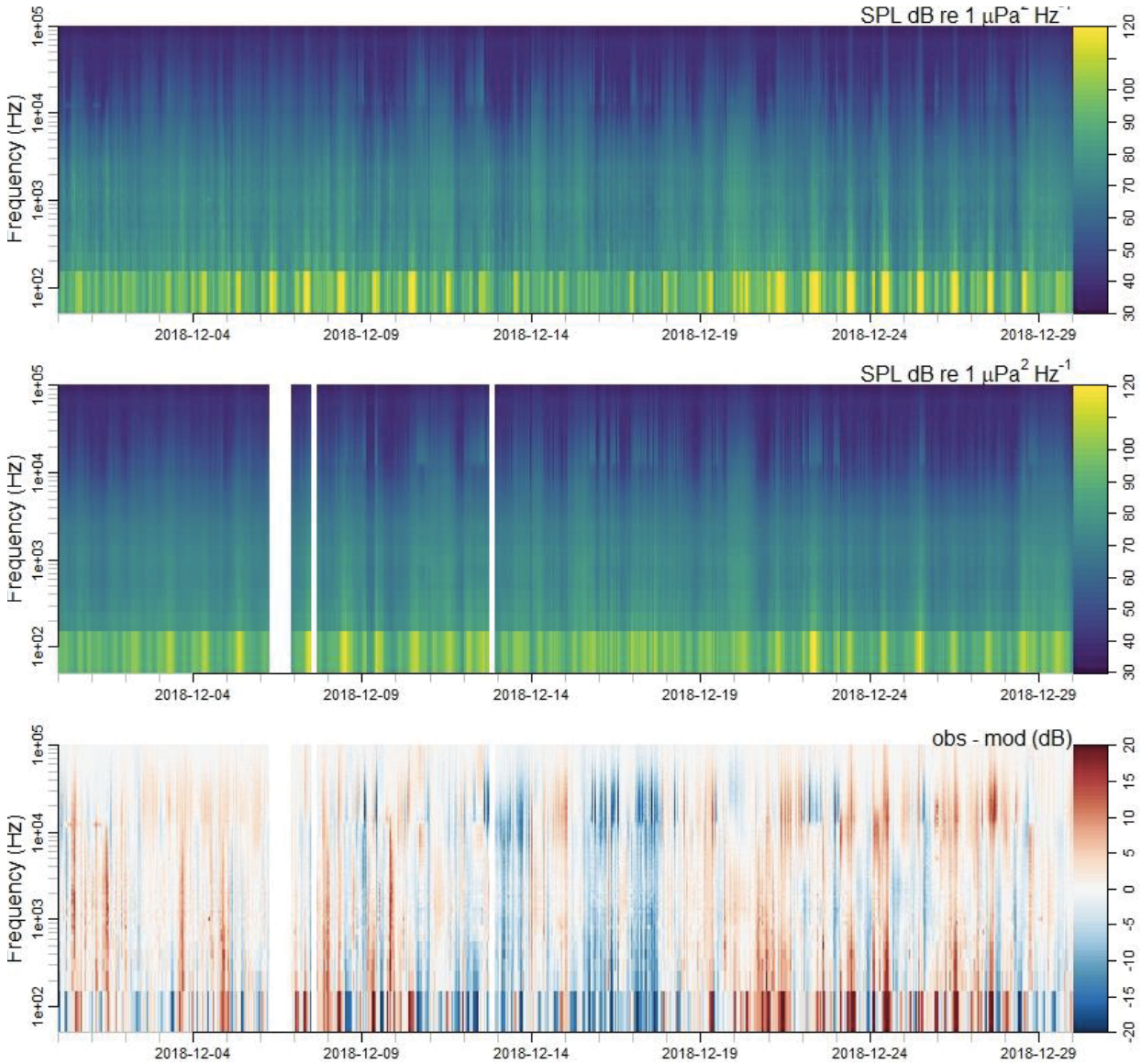

A2 Figure 7: Comparative Spectrograms. Top) Received level spectrogram from December 2018. Middle) Spectrogram predicted by Eq. 34 over the same time period Missing data in the predicted spectrogram are attributed to incomplete wind and rain information. Bottom) Spectrogram of the difference in dB between the observed and predicted spectrograms. Red represents positive residuals (model underestimation) while blue represent negative residuals (model overestimation).

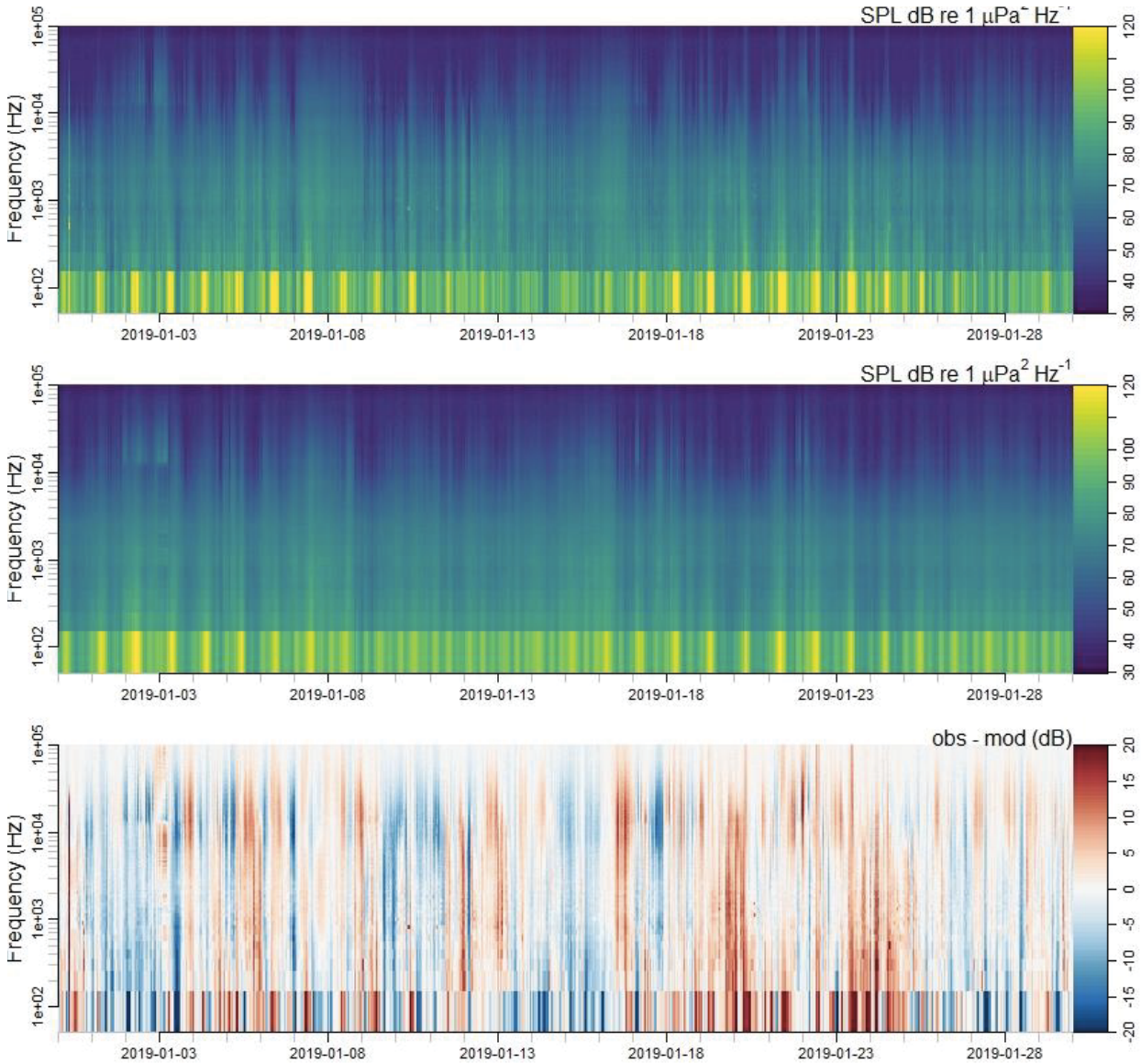

A2 Figure 8: Comparative Spectrograms. Top) Received level spectrogram from January 2019. Middle) Spectrogram predicted by Eq. 34 over the same time period. Bottom) Spectrogram of the difference in dB between the observed and predicted spectrograms. Red represents positive residuals (model underestimation) while blue represent negative residuals (model overestimation).

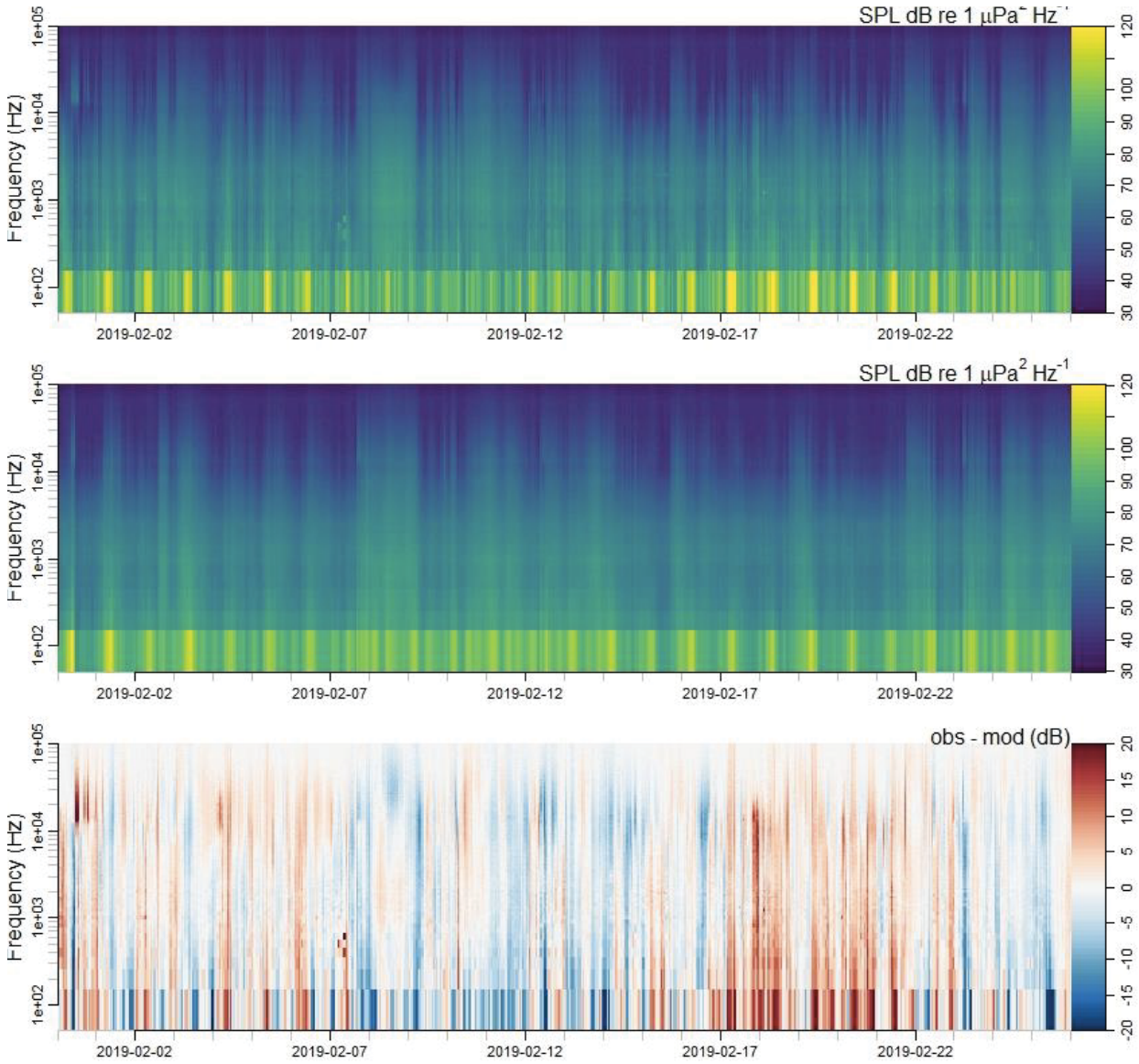

A2 Figure 9: Comparative Spectrograms. Top) Received level spectrogram from February 2019. Middle) Spectrogram predicted by Eq. 34 over the same time period. Bottom) Spectrogram of the difference in dB between the observed and predicted spectrograms. Red represents positive residuals (model underestimation) while blue represent negative residuals (model overestimation).